DEUTSCHES ELEKTRONEN-SYNCHROTRON

DESY-THESIS-1998-017
June 1998

A Measurement of the Polarised Parton Densities of the Nucleon in Deep-Inelastic Scattering at HERMES

by

M. A. Funk

ISSN 1435-8085

NOTKESTRASSE 85 - 22607 HAMBURG

To be sure that your reports and preprints are promptly included in the HEP literature database
send them to (if possible by air mail):

DESY
Zentralbibliothek
Notkestraße 85
22603 Hamburg
Germany

DESY
Bibliothek
Platanenallee 6
15738 Zeuthen
Germany

A Measurement of the Polarised Parton Densities of the Nucleon in Deep-Inelastic Scattering at HERMES

Dissertation
zur Erlangung des Doktorgrades
des Fachbereichs Physik
der Universität Hamburg

vorgelegt von
Marcus Andreas Funk
aus Heidelberg

Hamburg
1998

Gutachter der Dissertation:	Prof. Dr. A. Wagner Prof. Dr. B. Naroska
Gutachter der Disputation:	Prof. Dr. A. Wagner Prof. Dr. E. Lohrmann
Datum der Disputation:	9. 6. 1998
Dekan des Fachbereichs Physik und Vorsitzender des Promotionsausschusses:	Prof. Dr. B. Kramer

Zusammenfassung

Thema dieser Arbeit ist die Messung der Beiträge verschiedener Quark-Flavours zum Spin des Nukleons.

Im ersten Teil wird zunächst eine Einführung in die physikalischen und experimentellen Grundlagen für eine solche Analyse gegeben. Dabei wird insbesondere eine neue semi-inklusive Größe, die Purity, als Funktion der unpolarisierten Partondichteverteilungen und Fragmentationsfunktionen definiert.

Danach wird die Messung der inklusiven und semi-inklusiven Teilchen-Spinasymmetrien beschrieben und auf die in den Jahren 1995 und 1996 auf ^{3}He und Wasserstoff genommenen HERMES-Daten angewandt.

Im Anschluß wird ein Formalismus zur Extraktion der polarisierten Partondichteverteilungen aus Teilchen-Spinasymmetrien unter Verwendung der Purities vorgestellt und auf die gemessenen Asymmetrien angewandt. Die ersten und zweiten Momente der Verteilungen werden berechnet, bevor die Ergebnisse mit existierenden Messungen und anderen Vorhersagen verglichen werden.

Der Anhang enthält eine Zusammenstellung von formalen Details, welche in der Analyse Verwendung finden. Darüber hinaus werden dort einige Software-Module beschrieben, die während der Entstehung dieser Arbeit für HERMES angefertigt wurden.

Abstract

The subject of this thesis is the measurement of the different contributions of the quark flavours to the nucleon spin.

In the first part an introduction to the physical and experimental prerequisites for the analysis is given. In particular a new quantity, the purity, is defined as a function of the unpolarised parton densities and fragmentation functions.

Then the measurement of inclusive and semi-inclusive particle spin asymmetries is described and results are presented for the HERMES data taken in 1995 and 1996 on ^{3}He and hydrogen.

Subsequently a formalism to use purities for the conversion of particle asymmetries into quark polarisations is introduced and applied to the measured asymmetries. The first and second moments are calculated before the results are compared to existing measurements and other predictions.

The appendix contains a summary of formal details used in the spin decomposition. Furthermore it describes a number of software modules that were developed for HERMES in the course of this work.

Contents

Chapter 1

Introduction

The structure of matter has been for all time one of the main topics of physical research. Our present understanding of the world is summarised by the "standard model", which is in very good agreement with all experimental observations that are currently available. According to this model all matter consists of elementary fermions, the quarks and leptons, which are bound together by the exchange of bosons. However the standard model is not really satisfactory since it can not describe the masses of the elementary particles, which have to be introduced as external parameters of the theory. Furthermore the fact that there are three families of fermions with identical properties except for their masses gives rise to the presumption, that there is an underlying ordering scheme that is not yet discovered. On the other hand three of the four fundamental forces (strong and weak interaction, electromagnetism and gravitation) can be described by formally very similar field theories, the electro-weak theory and Quantum Chromodynamics (QCD). As the spectroscopy of the electromagnetic bound atoms helped to understand the electromagnetic field theory, the study of the structure of the nucleons can tell us details about the strong interaction described by QCD. In particular the question of how the spin of the nucleon is built up from its constituents is not yet resolved. While the naive quark model describes the magnetic moments of the nucleons well, it fails in predicting the spin fraction carried by quarks, which was in 1987 measured to be less than 30% surprisingly [EMC89b]. Meanwhile the inclusive structure functions of the proton and the neutron are known with much better precision and confirmed this result. HERMES is one of the experiments that was designed to use modern experimental techniques to study the spin composition of the nucleon in more detail by semi-inclusive measurements. This work will present a new analysis method that allows the extraction the polarisations of individual quarks inside the nucleon by measuring the spin-asymmetries of hadron production in deep-inelastic scattering.

Chapter 2

Inclusive Deep-Inelastic Scattering

Other than in elastic scattering, in inelastic scattering the numbers and/or types of the particles in the final state are not the same as the incoming particles. A process is called deep-inelastic if the wavelength of the exchanged boson is small compared to the dimensions of at least one incident particle, i.e. if the inner structure of this particle can be resolved. At HERMES polarised electrons or positrons (denoted in the following as lepton) $\vec{l}$ are scattered on polarised nucleons $\vec{N}$ to probe the spin structure of the nucleons:

$$\vec{l} + \vec{N} \longrightarrow l' + X. \tag{2.1}$$

While in inclusive measurements only the kinematics of the outgoing lepton l' is detected, semi-inclusive measurements include also parts of the nucleonic fragments X. For an exclusive measurement all particles and their momenta in the final state are known.

In this chapter the formalism of inclusive deep-inelastic reactions (2.1) will be introduced along with the interpretation in the standard physical model (QPM). In the first part the unpolarised case will be discussed before the polarised inclusive process is treated at the end of the chapter.

2.1 Kinematics of Deep-Inelastic Scattering

In Figure 2.1 a deep inelastic scattering process is shown in the rest frame of the nucleon to introduce the basic kinematical variables. Neglecting the thermal motion of the target atoms and the Fermi motion of the nucleons

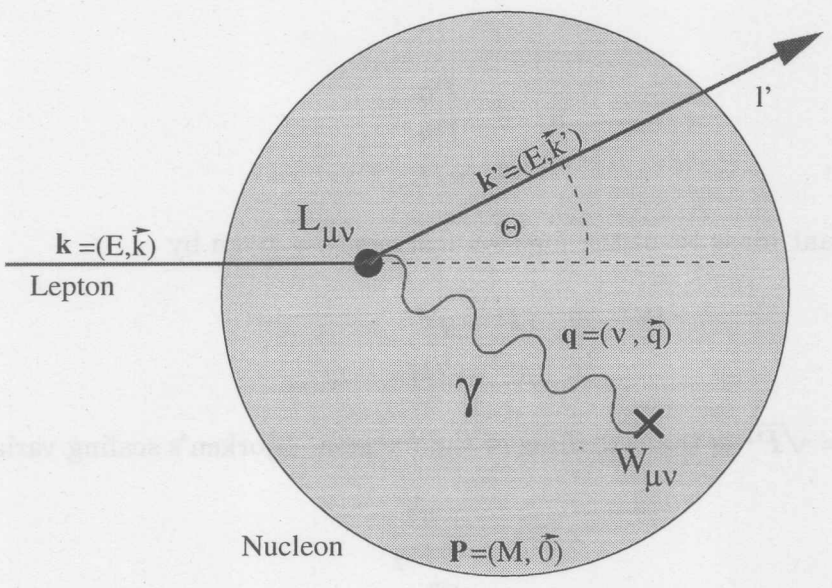

Figure 2.1: Schematic Picture of an Inclusive DIS Process. *A lepton of high energy penetrates a nucleon and emits a virtual photon γ that couples to the nucleonic field. The wavelength of the photon is small compared to the dimensions of the nucleon. The cross section for this reaction is proportional to the product of the lepton tensor $L_{\mu\nu}$ and the hadronic tensor $W_{\mu\nu}$. In inclusive measurements only the energy and angle θ of the deflected lepton is registered.*

within the atoms, this coordinate system coincides with the laboratory frame. The four-vector of the scattered lepton before and after the scattering process will be denoted by $\boldsymbol{k}$ and $\boldsymbol{k'}$, the scattering angle by θ, the four-momentum of the virtual photon by $\boldsymbol{q}$ and the four-momentum of the nucleon before the reaction by $\boldsymbol{P}$ (see also Table 2.1).

We now will define a set of useful Lorentz-invariant quantities together with their expressions in the lab frame. First the negative squared four-momentum transfer can be measured as

$$\begin{aligned} Q^2 &= -\boldsymbol{q}^2 = -(\boldsymbol{k}-\boldsymbol{k'})^2 \\ &\overset{\text{lab}}{=} 4EE'\sin^2\theta/2, \end{aligned} \tag{2.2}$$

while the absolute and fractional energy transfer of the lepton in the lab system ν and y can be expressed as

$$\begin{aligned} \nu &= \frac{\boldsymbol{Pq}}{\sqrt{\boldsymbol{P}^2}} \\ &\overset{\text{lab}}{=} E - E', \end{aligned} \tag{2.3}$$

and

$$\begin{aligned} y &= \frac{\boldsymbol{P}\boldsymbol{q}}{\boldsymbol{P}\boldsymbol{k}} \\ &\overset{\text{lab}}{=} \nu/E. \end{aligned} \tag{2.4}$$

The invariant mass W of the nucleon fragments is given by

$$\begin{aligned} W^2 &= (\boldsymbol{P}+\boldsymbol{q})^2 \\ &\overset{\text{lab}}{=} M^2 + 2M\nu - Q^2, \end{aligned} \tag{2.5}$$

where $M = \sqrt{\boldsymbol{P}^2}$ is the rest mass of the nucleon. Bjorken's scaling variable

$$\begin{aligned} x &= -\frac{\boldsymbol{q}^2}{2\boldsymbol{P}\boldsymbol{q}} \\ &\overset{\text{lab}}{=} \frac{Q^2}{2M\nu}, \end{aligned} \tag{2.6}$$

is a measure for the inelasticity of the scattering process: for $x = 1$ the squared invariant mass of the nucleon fragments W^2 equals the squared nucleon mass M^2 (elastic case) while low x identify a highly inelastic reaction.

2.2 Unpolarised Cross Section and Structure Functions

In lowest order Quantum Electrodynamics (QED) the double differential cross section for (2.1) can be expressed as the contraction of the leptonic tensor $L_{\mu\nu}$ with the hadronic tensor $W_{\mu\nu}$,

$$\frac{d^2\sigma}{dQ^2 d\nu} = \frac{4\pi\alpha^2}{Q^4 E^2} L_{\mu\nu} W^{\mu\nu}, \tag{2.7}$$

where $\alpha \approx \frac{1}{137}$ is the electromagnetic coupling constant. At HERMES energies ($\sqrt{s} \ll m_Z, m_{W^\pm}$) the contribution of weak currents can be neglected. The leptonic tensor $L_{\mu\nu}$ describes the coupling of the intermediate photon to the point-like lepton and is well known from QED. In contrast to that, the hadronic tensor $W_{\mu\nu}$ describing the coupling of the photon to the spatially extended nucleon is not yet calculable from first principles. Instead requiring Lorentz invariance, parity conservation (for non-weak processes), and invariance under time reversal yields an expression of $W_{\mu\nu}$ in terms of scalar structure functions. The cross section (2.7) can then be expressed for the unpolarised case (i.e. averaged over the spin states of the incoming lepton and summed over the

Inclusive Observables	
Variable	Name
$\boldsymbol{k}$ $\begin{cases} E \\ \vec{k} \end{cases}$	Beam energy Momentum and direction of incident lepton
$\boldsymbol{k'}$ $\begin{cases} E' \\ \vec{k'} \end{cases}$	Energy of scattered lepton Momentum and direction of scattered lepton
$\boldsymbol{P}$ $\begin{cases} M \\ \vec{P}(=0) \end{cases}$	Nucleon mass Momentum of nucleon

Derived Variables		
Variable	Definition	Name
θ	$\angle(\vec{k'}, \vec{k})$	Scattering angle of lepton
$\boldsymbol{q}$	$\boldsymbol{k'} - \boldsymbol{k}$	Four momentum transfer
Q^2	$4EE' \sin^2 \theta/2$	Negative squared four momentum transfer
s	$M^2 + 2EM + m_e^2$	Squared centre of mass energy
ν	$(E - E')_{lab}$	Energy transfer in lab frame
y	ν/E	Relative energy transfer
x	$Q^2/(2M\nu)$	Bjorken's scaling variable
W^2	$M^2 + Q^2/x - Q^2$	Invariant mass of hadronic final state

Table 2.1: Definition of the Inclusive Kinematical Variables as used in this text. *See also Figure 2.1.*

spin states of the outgoing lepton) as

$$\frac{d^2\sigma}{dxdQ^2}(x,Q^2) = \frac{4\pi\alpha^2}{xQ^4}\left(xy^2\mathbf{F_1}(x,Q^2) + \left(1 - y - \frac{xyM}{s}\right)\mathbf{F_2}(x,Q^2)\right), \quad (2.8)$$

where $F_{1/2}(x,Q^2)$ are the dimensionless structure functions of the nucleon.

2.3 The Quark Parton Model

The measurement of the structure functions of the proton revealed that they depend only very weakly on Q^2. Furthermore the Callan-Gross relation [CG69]

$$F_2(x) = 2xF_1(x), \quad (2.9)$$

which is true for the scattering of two point-like spin-1/2 particles by the exchange of a vector boson, was measured to be fulfilled to a high degree. In the framework of the group-theoretical $SU(3)$ flavour model of Gell-Mann [Gel64] and Zweig [Zw64] this leads to the following interpretation of the deep-inelastic scattering in terms of the Quark Parton Model (QPM).

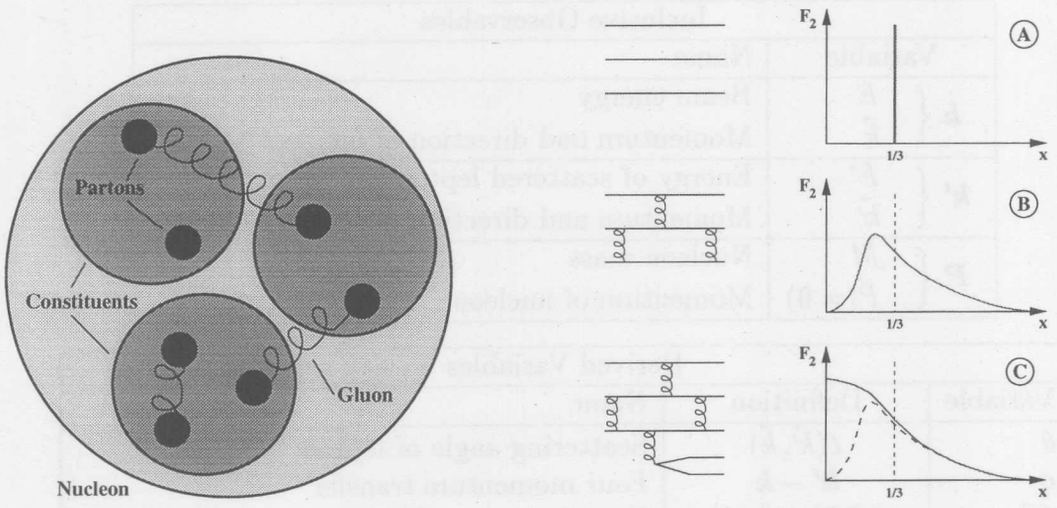

Figure 2.2: The Quark Parton Model. *On the left a schematic sketch of the picture of the nucleon in the QPM is shown. The valence quarks are surrounded by a cloud of virtual gluons and quark anti-quark pairs (called sea). A valence quark together with its QCD cloud is called constituent, while the parts of a constituent (quarks and gluons) are called partons. On the right the different contributions to the parton momentum distribution $F_2(x)$ are shown. If the nucleon only contained the 3 valence quarks each of them would carry one third of the nucleon momentum (a). The exchange of gluons lowers and smears the momentum distributions of the valence quarks and hides parts of the nucleonic momentum from electroweak interactions (b). The gluons might split up into quark anti-quark pairs which give an additional sea contribution at small x.*

The SU(3) model explains the quantum numbers of the hadrons by interpreting them as a composition of spin-1/2 particles, called quarks. According to the model, the quarks are solely responsible for the strong interaction of hadrons and hence they don't only carry electro-weak charges but get assigned an additional strong charge called colour. The model assumes that all isolated particles that can be observed in nature have to be colour-neutral (confinement) and explains the mesons as quark anti-quark states while the baryons are made up of three quarks. These quarks that fix the quantum numbers of a hadron are called valence quarks. The field bosons of the field theory of strong interaction (Quantum Chromodynamics, QCD) are called gluons. As a naked electron in QED is surrounded by a cloud of virtual photons, electrons and positrons, a quark might emit a virtual gluon which splits up into a quark anti-quark pair. Quarks produced in this process are called sea quarks (see left side of Figure 2.2). A valence quark together with its cloud of gluons and sea quarks is called a constituent quark of the hadron. Unlike in QED the field bosons of the strong force are not neutral, which leads to the fact, that there

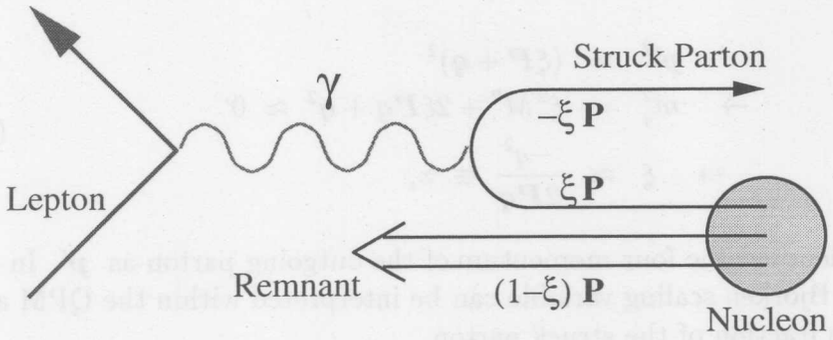

Figure 2.3: DIS Process in Breit-Frame.

are direct gluon-gluon interactions in QCD. Field theories with this property are called non-Abelian. As a consequence the strong coupling constant α_s is much more scale dependent than the electromagnetic coupling constant, it grows very rapidly for low Q^2. First order QCD yields [PRS94]:

$$\alpha_s(Q^2) = \frac{12\pi}{(33 - 2n_f)\ \ln(Q^2/\Lambda_0^2)}, \tag{2.10}$$

where n_f is the number of quark flavours contributing at the given energy ($n_f = 3$ for HERMES energies) and $\Lambda_0 \approx 0.25$ GeV/c is the QCD scale parameter. This running coupling constant (or the non-Abelian character of the theory) is the explanation in QCD for the confinement effect and makes perturbative calculations for low energies very hard or even impossible. Equation (2.10) explains also a second feature of QCD called asymptotic freedom, which describes the fact that quarks and gluons behave as free particles at small distances (i.e. high Q^2).

At high Q^2 (i.e. small wavelength of the coupling photon) the QPM assumes the partons in the nucleon to be only loosely coupled (or "quasi-free"). For further discussion the scattering process is considered in the Bjorken Limit ($Q^2 \to \infty, \nu \to \infty$ for fixed x) and in the Breit-frame, where the energy transfer of the photon is zero, i.e. the struck parton is backscattered, while the other constituents are not affected and all transversal momentum components are neglected. In the Breit-frame the longitudinal momentum fraction ξ of the struck parton (Nachtmann variable) can be defined as shown in Figure 2.3. Under the additional assumption that the parton mass m_q vanishes it can be seen from momentum conservation at the photon parton vertex that $\xi \approx x$:

$$\begin{aligned} \boldsymbol{p'}^2 &= (\xi \boldsymbol{P} + \boldsymbol{q})^2 \\ \rightarrow \quad m_q^2 &= \xi^2 M^2 + 2\xi \boldsymbol{P}\boldsymbol{q} + \boldsymbol{q}^2 \approx 0 \\ \rightarrow \quad \xi &\approx \frac{-q^2}{2\boldsymbol{P}\boldsymbol{q}} \equiv x, \end{aligned} \tag{2.11}$$

where we denoted the four momentum of the outgoing parton as $\boldsymbol{p'}$. In other words, the Bjorken scaling variable can be interpreted within the QPM as the momentum fraction of the struck parton.

Furthermore, we are now able to resolve the hadronic tensor $W_{\mu\nu}$ in terms of the fundamental electroweak coupling of the exchanged boson to one parton of the nucleon. That is, the scattering process can be expressed as the incoherent sum of the interaction of the lepton with the partons. The structure function $F_2(x)$ is then interpreted as the charge-weighted sum of the parton momentum distributions $xq(x)$:

$$F_2(x) = \sum_q e_q^2 x q(x), \tag{2.12}$$

where q runs over all quark flavours (including anti-quarks) of interest at the given energy scale. The functions $q(x)$ can be interpreted as the number density of a quark with flavour q and momentum fraction x in the nucleon and are called Parton Density Functions (PDFs)[1]. The PDFs are usually split into valence and sea contributions

$$q(x) = q_v(x) + q_s(x), \tag{2.13}$$

where for nucleons only $u_v(x)$ and $d_v(x)$ are different from zero. Because of the symmetric production mechanism of the sea, the relation

$$\bar{q}_s(x) = q_s(x) \tag{2.14}$$

holds for all flavours. It should be noted that integration of (2.12) yields only half of the proton momentum [PRS94]. The rest of the momentum is carried by the gluons, which are electro-weakly neutral (see right side of Figure 2.2).

The naive Quark Parton Model describes the results of the early experiments very well. However there are measurable deviations from the Callan-Gross relation (2.9) which can be parametrised by the function $R(x, Q^2)$:

$$R(x, Q^2) = (1 + \gamma^2)\frac{F_2(x, Q^2)}{2xF_1(x, Q^2)} - 1, \tag{2.15}$$

[1] Often $q(x)$ is refered to as the probability to find a quark of flavour q with momentum fraction x. This is misleading since the integral $\int u(x)dx$ is not one since the proton contains two valence u quarks.

where γ^2 is a kinematical factor defined by

$$\gamma^2 = \frac{Q^2}{\nu^2} = \frac{4M^2x^2}{Q^2}. \tag{2.16}$$

For later approximations one should remember that $\gamma^2 \ll 1$, since $4M^2x^2$ is small compared to Q^2; in the Bjorken limit γ^2 vanishes. $R(x,Q^2)$ can be interpreted as the ratio of the absorption cross section of longitudinally (σ_L) and transversely (σ_T) polarised virtual photons by the nucleon:

$$\begin{aligned} R(x,Q^2) &= \sigma_L/\sigma_T, \\ \sigma &= \Gamma_T(\sigma_T + \varepsilon\sigma_L), \end{aligned} \tag{2.17}$$

where σ is the total cross section, Γ_T is the total flux of transversely polarised virtual photons and ε is the ratio of probabilities that the lepton emits a longitudinally or transversely polarised photon (which is calculable in QED):

$$\varepsilon = \frac{\Gamma_L}{\Gamma_T} = \frac{1-y}{1-y+\frac{1}{2}y^2}. \tag{2.18}$$

The Callan-Gross relation is equivalent to $\sigma_L = 0$ which means that in the naive QPM, neglecting parton masses and transversal momenta, a nucleon can not contain partons with transversely oriented spin. $R(x,Q^2)$ corrects for the deviations from these approximations.

In addition to the breaking of the Callan-Gross relation, structure function data taken with high precision show a scaling violation, i.e. the structure functions explicitly depend on Q^2 (see Figure 2.4). QCD allows the calculation of these effects by the Gribov-Lipatov-Altarelli-Parisi (GLAP) equations [GL72, Lip75, AP77] which can be used to evolve structure functions measured at a certain Q^2 to a fixed Q_0^2. The breaking of the Q^2-scaling is again a consequence of the invisibility of the gluons: a quark with momentum fraction x_1 might emit a gluon and remain with the momentum fraction $x_2 < x_1$. The resolution of the photon increases with Q^2, and while at Q_0^2 the gluon-emission can not always be resolved, the process becomes visible at higher $Q^2 > Q_0^2$. At higher Q^2 one expects to measure a smaller x_2 since the gluons are not visible. This translates into an increase of $F_2(x,Q^2)$ with increasing Q^2 for small x and a decrease over Q^2 for high x as seen in the data.

2.4 Polarised Deep-Inelastic Scattering

The unpolarised cross section (2.8) was calculated by averaging over both spin states of the incoming lepton, which means that all spin-asymmetric contributions to $L_{\mu\nu}W^{\mu\nu}$ cancel themselves. On the other hand by calculating the

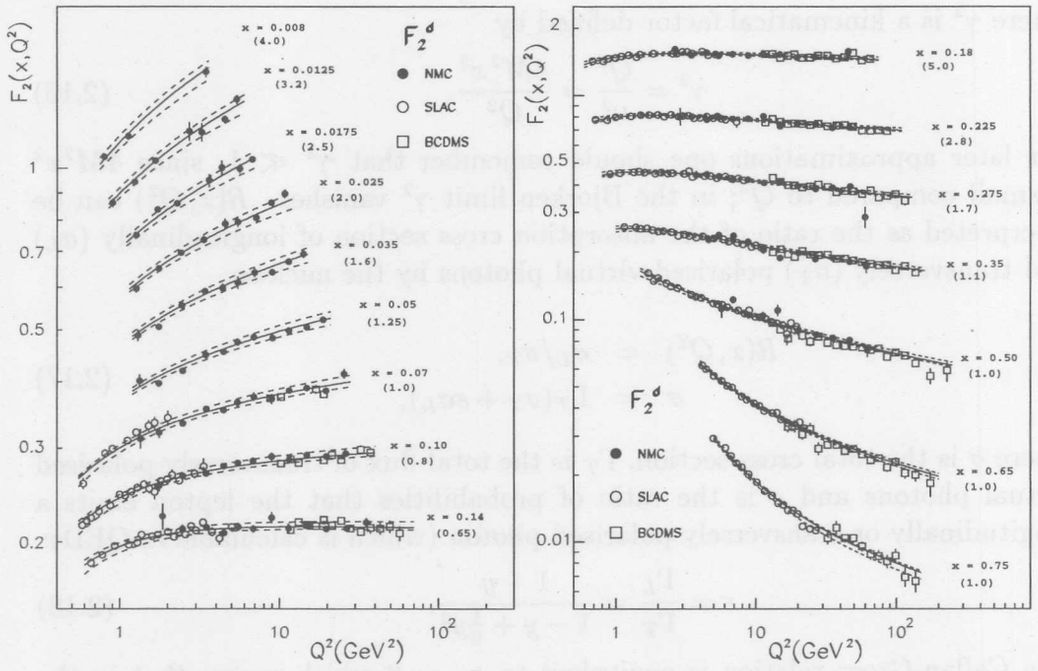

Figure 2.4: The Structure Function $F_2^p(x, Q^2)$. *In this picture F_2^p as published in [NMC95, SLAC92, BCDMS90] is plotted as a function of Q^2 for different values of x. The scaling property shows up at medium x while it is clearly violated for small and large x. The numbers in parenthesis are offset factors for a clear layout.*

difference of both spin states, the symmetric parts are suppressed and the asymmetric terms become apparent.

In Figure 2.5 the angles of a polarised scattering process are defined. In addition to the scattering angle θ the angle between the direction of the target polarisation $\vec{S}$ and the incident electron beam $\vec{k}$ is named α while φ denotes the angle between the scattering plane (defined by the directions of the incident and scattered lepton) and the target polarisation plane (defined by the direction of the incident lepton and the direction of the target polarisation $\vec{S}$). The cross section difference for right- and left-handed incident leptons can then be calculated as

$$\frac{d^3\sigma(\alpha) - d^3\sigma(\alpha + 180°)}{dx dy d\varphi} = \frac{e^4}{4\pi^2 Q^2}\left\{\left[\left(1 - \frac{y}{2} - \frac{y^2}{4}\gamma^2\right)\mathbf{g_1}(x,Q^2) - \frac{y}{2}\gamma^2\mathbf{g_2}(x,Q^2)\right]\cos\alpha - \sqrt{\gamma^2\left(1 - y - \frac{y^2}{4}\gamma^2\right)}\left[\frac{y}{2}\mathbf{g_1}(x,Q^2) + \mathbf{g_2}(x,Q^2)\right]\sin\alpha\cos\varphi\right\}, \tag{2.19}$$

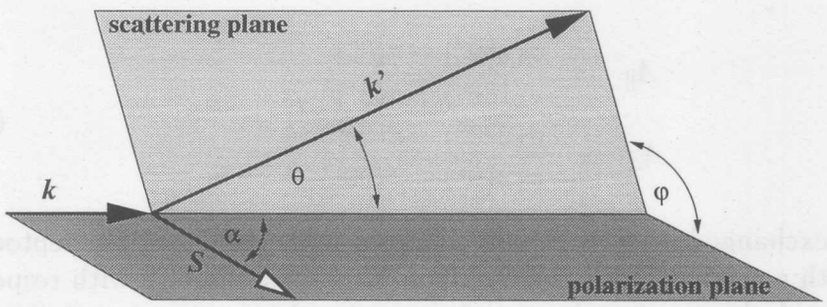

Figure 2.5: Definition of scattering angles in polarised DIS. *See equation (2.19).*

where $g_{1/2}(x, Q^2)$ are in analogy to $F_{1/2}(x, Q^2)$ the dimensionless polarised structure functions of the nucleon. γ^2 is defined in (2.16).

To describe the polarised structure functions in the Quark Parton Model, the quark distributions $q(x)$ and quark spin distributions $\Delta q(x)$ are written as

$$\begin{aligned} q(x) &= q^+(x) + q^-(x), \\ \Delta q(x) &= q^+(x) - q^-(x), \end{aligned} \tag{2.20}$$

where $q^{+(-)}(x)$ is the density of quarks with flavour q and momentum fraction x with the helicity parallel (anti-parallel) to the nucleon spin. The structure functions $g_{1/2}(x)$ scale like $F_{1/2}(x)$ for high Q^2 and ν and can in analogy to (2.12) be expressed as

$$\begin{aligned} g_1(x) &= \frac{1}{2} \sum_q e_q^2 \Delta q(x), \\ g_2(x) &= 0. \end{aligned} \tag{2.21}$$

Similar to the unpolarised case, the naive QPM reduces the number of structure functions from two to one, which is again the consequence of scaling approximations.

2.5 Experimental Determination of g_1

The spin structure functions can be determined experimentally by measuring the cross sections in two longitudinal ($\alpha = 0°, 180°$) and two transversal ($\alpha = 90°, 270°$) spin configurations:

$$\begin{aligned} A_{\parallel} &= \frac{\sigma(180°) - \sigma(0°)}{\sigma(180°) + \sigma(0°)}, \\ A_{\perp} &= \frac{\sigma(270°) - \sigma(90°)}{\sigma(270°) + \sigma(90°)}. \end{aligned} \tag{2.22}$$

Since the exchanged photon is not collinear with the incoming lepton but emitted with a certain angle, the measured asymmetries $A_{\parallel/\perp}$ with respect to the lepton polarisation first have to be translated into the virtual Compton scattering asymmetries $A_{1/2}$ [Dür95] by

$$\begin{aligned} A_{\parallel} &= D(A_1 + \eta A_2), \\ A_{\perp} &= d(A_2 - \xi A_1), \end{aligned} \tag{2.23}$$

with the kinematical factors

$$\begin{aligned} D &= \frac{y(2-y)}{y^2 + 2(1-y)(1+R(x,Q^2))}, & \eta &= \frac{2\gamma(1-y)}{2-y}, \\ d &= D\sqrt{\frac{2\varepsilon}{1+\varepsilon}}, & \xi &= \eta\frac{1+\varepsilon}{2\varepsilon}, \end{aligned} \tag{2.24}$$

before the polarised structure functions can be extracted by inverting

$$\begin{aligned} A_1 &= \frac{g_1 - \gamma^2 g_2}{F_1}, \\ A_2 &= \gamma\frac{g_1 + g_2}{F_1}. \end{aligned} \tag{2.25}$$

The approximate determination of $g_1(x, Q^2)$ by only measuring $A_{\parallel}$ is possible, as the following derivation shows: First the asymmetry A_2 is limited by the positivity limit [SMC94b]

$$|A_2| \leq R(x, Q^2) \tag{2.26}$$

and measured to be consistent with zero [E143:96]. Also its contribution to $A_{\parallel}$ is suppressed by the small factor η with respect to A_1. Hence we can assume

$$A_{\parallel} \approx D A_1. \tag{2.27}$$

Solving (2.25) under the assumption of $A_2 = 0$ then yields

$$\frac{g_1}{F_1} \approx \frac{A_{\parallel}}{D} \cdot \frac{1}{1+\gamma^2}. \tag{2.28}$$

Using equation (2.15) we therefore can derive g_1 from the longitudinal spin asymmetry $A_{||}(x, Q^2)$, the unpolarised structure function $F_2(x, Q^2)$ and $R(x, Q^2)$ via

$$g_1(x, Q^2) \approx \frac{A_{||}(x, Q^2)}{D} \frac{F_2(x, Q^2)}{2x[1 + R(x, Q^2)]}. \tag{2.29}$$

Figure 2.6 shows the results for the latest measurements of the polarised structure functions of the proton g_1^p and neutron g_1^n.

2.6 Sum Rules

Up to now most of the theoretical models fail to make precise predictions for the x-dependence of the structure functions. The main reason for this is the breakdown of perturbative calculations at low energy scales due to to the increasing α_s according to equation (2.10). However, the same models often can give information about the value of certain moments of a structure function $f(x)$

$$M_n(f) = \int_0^1 x^{n-1} f(x)\, dx, \tag{2.30}$$

which then can be compared to the corresponding experimental results. Unfortunately, the distributions measured experimentally can not cover the full integration range of (2.30) and hence have to be extrapolated into some unmeasured region. The models used for this extrapolation introduce an additional uncertainty on the moments quoted by the experimentalists. In the following a brief overview for the most important sum rules is given.

2.6.1 Gottfried Sum Rule

The Gottfried sum rule [Got67] makes a prediction for the difference of the 0^{th} moments of the unpolarised structure functions $F_2^{p/n}$ of proton and neutron. Assuming iso-spin symmetry and considering the quark contents of the proton

$$\int_0^1 u_v(x)\, dx = 2; \qquad \int_0^1 d_v(x)\, dx = 1, \tag{2.31}$$

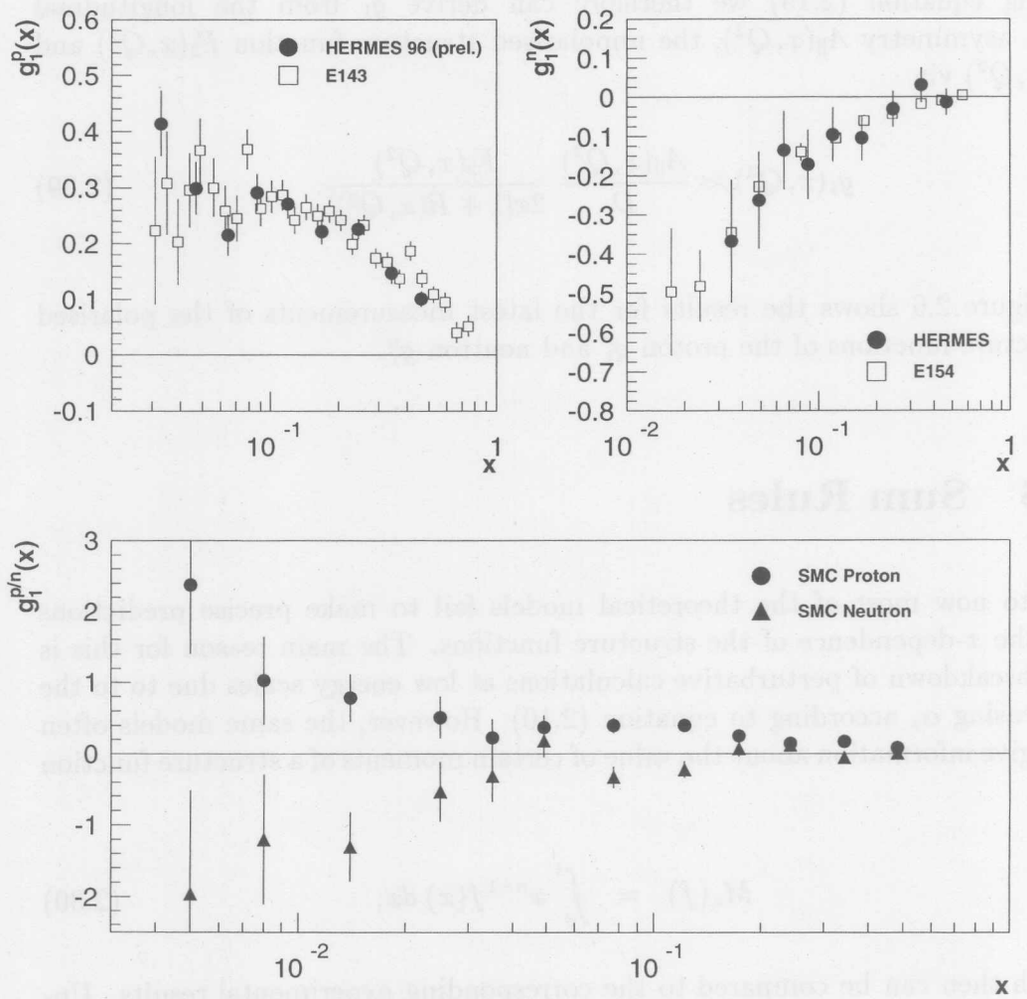

Figure 2.6: The Structure Functions g_1^p and g_1^n. *The two upper plots show the structure functions in the kinematical region that is accessible to* HERMES. *The* SLAC *proton data [E143:95] was evolved to* $Q^2 = 3$ $(\mathrm{GeV/c})^2$. *The neutron data [E154:97] is plotted for* $Q^2 = 5$ $(\mathrm{GeV/c})^2$. *The* HERMES *data [HER97b] is plotted for the measured* Q^2. *The lower plot shows* g_1^p *and* g_1^n *evolved to* $Q^2 = 10$ $(\mathrm{GeV/c})^2$ *for a larger measured* x *range using a muon beam [SMC97a, SMC97b].*

it can easily be derived from (2.12) and reads as

$$\begin{aligned} S_G &= \int_0^1 \frac{1}{x}\left(F_2^p(x) - F_2^n(x)\right) dx \\ &= \frac{1}{3} + \frac{2}{3}\int_0^1 u_s(x) - d_s(x)\, dx. \end{aligned} \tag{2.32}$$

The integral in the second line is a measure for the sea flavour asymmetry and hence the observed deviation of $S_G = 0.235 \pm 0.026$ [NMC94] from 1/3 indicates that indeed the sea flavour symmetry is broken [Ack96].

2.6.2 Bjorken Sum Rule

Under the assumption of iso-spin symmetry the first moments of the inclusive structure function g_1 on the proton and the neutron can be written for three quark flavours as

$$\Gamma_1^{p,n} = M_1(g_1^{p,n}) = \frac{1}{9}a_0 \pm \frac{1}{12}a_3 + \frac{1}{36}a_8, \tag{2.33}$$

where a_0, a_3 and a_8 are the $SU(3)$ flavour singlet, octet isotriplet and octet isosinglet combinations of the first moments of the quark distributions [ESW96]:

$$\begin{aligned} a_0 &= (\Delta u + \Delta\bar{u}) + (\Delta d + \Delta\bar{d}) + (\Delta s + \Delta\bar{s}), \\ a_3 &= (\Delta u + \Delta\bar{u}) - (\Delta d + \Delta\bar{d}), \\ a_8 &= (\Delta u + \Delta\bar{u}) + (\Delta d + \Delta\bar{d}) - 2(\Delta s + \Delta\bar{s}). \end{aligned} \tag{2.34}$$

In the following the variables Δq will denote the first moments of the polarised quark distributions $\Delta q(x)$. The two combinations a_3 and a_8 can be expressed in terms of the weak coupling constants F and D measured in baryon (n, Λ, Σ and Ξ) decays [CR93]:

$$\begin{aligned} a_3 &= F + D = 1.257 \pm 0.003, \\ a_8 &= 3F - D = 0.58 \pm 0.02. \end{aligned} \tag{2.35}$$

For the difference of $\Gamma_1^p - \Gamma_1^n$ one immediately obtains the Bjorken sum rule

$$\int_0^1 g_1^p(x) - g_1^n(x)\, dx = \frac{1}{6}(F + D) \cdot C_1^{NS}, \tag{2.36}$$

where

$$C_1^{NS} = 1 - \frac{\alpha_s(Q^2)}{\pi}, \tag{2.37}$$

is a QCD correction factor (here given to the first order) which takes into account that the polarised structure functions are measured at finite Q^2. The strong coupling constant α_s has to be calculated for the same Q^2 using equation (2.10).

Once more it should be emphasised that the Bjorken sum rule only assumes

iso-spin invariance and is therefore a very fundamental test of the QCD. Up to now all experimental data are consistent with this sum rule.

2.6.3 Ellis-Jaffe Sum Rule

Extending the Bjorken sum rule, the Ellis-Jaffe sum rule [EJ74] makes independent predictions for the first moments of the polarised structure functions $g_1^{p,n}$ of the proton and neutron. It additionally assumes exact SU(3) symmetry and an unpolarised sea ($\Delta\bar{q} = 0$). Without QCD corrections the predictions are [ESW96]

$$\begin{aligned} \Gamma_1^p &= \frac{1}{18}(9F - D) = 0.185 \pm 0.003, \\ \Gamma_1^n &= \frac{1}{18}(6F - 4D) = -0.024 \pm 0.003, \end{aligned} \tag{2.38}$$

which are not in agreement with the experimental value [SMC94a] of

$$\Gamma_1^p = 0.142 \pm 0.008 \pm 0.011. \tag{2.39}$$

The violation of this sum rule remains even after the application of QCD corrections and shows that the spin of the nucleon can not be understood as the simple sum of the three valence quark spins, a fact that was called "spin crisis". A number of experiments, one of them HERMES, have been designed to study the spin composition of the nucleon in more detail.

2.7 Summary

In this chapter the basic formalism of deep-inelastic scattering was briefly reviewed. The inclusive polarised structure functions (which are known with good precision) have been discussed and the related sum rules were presented. Although HERMES is able to measure all these inclusive quantities, one of its most important new features is the ability to observe semi-inclusive asymmetries. In the following chapter the quark parton model will be extended to the semi-inclusive case to lay the formal foundations for the main subject of this work: the extraction of polarised parton density functions from semi-inclusive asymmetries.

Chapter 3

Semi-Inclusive Deep-Inelastic Scattering and Purities

After discussing the unpolarised and polarised cases of deep-inelastic scattering in the previous chapter, we'll now turn towards the case of semi-inclusive DIS reactions

$$\vec{l} + \vec{N} \longrightarrow l' + h + X, \tag{3.1}$$

where in addition to the scattered lepton l' other particles are detected in the final state. For a formal description of the unpolarised processes, the quark parton model will be extended by a fragmentation model which allows to relate the occurrence of certain hadrons h in the final state to the parton density functions for different flavours by so called fragmentation functions. For the polarised case a new quantity, the hadron quark purities, will be introduced to extract polarised parton density functions from measured hadron asymmetries.

3.1 Semi-Inclusive DIS and the QPM

Up to now we discussed deep inelastic processes only by inclusive measurements of the form (2.1), i.e., the kinematics of the scattered lepton alone have been of interest. Although it is possible to determine the structure functions with such measurements, it is not possible to break them up into the parton density functions as they are predicted by the quark parton model. We will now see how additional information about other particles generated by the scattering process can help to overcome this situation. In Figure 3.1 our present understanding of a semi-inclusive DIS process (3.1) is shown in more

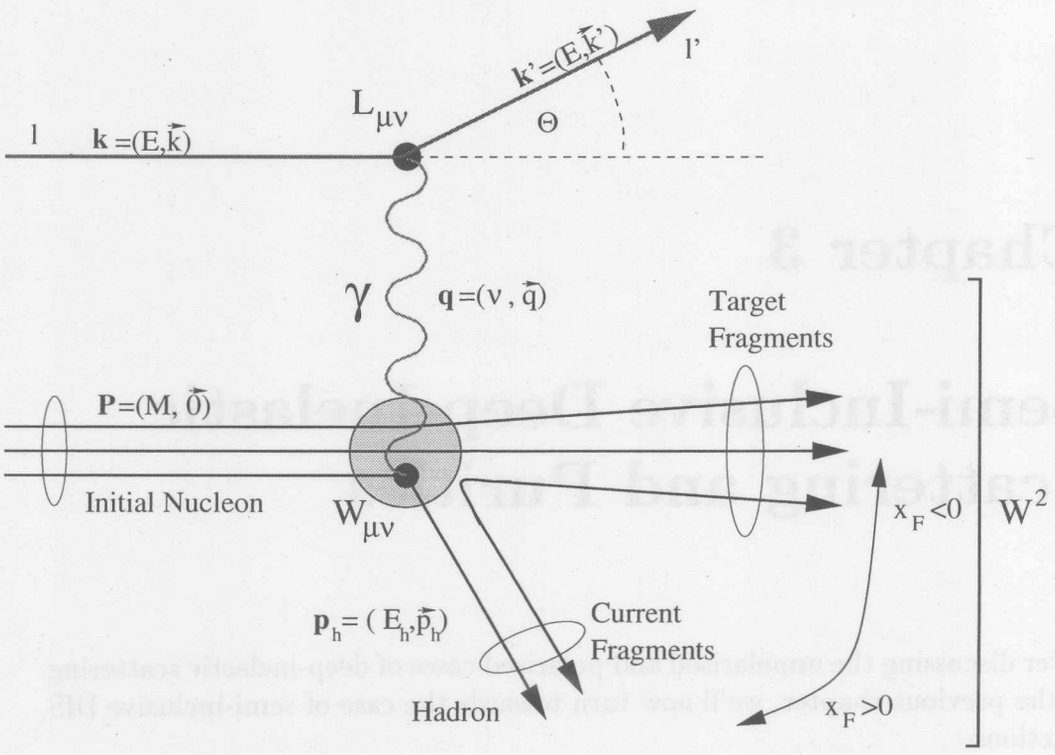

Figure 3.1: Schematic Picture of a Semi-Inclusive DIS Process at HERMES energies. *In this sketch the nucleon is not drawn to scale (too small) for more clarity (see also Figure 2.1). The nucleon breaks up into fragments escaping parallel to its initial momentum ("target region") and other hadrons more collinear with the direction of the photon ("current region"). In the QPM the hadronic tensor is resolved to the electromagnetic interaction of the photon and a charged quark.*

detail in the framework of the QPM. Table 3.1 defines the most important semi-inclusive kinematical variables, that are used in the following.

3.2 Fragmentation Functions

The cross-section for the semi-inclusive process (3.1) with a hadron h in the final state is given by

$$\begin{aligned} \frac{d^3\sigma_h}{dxdQ^2dz}(x,Q^2,z) &= \frac{\sum_q e_q^2 q(x) D_q^h(z)}{\sum_q e_q^2 q(x)} \cdot \frac{d^2\sigma}{dxdQ^2}(x,Q^2) \\ &= C(x,Q^2) \cdot \sum_q e_q^2 q(x) D_q^h(z), \end{aligned} \tag{3.2}$$

Semi-Inclusive Observables	
Variable	Name
E_h	Hadron energy
$\vec{p}_h$	Hadron momentum and direction

Derived Variables		
Variable	Definition	Name
z	E_h/ν	Fractional energy of a hadron in lab frame
$\boldsymbol{p}_{\parallel}$	$\frac{\boldsymbol{p}_h \boldsymbol{q}}{\sqrt{\boldsymbol{q}^2}}$	Parallel and transverse momentum
$\boldsymbol{p}_T$	$\boldsymbol{p}_h - \boldsymbol{p}_{\parallel}$	of hadron in γN frame with respect to $\boldsymbol{q}$
x_F	$\left(2\lVert\boldsymbol{p}^2_{\parallel}\rVert/\sqrt{W^2}\right)_{c.m.}$	Feynman's scaling variable

Table 3.1: Definition of the Semi-Inclusive Kinematical Variables as used in this text. *See also Figure 3.1.*

where we introduce the fragmentation functions $D_q^h(z)$ as the number density to produce a hadron h with the energy fraction $z \overset{\text{lab}}{=} E_h/\nu$ after a quark of flavour q was struck. The fact that the fragmentation functions (and hence the hadronisation) do not depend on any kinematical variable characteristic of the inclusive process (e.g. x and/or Q^2) expresses the assumption that the two processes are independent of each other and is called factorisation. Factorisation is a direct consequence of quasi-free partons in the QPM. The mean hadron multiplicity n^h per event is calculated by integrating

$$\frac{d^3 n^h}{dx dQ^2 dz}(x, Q^2, z) = \frac{\sum_q e_q^2 q(x) D_q^h(z)}{\sum_q e_q^2 q(x)}, \tag{3.3}$$

over the kinematical region of interest.

The number of fragmentation functions $D_q^h(z)$ can be reduced significantly by the application of iso-spin and charge symmetry. In this approximation only three functions are necessary to parametrise the generation of pions:

$$\begin{aligned} D^+(z) &= D_u^{\pi^+}(z) = D_{\bar{d}}^{\pi^-}(z) = D_{\bar{d}}^{\pi^+}(z) = D_{\bar{u}}^{\pi^-}(z), \\ D^-(z) &= D_{\bar{d}}^{\pi^+}(z) = D_{\bar{u}}^{\pi^-}(z) = D_{\bar{u}}^{\pi^+}(z) = D_{\bar{d}}^{\pi^-}(z), \\ D_s(z) &= D_{\bar{s}}^{\pi^+}(z) = D_{\bar{s}}^{\pi^-}(z) = D_{\bar{s}}^{\pi^+}(z) = D_{\bar{s}}^{\pi^-}(z). \end{aligned} \tag{3.4}$$

$D^+(z)$ and $D^-(z)$ are called favoured and unfavoured fragmentation functions and have been measured by EMC [EMC89a] and by HERMES [Gei98]. Since the probability to produce a hadron that contains the struck quark is higher than producing one that does not contain it, $D^+(z) > D^-(z)$ is true for all z

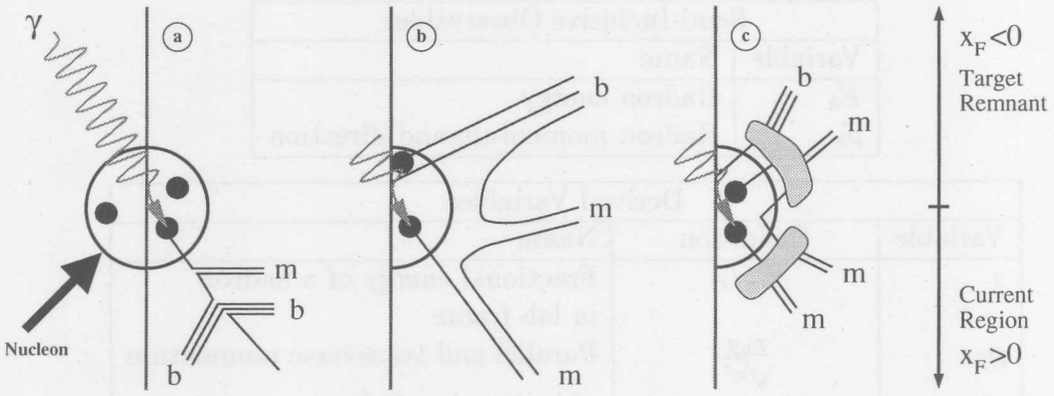

Figure 3.2: Schematic Picture of Different Fragmentation Models.
a) Independent fragmentation, b) LUND *string model, c) Cluster Fragmentation. Mesons in the final state are marked with m while Baryons are denoted by b.*

values.

3.3 Fragmentation Models

While the initial scattering of the struck quark happens at such high energies that perturbative methods can actually be used to calculate the QCD processes, the energy during the hadronisation becomes too low to permit an accurate modelling of the fragmentation functions from first principles. For this reason different physically motivated fragmentation models are used to implement Monte Carlo hadron generators (Figure 3.2). The parameters of the models are tuned such that the generated particle and momentum spectra match the observed data. In the following a short introduction for the three most commonly used models is given.

3.3.1 Independent Fragmentation

One of the first attempts to describe the fragmentation process was made by Field and Feynman with the independent fragmentation model [FF78]. This model is based on the assumption, that each parton fragments in an independent cascade by picking up $q\bar{q}$-pairs from the vacuum until a certain energy threshold is reached (Figure 3.2 a). It is parametrised by one parameter controlling the scaling function $f(z)$ which gives the probability that a energy fraction z is left to the remaining cascade after a $q\bar{q}$-pair pair was produced. The probability to produce a quark of a certain flavour is parametrised by

the parameters $\gamma = \gamma_u = \gamma_d$ and γ_s, with $2\gamma + \gamma_s = 1$. By measuring the K/π-ration, γ is found to be 0.435 which is equivalent to $\gamma_s = 0.3\gamma$ [EMC84]. A third parameter $< p_\perp^2 >$ controls the width of the transverse momentum distribution of the quark pairs, which is assumed to be Gaussian.

The model then predicts the ratio of unfavoured and favoured fragmentation functions to be

$$\frac{D^-(z)}{D^+(z)} = \frac{\gamma(1-z)}{z+\gamma(1-z)}, \tag{3.5}$$

which is supported by experimental data.

Even if the independent fragmentation model describes many features of the hadronisation with good precision, it is not really satisfactory. The model does not conserve the colour and flavour quantum numbers, because the last quark below the energy cut-off is simply neglected. Furthermore it can be shown that the model is not Lorentz invariant since momentum is not conserved when changing into a different reference frame. Also the particle multiplicities depend on the reference frame. For these reasons, more consistent models have been developed.

3.3.2 The LUND String Model

The underlying idea of the LUND string model [AG83] is similar to the Field-Feynman model. Here the struck parton is not treated independently but is connected via the colour field to the target remnant. Due to the fact that gluons are colour charged and therefore attract each other, this field is concentrated along a tube which is called a string. If the energy stored in the string exceeds the mass of a $q\bar{q}$-pair, a pair is produced and the string is divided in two substrings which now fragment independently until a colourless hadron on the mass shell is produced (Figure 3.2 b). The main parameters of this model are: The flavour production ratios (equivalent to the γs in the independent fragmentation model), the ratio between quark and diquark production, which controls the production ratio of mesons and baryons, a parametrisation of the string breaking probability (a,b) and the width of the $p_\perp$ distribution [Gei98].

The LUND string model is invariant under Lorentz transformations and conserves all quantum numbers. In this sense it is a consistent model for hadronisation and was used in form of the JETSET library [Sjö94] for most of the Monte Carlo studies in this work. The parameters of the model (which are by default optimised to describe the high-energy data of LEP and HERA) were tuned so that the hadron spectra at HERMES energies are described.

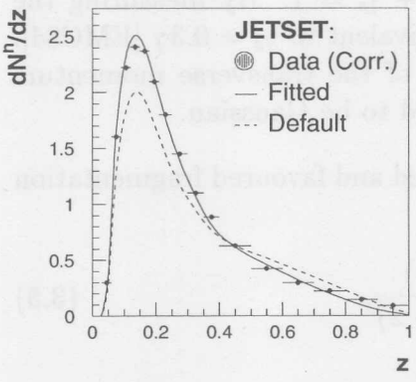

Parameter		default	fitted
a	(PARJ(41))	0.30	0.82
b	(PARJ(42))	0.58	0.24
$< p_\perp^2 >$	(PARJ(21))	0.36	0.34

Figure 3.3: Fitted LUND Fragmentation Parameters. *The left plot shows the generated hadron spectrum for the default* JETSET *parameters and for the fitted parameters in comparison to the measured distribution (which is corrected for the acceptance of the* HERMES *spectrometer). The table to the right shows the numerical values of the fitted parameters. For a description of the parameters see text.*

Figure 3.3 shows the hadron spectrum generated by JETSET for the default parameters and for the parameters fitted to match the HERMES experimental results [Gei98].

3.3.3 Cluster Fragmentation

As opposed to the Field-Feynman and the LUND fragmentation models, the cluster model attempts to describe the hadronisation process by the application of QCD perturbation theory as long as possible rather than parametrising it [MW92]. In the first step, the virtual partons coming from the photon-parton interaction form colour-neutral clusters of low virtuality (Figure 3.2 c). This process, called preconfinement, is calculated in the leading-logarithmic approximation (LLA). In the second step, the resulting clusters produce the observed hadrons by simple phase space decays. The cluster fragmentation model has the advantage that it is more theory-driven and does not need ad-hoc parametrisations like the other models. Adjustable parameters are the parton masses, the QCD scale parameter Λ_0 and the maximum cluster mass. Although high-energy data was successfully described by the cluster model, the model could not yet be tuned to describe the hadron spectra observed at HERMES energies well enough [Gei97].

3.4 Hadron Asymmetries

In analogy to the inclusive case, the measured semi-inclusive asymmetry of a hadron h is defined as

$$A_{\parallel}^{h} = \frac{\sigma_h(180°) - \sigma_h(0°)}{\sigma_h(180°) + \sigma_h(0°)} \tag{3.6}$$

where we used the naming convention of Section 2.5. Further more we define

$$\begin{aligned} g_1^h(x,z) &= \frac{1}{2}\sum_q e_q^2 D_q^h(z)\Delta q(x), \quad \text{and} \\ F_2^h(x,z) &= 2x\frac{1}{2}\sum_q e_q^2 D_q^h(z) q(x), \end{aligned} \tag{3.7}$$

as an extension of the inclusive case and can then use (2.29) to express the following relation between the polarised and unpolarised parton density functions, the fragmentation functions and $A_{\parallel}^{h}(x,z)$:

$$\frac{\sum_q e_q^2 D_q^h(z)\Delta q(x)}{\sum_{q'} e_{q'}^2 D_{q'}^h(z) q'(x)}\left[1 + R(x,Q^2)\right] = \frac{A_{\parallel}^{h}(x,z)}{D}, \tag{3.8}$$

where we assumed $A_2^h = 0$ as in the inclusive case. For future use we define the measured longitudinal asymmetries corrected with the depolarisation factor as

$$A^h(x,z) = \frac{A_{\parallel}^{h}(x,z)}{D}, \tag{3.9}$$

where $A^{e^+}(x)$ shall denote the inclusive case. Note that in the QPM model the hadron spin asymmetries do not depend on Q^2.

3.5 QCD Correction and PDF Sets

Relation (3.8) between the (un)polarised parton density functions defined in the QPM and the measured particle asymmetries were derived by correcting the naive QPM with the factor $(1 + R)$ which in this context can be understood as a factor taking into account higher order QCD effects (see Figure 3.4) as well as corrections to the Breit-approximation. We used equation (2.12) to relate the measured unpolarised structure function F_2 to the parton density functions (Deep Inelastic Scattering (DIS) factorisation/renormalisation scheme [ESW96]). For a consistent analysis it is important to use PDF sets

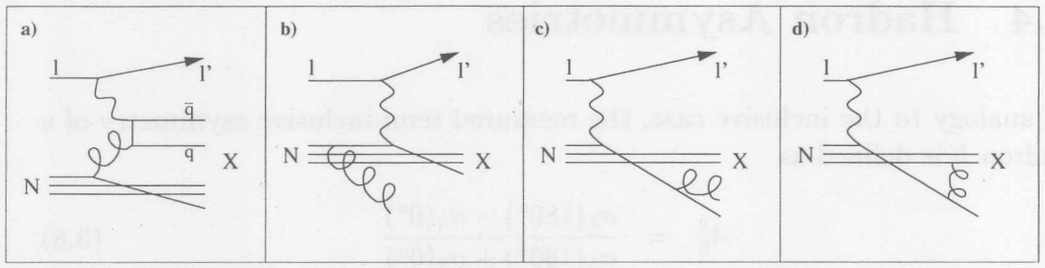

Figure 3.4: QCD Corrections. *a) Boson-gluon fusion b) Gluon bremsstrahlung in initial state, c) Gluon bremsstrahlung in final state, d) Gluon exchange between struck quark and spectator quark (higher-twist corrections).*

that are extracted under the same assumption, which is the case for the leading order fits published by [GRV95, GRSV95]. Although the authors actually parametrise F_1 by the PDFs and apply then QCD corrections to fit the measured F_2 data, in case of the leading order (LO) parametrisations the QCD corrections only imply heavy quark (charm) contributions, which are negligible at HERMES energies. This means that the Callan-Gross relation (2.9) holds and we can insert the leading order PDFs in (2.12).

3.6 Definition of Purities

Remember that the hadron asymmetries can be related to the polarised and unpolarised parton density functions by equation (3.8). We now use definition (3.9) and rearrange the terms in the following way:

$$\begin{aligned} A^h(x,z) &= (1+R)\frac{\sum_q e_q^2 D_q^h(z)(q^+(x)-q^-(x))}{\sum_{q'} e_{q'}^2 D_{q'}^h(z)(q'^+(x)+q'^-(x))} \\ &= (1+R)\sum_q \frac{e_q^2 D_q^h(z)q(x)}{\sum_{q'} e_{q'}^2 D_{q'}^h(z)q'(x)}\frac{\Delta q(x)}{q(x)}. \end{aligned} \tag{3.10}$$

This suggests that one can define the hadron purity $P_q^h(x,z)$ as the probability that a quark of flavour q was struck in an event in whose final state a hadron h with the energy fraction z was observed, namely

$$P_q^h(x,z) = \frac{e_q^2 D_q^h(z)q(x)}{\sum_{q'} e_{q'}^2 D_{q'}^h(z)q'(x)}. \tag{3.11}$$

Now we can express the following master relation between hadron asymmetries and the ratios of polarised and unpolarised parton density distributions, which

in the following will be called quark polarisations:

$$A^h(x,z) = (1+R)\sum_q P_q^h(x,z)\frac{\Delta q(x)}{q(x)}. \tag{3.12}$$

Obviously the following relation for the purities holds for every (x,z)-bin:

$$\sum_q P_q^h(x,z)dz = 1. \tag{3.13}$$

Furthermore a pseudo-purity can be defined for the scattered lepton by setting $D_q^{e^+} \equiv 1$ to include the inclusive asymmetries in the analysis formally. In this sense the index h might also be read as e^+ in the following text.

In practice the lack of statistics makes it impossible to measure the hadron asymmetries in (x,z)-bins. However, since the set of quark spin distributions to be extracted, $\{\Delta q_i(x)/q_i(x)\}_{i=1,\cdots,n}$, does not itself depend on z, it is sufficient to integrate all hadron particle numbers that are found in a fixed z-range to calculate a set of overall asymmetries $\{A^{h_i}(x)\}_{i=1,\cdots,m}$. Of course one has then to use the same hadronic cut and summing for the generation of the purities $P_q^h(x)$ (see Section 6.1).

The actual extraction of the quark polarisations is finally done by solving the following system of linear equations

$$\boldsymbol{A} = (1+R)\boldsymbol{\mathcal{P}}\boldsymbol{Q}, \tag{3.14}$$

for each bin in x, where we use the notation

$$\boldsymbol{A} = \begin{pmatrix} A^{h_1}(x) \\ \vdots \\ A^{h_m}(x) \end{pmatrix}, \quad \boldsymbol{Q} = \begin{pmatrix} \Delta q_1(x)/q_1(x) \\ \vdots \\ \Delta q_n(x)/q_n(x) \end{pmatrix}, \quad \boldsymbol{\mathcal{P}} = \left[P_q^h(x)\right]. \tag{3.15}$$

Here $\boldsymbol{A}$ is the vector of measured particle asymmetries, $\boldsymbol{Q}$ is the vector of quark polarisations and $\boldsymbol{\mathcal{P}}$ is the purity matrix. As we will discuss in Chapter 6, this system of equations can be over-determined. In this case its inversion is a linear fit.

3.7 Summary

In the previous chapter an introduction to the formalism of semi-inclusive deep-inelastic scattering was given mainly for the polarised case. It was shown by introducing new unpolarised quantities, the quark hadron purities, that the

experimental semi-inclusive asymmetries can be related directly to the central polarised entities of the quark parton model, the polarised parton density functions. The measurement of these quantities is the main topic of this work and will be presented in Chapter 6. But before reaching this main point, in the following two chapters the experimental setup of HERMES will be introduced as an apparatus designed to do asymmetry measurements (Chapter 4) and the measurement of particle asymmetries (Chapter 5) will be discussed.

Chapter 4

Experimental Setup

Designed to do precision measurements of spin effects, HERMES makes use of two modern techniques: A polarised electron storage ring and a polarised internal gas target in a windowless storage cell. The HERMES detector is located in the east section of the HERA electron-proton collider facility at DESY in Hamburg, Germany (Figure 4.1). While HERA is able to deliver polarised electrons, it is not yet able to accelerate polarised protons. As a consequence HERMES employs a fixed target and only utilises the polarised 27.5 GeV electron/positron beam, while the unpolarised 820 GeV proton beam

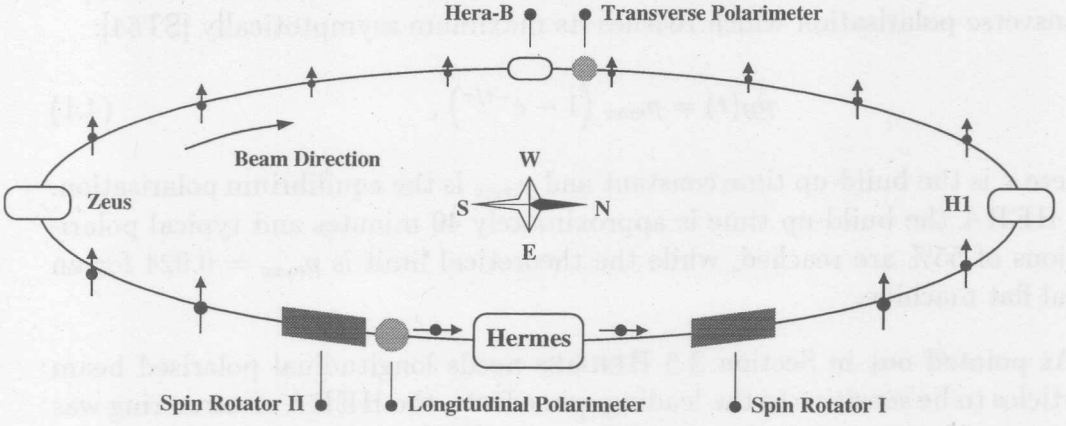

Figure 4.1: Location of HERMES at HERA. *In this diagram the positions of the four* HERA *experiments in the straight sections of the electron storage ring are shown. The spin of the electrons is symbolised by the small arrows. Two spin rotators supply* HERMES *with an electron beam of longitudinal spin direction. The beam polarisation is measured by two beam polarimeters. The proton ring as well as the booster rings are not drawn.*

passes through the apparatus without interaction. In the other experimental zones HERA hosts three other experiments. The two collider experiments ZEUS and H1 are using both beams to study unpolarised deep inelastic scattering at high energies ($\sqrt{s} = 300$ GeV) in a kinematical region that is not accessible for fixed target experiments. The last is HERA-B, the youngest experiment at HERA. Running as a test-experiment in 1997 its goal is to scatter halo-particles of the proton beam on target wires to produce and study B-mesons.

Due to lifetime problems caused by positive ions being attracted into the electron beam, HERA operated with positrons in the years 1995-97. Since (in lowest order QED) this means no difference for the fundamental physical processes at HERMES-energies, we refer to an electron beam in this text. However, it should be noted that the electro-weak processes under study at ZEUS and H1 are sensitive to the lepton charge and that therefore the vacuum system will be upgraded during an extended shutdown in 1998. The HERA electron beam consists of 220 bunches and reached maximum currents of about 30 mA in 1995 and 35 mA in 1996.

4.1 The polarised HERA-Positron-Beam

As a consequence of the small asymmetric spin flip amplitude in synchrotron radiation known as SOKOLOV-TERNOV effect, the electron beam builds up a transverse polarisation which reaches its maximum asymptotically [ST64]:

$$p_B(t) = p_{max}\left(1 - e^{-t/\tau}\right), \tag{4.1}$$

where τ is the build-up time constant and p_{max} is the equilibrium polarisation. At HERA the build-up time is approximately 40 minutes and typical polarisations of 55% are reached, while the theoretical limit is $p_{max} = 0.924$ for an ideal flat machine.

As pointed out in Section 2.5 HERMES needs longitudinal polarised beam particles to be sensitive to the leading spin effects, the HERA electron ring was augmented by two spin rotators which are designed to change the spin direction of the beam from transverse to longitudinal in front of the experimental section and vice versa behind it (see Figure 4.1). A schematic diagram of one rotator is shown in Figure 4.2. By changing the polarity of the vertical bending dipoles the helicity of the electron beam at the interaction point can be reversed. However this means that the vertical orbit is changing about 45 cm and that the beam line in this section has to be movable.

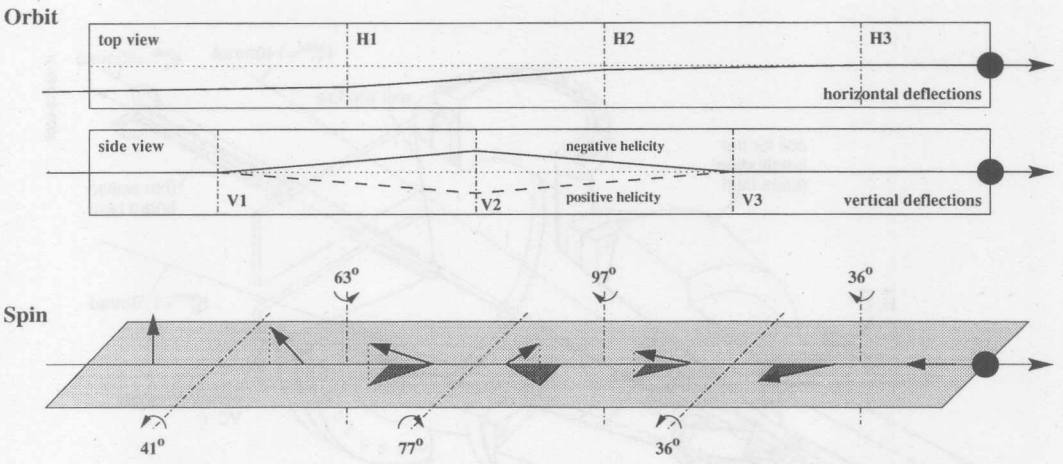

Figure 4.2: Schematic Diagram of a Spin-Rotator [BS86]. *Here the setup of the horizontal and vertical bending magnets are shown together with their influence on the electron orbit and the corresponding spin precession angles. Due to relativistic effects described by the* THOMAS-BARGMANN-MICHEL-TELEGDI *equation [Tho27, BMT59], the spin precession in a magnetic field at the* HERA *electron beam energy is* 63.5 *times larger than the orbital bending. Since rotations are non-commutative in three dimensions it is possible to rotate the spin by* 90° *while the orbit is unchanged. The size of the vertical bump is about* 22 *cm, the length of the whole system roughly* 70 *m.*

The beam polarisation is measured by two Compton polarimeters scattering circularly polarised laser light off the beam. The transverse polarimeter is located in the west section of HERA and uses the fact that the Compton cross section on transverse polarised leptons shows a spin-dependent azimuthal distribution. The laser intensity is chosen such that in average only 0.01 photon is backscattered per bunch (single-photon method). The centre of gravity of this photon is then measured in a position sensitive calorimeter and the top-bottom asymmetry of the position distribution can be used to derive the beam polarisation [Dür95, Oel95]. Since 1997 a second polarimeter in the east section directly measures the longitudinal polarisation of the beam near the HERMES interaction point. This polarimeter works with a different measurement principle than the transverse one. It uses the spin-dependent angular distribution of the Compton cross section on longitudinal polarised leptons which translates into a spin-dependent energy spectrum. By using laser pulses of high intensity several thousand photons are backscattered per bunch and their energy weighted spin asymmetry can be used to measure the beam polarisation [Lor95].

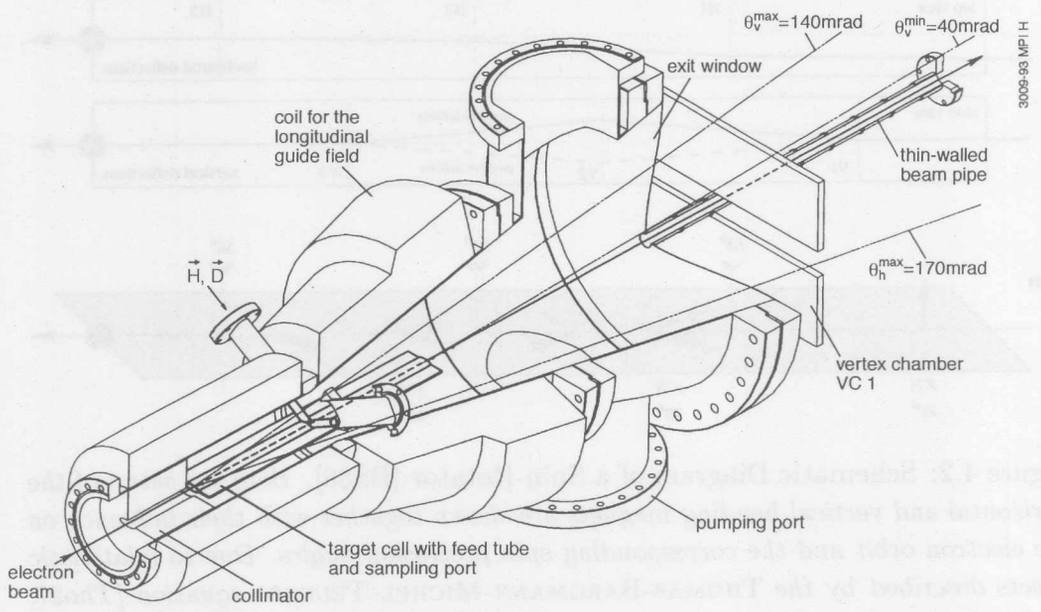

Figure 4.3: The Target Section. *The* HERA *electron/positron beam enters the setup from the left and passes through the target storage cell. The scattered lepton as well as the products of an interaction leave the vacuum through a thin exit window which is immediately followed by the first tracking device. The non-interacting leptons continue their orbit in a thin-walled section of the beam pipe. This picture is a design study and does not reflect the actual setup in detail.*

4.2 The polarised Targets

In contrast to polarised fixed target experiments using an external beam, a storage ring obviously makes it impossible to use solid or liquid polarised targets. Such targets are usually built of mixed materials where only a fraction of the atoms are polarised while the others stay unpolarised and introduce a low dilution factor. Furthermore massive cell windows might be necessary, which (in addition to the high target density) potentially cause multiple scattering and energy loss of particles originating from a scattering process.

At HERMES the technique of an internal gas target is used by inserting a thin storage cell in the HERA electron ring as shown in Figure 4.3. This target cell is fed by a polarised gas source and builds up a triangular density distribution. It is made out of very pure aluminium with an uniform wall thickness of about 100 μm to reduce kinematical smearing. The cell walls are cooled in order to increase the target density by reducing the velocity of the target atoms. The low density of an internal target is compensated by

	Type of Target	
	^{3}He	H (ABS)
Year of Operation	1995	since 1996
Polarisation	46%	99%
Thickness	10^{15} nucleons/cm^2	$3.5 \cdot 10^{14}$ atoms/cm^2
Source intensity	$1 \cdot 10^{17}$ atoms/s	$6 \cdot 10^{16}$ atoms/s
Working Principle	Optical Pumping	Stern-Gerlach, Hyper-Fine Transitions
Polarimeter	Optical	Breit-Rabi
Total Error	$\pm$5% (fractional)	$\pm$7% (fractional)[a]
Switching Time	10 min	45 s[b]
Cell temperature	20 K	100 K
Holding field	3.2 mT	335 mT
Cell coating	—	Dri-film

[a]This error is dominated by the systematical uncertainty of the molecular polarisation and can be reduced by using reference A_1^p data to calibrate the product of beam and target polarisation.

[b]The ABS can reach switching times below a second. In 1996 a slower target cycle was chosen to guarantee a constant target spin orientation during a 10 second data acquisition interval called a "burst".

Table 4.1: Specifications of Targets used at HERMES.

the fact that it consists of pure gas atoms and hence has a low fraction of unpolarised material (high dilution factor). To avoid heating of the storage cell and particle shower development at the cell walls, the target region is carefully shielded against synchrotron light and beam halo particles by both fixed and movable collimators.

Aside from an unpolarised gas feed system that is able to deliver unpolarised gases over a wide density range, two different kinds of setups can be used to realize polarised hydrogen, deuterium and ^{3}He targets. Both target systems are completed by a target polarimeter and a target magnet generating a longitudinal holding field for the polarised atoms. The features of the targets used in 1995 and 1996 are summarised in Table 4.1.

4.2.1 ^{3}Helium Target

In 1995 the polarised ^{3}He target was installed at the HERMES interaction point to study the polarised structure function of the neutron. In this setup the target gas is stored at low pressure in an intermediate pumping cell made out of quartz glass. A weak electrical RF discharge excites a small fraction of the

atoms to the meta-stable state (2^3S_1) which then is optically pumped to a higher level (2^3P_0) by circularly polarised laser light traversing the pumping cell. The excited states decay back to the meta-stable level by isotropic emission of unpolarised light, or in other words, the polarisation of the pumping light is transfered to the meta-stable atoms. Hyperfine interactions in the excited state mix the spins of the electronic system and the nucleus so that the meta-stable sample gets nuclearly polarised. Finally, this nuclear polarisation gets transfered from the meta-stable to the ground state by the metastability exchange process, which is based on the exchange of the electron clouds between two atoms during an atomic collision. Neither the electron spin of each cloud nor the spin of each nucleus is changed by this process (while the de-excitation of the metastable state to the ground state does not conserve the nuclear polarisation). The polarised atoms are then injected in the target storage cell via a precision capillary. To maintain the polarisation axis of the target atoms, the whole target area is kept in a holding field provided by a pair of large Helmholtz coils. The target polarisation can be flipped by reversing the circular polarisation of the laser light [Sch97].

There are two ways to determine the polarisation of the ^{3}He target. In the Pump Cell Polarimeter (PCP) the circular polarisation of the light emitted by the discharge in the pumping cell is measured. Via a calibration relation the nuclear polarisation of the atoms can be derived [Lee93]. Due to the chemical inactivity of Helium the depolarising effects in the capillary and cell are assumed to be small and are neglected. Furthermore the storage cell does not need a special coating and can be cooled down to 20 K.

An independent method to measure the polarisation of the ^{3}He atoms directly inside the storage cell is provided by the Target Optical Monitor (TOM). The HERA electron beam excites the gas in the target cell and via hyperfine coupling the nuclear polarisation is transfered to the electronic system which then emits circularly polarised light. Part of this light is collected by a mirror located upstream in the beam pipe and then analysed, yielding a measure for the target polarisation. Within errors both methods give compatible results.

4.2.2 Atomic Beam Source

In 1996 the ^{3}He target was replaced by the polarised Atomic Beam Source (ABS) which provided a proton target (see Figure 4.4).

The ABS is based on the Stern-Gerlach principle. In a first stage molecular hydrogen is dissociated by RF discharge into atoms and an unpolarised beam is formed by a cooled nozzle and skimmers. The beam particles now enter a

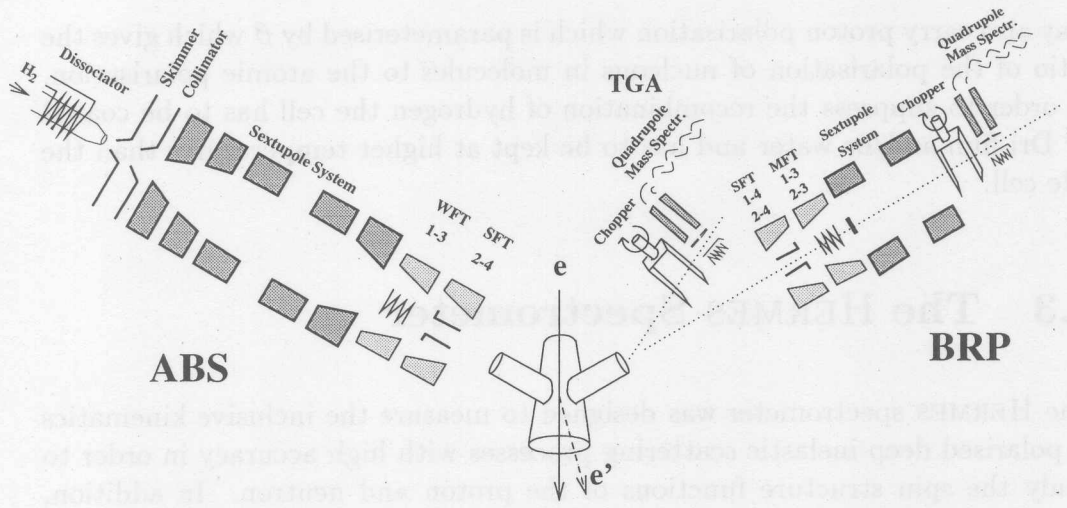

Figure 4.4: The HERMES Proton Target. *On the left side the Atomic Beam Source (ABS) prepares a nuclearly polarised proton beam which is injected into the storage cell. The right side shows two detectors for the analysis of a gas sample extracted from the cell: The Target Gas Analyser (TGA) measures the composition of this gas sample and the Breit-Rabi Polarimeter (BRP) measures its polarisation.*

sequence of strong sextupole magnets and are focused or defocused depending on their electron spin. Using high frequency transitions the population of selected hyperfine states can be exchanged and an atomic beam consisting of two hyperfine states with the same nuclear spin and opposite electron polarisation can be injected into the storage cell. The same setup can be used to generate polarised deuterium beams [Ste97].

The polarisation of the hydrogen atoms in the target cell is measured by a Breit-Rabi Polarimeter (BRP). A small fraction of target gas is extracted via a sample tube from the storage cell and fed into an apparatus that is basically the reverse setup of the ABS. At the position of the dissociator an atomic beam detector measures the intensity of the atomic beam. By switching the high frequency transitions, the population of selected hyper fine states and therefore the polarisation of the sample beam can be extracted [Bra97]. The BRP is augmented by a Target Gas Analyser (TGA) which measures the degree of dissociation α in the target cell by the ratio of hydrogen atoms and recombined hydrogen molecules. The polarisation p_T of the target nucleons in the cell is then related to the polarisation of the hydrogen atoms measured in the BRP p_{BRP} by

$$p_T = \alpha_0(\alpha + (1-\alpha)\beta) \cdot c_p p_{BRP} \tag{4.2}$$

where $1 - \alpha_0$ is the fraction of protons entering the cell in molecules and c_p is a sampling correction from calibrations. The recombined molecules in the cell

may also carry proton polarisation which is parameterised by β which gives the ratio of the polarisation of nucleons in molecules to the atomic polarisation. In order to suppress the recombination of hydrogen the cell has to be coated by Dri-film and/or water and has to be kept at higher temperatures than the ^{3}He cell.

4.3 The HERMES Spectrometer

The HERMES spectrometer was designed to measure the inclusive kinematics of polarised deep-inelastic scattering processes with high accuracy in order to study the spin structure functions of the proton and neutron. In addition, hadronic products of the scattering can be reconstructed over a wide kinematical range.

Since both HERA storage rings traverse the HERMES spectrometer, the detector was split into an upper and lower half mounted symmetrically above and below the beam lines which are shielded from the magnetic field of the spectrometer by a septum plate. Figure 4.5 shows the layout of the spectrometer which is divided into three main parts. The front region is solely instrumented with tracking devices to record the scattering angle without imposing much material that would smear the electron momentum by multiple scattering. The main spectrometer magnet is used for deflecting charged tracks according to their momentum and houses some tracking chambers to help the matching of tracks reconstructed in the front and back regions. The back region consists not only of tracking chambers but also has a variety of detectors used for trigger and particle identification purposes.

4.3.1 Tracking Detectors

The HERMES tracking system consists of gas-micro-strip chambers and drift chambers in the front region, proportional chambers in the magnet and two sets of drift chambers in the back region. The parameters of the tracking devices are summarised in Table 4.2. The main spectrometer magnet provides an integrated field of 1.3 Tm for the momentum measurement. A horizontal septum plate augmented with compensator coils is mounted in the middle plane of the magnet to prevent distortions of the HERA beams by the dipole field. The angular acceptance in the front region covered by the opening of the magnet gap is 40 mrad$< |\theta_y| <$140 mrad vertically and $|\theta_x| <$170 mrad horizontally. The horizontal acceptance in the back region is increased to 270 mrad so that particles with an momentum of >2 GeV/c can be fully

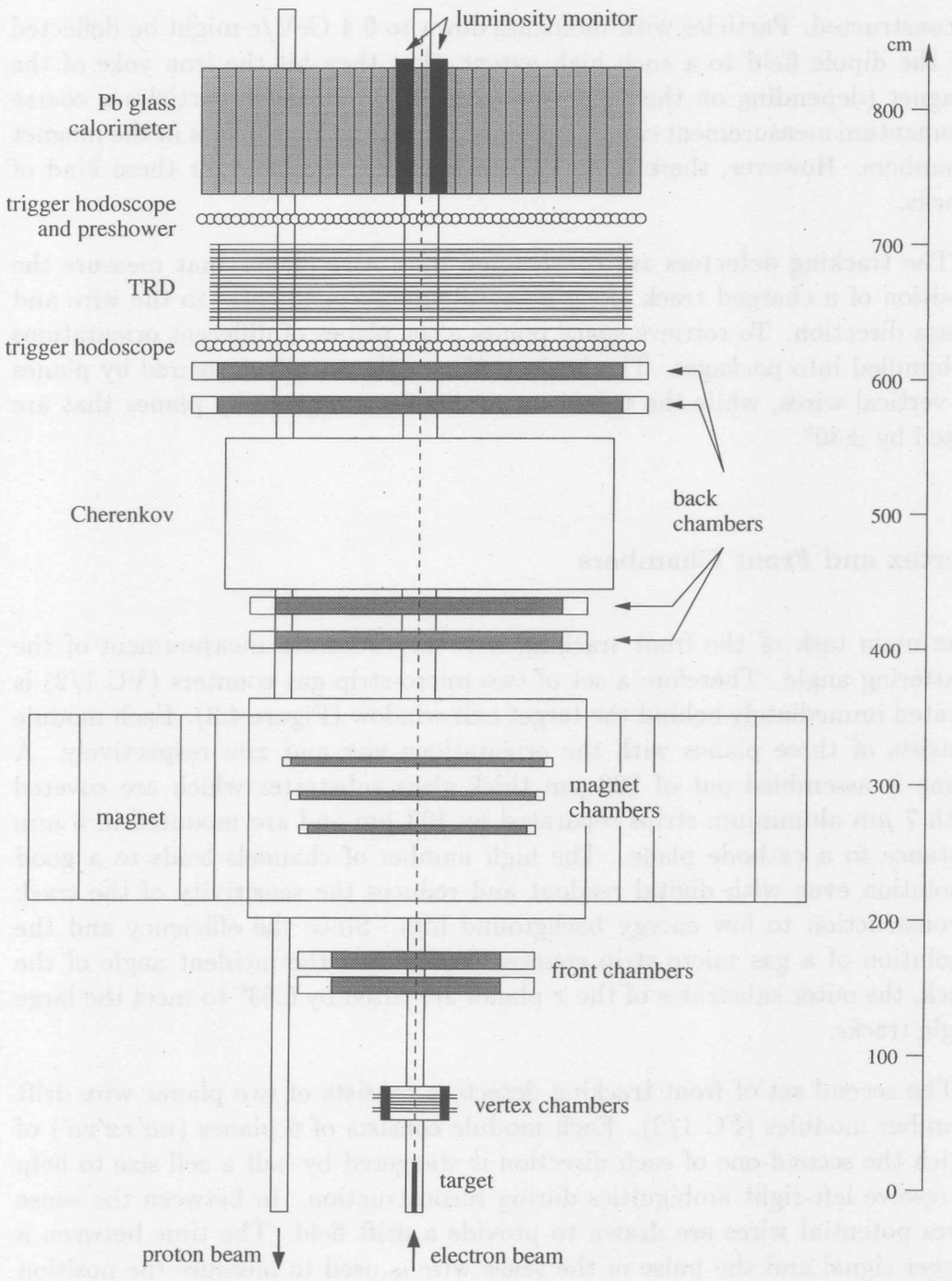

Figure 4.5: Top view of the HERMES Setup. *The tracking devices are labelled on the right side. Detectors for trigger and particle identification are labelled on the left side. The iron yoke of the magnet is roughly 5 m wide and 4.5 m high.*

reconstructed. Particles with momenta down to 0.4 GeV/c might be deflected by the dipole field to a such high extent, that they hit the iron yoke of the magnet (depending on their entrance position). For those particles a coarse momentum measurement can be provided by evaluating the hits in the magnet chambers. However, there is no PID information available for these kind of tracks.

The tracking detectors are constructed from wire planes that measure the position of a charged track along a coordinate perpendicular to the wire and beam direction. To retrieve space points a set planes of different orientations is bundled into packages. The horizontal coordinate x is measured by planes of vertical wires, while the u and v coordinates are given by planes that are tilted by $\pm 30°$.

Vertex and Front Chambers

The main task of the front tracking is a very accurate measurement of the scattering angle. Therefore a set of two micro-strip gas counters (VC 1/2) is located immediately behind the target exit window (Figure 4.3). Each module consists of three planes with the orientations vux and xvu respectively. A plane is assembled out of 300 μm thick glass substrates which are covered with 7 μm aluminium strips separated by 193 μm and are mounted in 3 mm distance to a cathode plane. The high number of channels leads to a good resolution even with digital readout and reduces the sensitivity of the track reconstruction to low energy background hits. Since the efficiency and the resolution of a gas micro strip counter depends on the incident angle of the track, the outer substrates of the x planes are tilted by 6.93° to meet the large angle tracks.

The second set of front tracking detectors consists of two planar wire drift chamber modules (FC 1/2). Each module consists of 6 planes ($uu'xx'vv'$) of which the second one of each direction is staggered by half a cell size to help to resolve left-right ambiguities during reconstruction. In between the sense wires potential wires are drawn to provide a drift field. The time between a trigger signal and the pulse in the sense wire is used to measure the position of the incident track in the cell by evaluating the Space Drift Time Relation (SDTR).

Although the vertex chambers had problems in 1995, it turned out that sufficient forward tracking can be done by the front chambers alone (plus corrections from the bridging to the backtracks). However, it was desirable to make the forward tracking less vulnerable to failing detectors by introducing

	Vertex		Front		Magnet			Back	
Detector	VC-1	VC-2	FC-1	FC-2	MC-1	MC-2	MC-3	BC-1/2	BC-3/4
Type	micro-strip gas		hor. drift		proportional			hor. drift	
Num. of planes	3	3	6	6	3	3	3	6/6	6/6
z-Pos. (mm)	727	972	1526	1637	2655	3060	3423	4150	5900
Active hor. (mm)	420	420	680	680	996	1216	1424	1888	2890
Active vert. (mm)	137	145	220	220	263	306	347	520	710
Cell size	193 μm		7 mm		2 mm			15 mm	
Resolution (nom.)	57 μm		150 μm		577 μm			150 μm	
Chamber gas	DME/CO_2		Ar/CF_4/CO_2		Ar/CF_4/CO_2			Ar/CF_4/CO_2	
Gas mix	60:40%		90:5:5%		65:5:30%			90:5:5%	
High Voltage	2 kV		1.4 kV		2.8 kV			1.75 kV	
Readout	digital (APC)		TDC		digital (PCOS)			TDC	
Channels (x)	1674	2046	96	96	496	608	720	120	192
Channels (u/v)	2170	2170	96	96	512	608	720	118	186
Rad. length	1.2%		0.20%		0.29%			0.26%	

Table 4.2: Design Parameters of the Tracking Chambers.

an additional set of drift vertex chambers (DVCs) in the gap between VCs and FCs. These chambers were commissioned in early 1997 and are included in the tracking since then.

Magnet Chambers

In the rear part of the magnet, where most of the low energetic background is deflected into the magnet yoke, three modules of proportional wire chambers are mounted. Each module consists of three planes with the orientations uxv which are build by two cathode foils enclosing a plane of anode wires with a wire distance of 2 mm. This setup results in a resolution of 2 mm/$\sqrt{12}$=0.577 μm. Although the information from the magnet chambers originally was only forseen to simplify the matching between the forward and backward tracks by applying a Kalman filter, it turned out that they can be used to reconstruct partial tracks and momenta of low energy particles.

Back Chambers

The tracking in the region behind the magnet is done by two sets of drift wire chambers that are very similar to the front chambers. Due to the high distance to the interaction point and the increased horizontal angular acceptance for particles deflected in the magnet, the active areas of the chambers are rather large. On the other hand, the cell size at that location can be wider since the separation of the two sets gives a good lever arm to reconstruct the angle

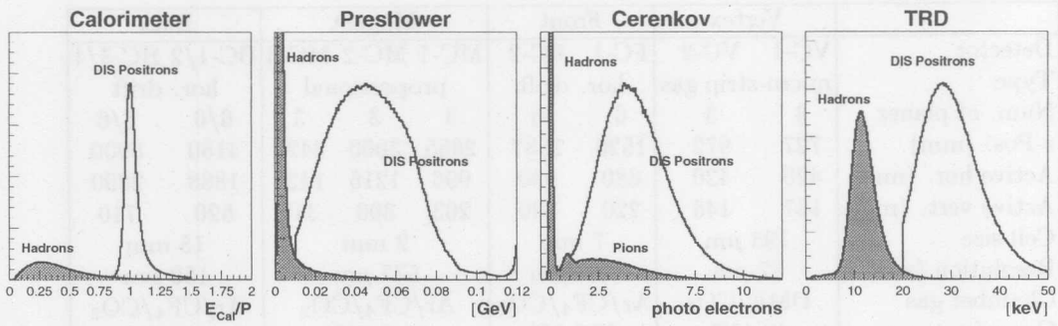

Figure 4.6: Signals of the Particle Identification Detectors. *In these plots the Monte Carlo results for the four particle identification detectors are shown for the samples of reconstructible hadrons and DIS positrons.*

of a track and the track density is lower. Each set of back chambers is two modules consisting of 6 planes ($uu'xx'vv'$) that are also staggered. Due to a well-known SDTR and a fast readout electronic with high time resolution, a spatial resolution of 250 μm can be achieved with a cell size of 15 mm.

4.3.2 Particle Identification

The particle identification (PID) system at HERMES consists of four components and was designed to identify the DIS electron with high efficiency and with low contamination from hadronic tracks.

A lead glass calorimeter and a preshower hodoscope allow the measurement of the energy deposit of particles and the use of the ratio E/p to distinguish between electron and hadron tracks. The Transition Radiation Detector (TRD) allows the separation of highly relativistic particles (high $\gamma = E/m_0$) from others while the Čerenkov counter identifies all particles above a certain velocity. Furthermore, it is possible to measure the masses of low-energy particles by time-of-flight methods using the hodoscopes. Since this is only possible for particles with momenta less than 2 GeV/c it is not discussed further.

The PID signals (see Figure 4.6) of the four components can be used in two ways. First, one can place hard cuts on the individual detector responses near the intersection of the distributions for electrons and hadrons. The exact position of the cut controls the efficiency and the contamination of the particle identification. Using this method the PID information of the components become independent and can be used to crosscheck and study single detectors. However for data analysis it is too inefficient. A more complex method defines for each detector the conditional probabilities $\mathcal{L}^{e,h}$ that a track is identified

as an electron or a hadron under the assumption that the detector signal was generated by this kind of particle. The conditional probabilities, $\mathcal{L}^{e,h}$, can be converted into true probabilities $\mathcal{P}^{e,h}$ by applying Bayes' theorem:

$$\mathcal{P}^i = \frac{\Phi^i \mathcal{L}^i}{\sum_j \Phi^j \mathcal{L}^j}, \tag{4.3}$$

where Φ^i are the true particle fluxes which might be a function of momentum and angle. Building the logarithmic ratio of the true probabilities for opposite hypotheses

$$pid = \log_{10} \frac{\mathcal{P}^e}{\mathcal{P}^h} = \log_{10} \frac{\mathcal{L}^e}{\mathcal{L}^h} + \log_{10} \frac{\Phi^e}{\Phi^h} \tag{4.4}$$

is a sensitive measure for the particle type, but one needs to have a Monte Carlo model for particle fluxes. However, if the flux ratio Φ^e/Φ^h depends only weakly on the kinematical variables, the second term in (4.4) is a constant offset and already the ratio of the conditional probabilities for a measured detector signal becomes a good PID information. For historical reasons the conditional probabilities of the calorimeter, preshower and Čerenkov counter are usually combined yielding a quantity called pid_3:

$$pid_3 = log_{10} \frac{\mathcal{L}^e_{Cal} \cdot \mathcal{L}^e_{Pre} \cdot \mathcal{L}^e_{Cer}}{\mathcal{L}^h_{Cal} \cdot \mathcal{L}^h_{Pre} \cdot \mathcal{L}^h_{Cer}}, \tag{4.5}$$

which allows, together with the TRD information, a very good separation of electrons and hadrons (see Figure 4.7). A more advanced scheme collects all four PID systems in one combined quantity but is not yet available for the helium data taken in 1995. Electrons can be identified with an overall efficiency of better than 98% with a hadronic contamination level of less than 1%. A detailed description of the HERMES PID scheme can be found in [Kai97].

Čerenkov Counter

If a particle passes through a medium with velocity larger than the speed of light in this medium, electromagnetic radiation (Čerenkov light) is emitted on a cone along the direction of the particle. In the threshold Čerenkov counter used at HERMES until 1997, the detection of photons along a track indicates that this particle travels with a relativistic β-factor[1] that is higher than $\beta_{\text{thr}} = 1/n$, where n is the optical density of the radiating material. The Čerenkov light is reflected by an array of 20 mirrors per detector half onto

[1]The relativistic β-factor is defined as the ratio of velocity to the speed of light in the vacuum: $\beta = v/c$.

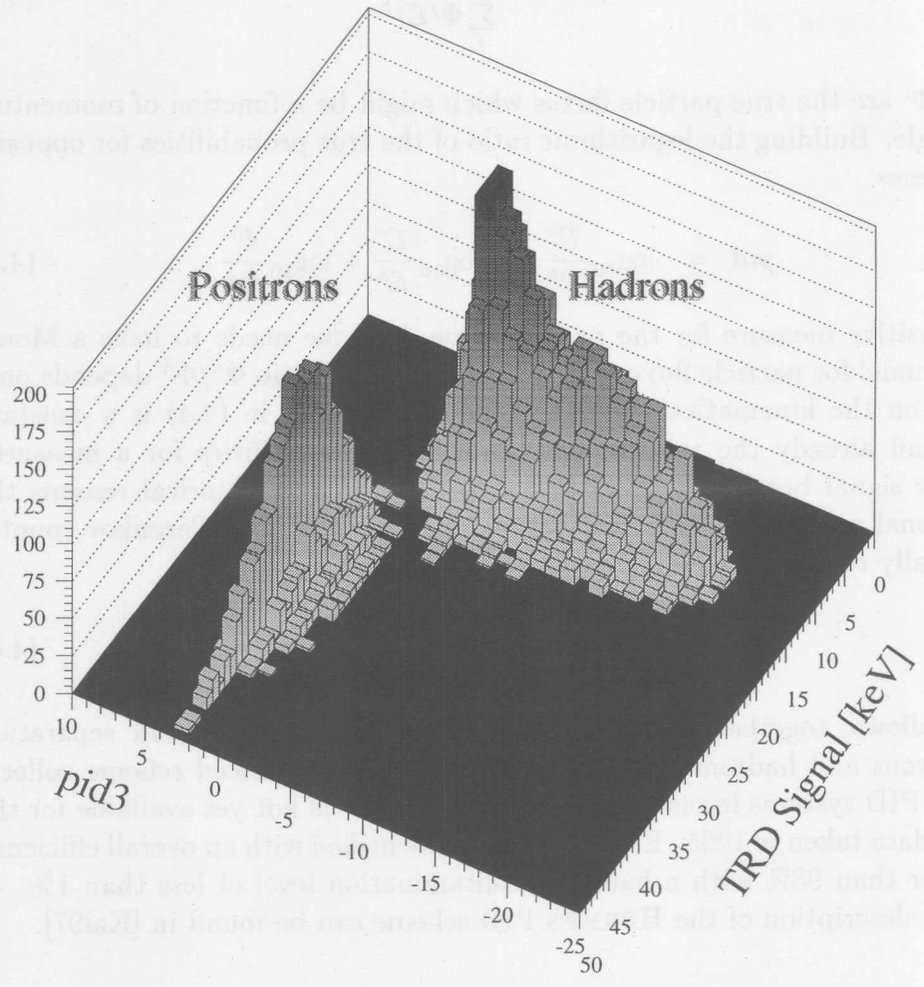

Figure 4.7: Combined PID Distributions. *In this graph the quantity pid_3 which is derived by definition (4.5) from combined conditional probabilities of the calorimeter, preshower, and Čerenkov counter is plotted against the TRD signal. By applying a cut on the linear combination of both quantities very good particle separation is possible. Because of the topology of the distributions this method is called a "valley-cut".*

Year	1995	1996
Radiator	N_2	N_2,C_4F_{10}
n	1.000298	1.001223
$p_{thr}(e^{\pm})$	0.021 GeV/c	0.015 GeV/c
$p_{thr}(\pi^{\pm})$	5.72 GeV/c	3.99 GeV/c
$p_{thr}(\mathrm{K}^{\pm})$	20.23 GeV/c	14.13 GeV/c
$p_{thr}(\mathrm{p})$	38.42 GeV/c	26.83 GeV/c

Table 4.3: Čerenkov Thresholds. *The change of the radiator gas lowered the pion momentum threshold by approximately 2 GeV/c (values from [Kai97]).*

corresponding photo-multipliers. The observed Čerenkov signals are assigned to reconstructed tracks.

In Table 4.3 the momentum threshold of various particles are listed for the radiator gases used in 1995 and 96. As one can see the Čerenkov counter can not only be used to do lepton hadron separation but also allows the identification of a pion sample in certain momentum windows. In 1995 the lower limit of this window was around 5.7 GeV/c while in 1996 it was lowered to 4 GeV/c in order to reach a higher yield of unambiguously identified pions.

In 1998 the Čerenkov counter will be replaced by an Ring Imaging Čerenkov counter (RICH) which will provide a much cleaner pion and kaon identification over the full momentum range by measuring the opening angle of the Čerenkov cone [Jac97].

Transition Radiation Detector

Transition radiation is emitted if a charged particle crosses the boundary of materials with different dielectric constants. In the ultra-relativistic case ($\gamma > 1000$) the photons are radiated in the forward direction and have an energy above several keV, while particles with lower γ-factor emit much softer photons with less total energy. Since a 5 GeV electron has a γ-factor of 10^4 compared to $\gamma = 36$ for a pion of the same energy, transition radiation can be used very efficiently to distinguish electrons and hadrons.

At HERMES the Transition Radiation Detector (TRD) consists of 6 identical modules per detector half, each one built of a 6.35 cm thick radiator and a 2.54 cm thick X-ray detector. The radiating volume is loosely filled with polyethylene/polypropylene fibres of a diameter of 17–20 μm surrounded by air. A multi-wire proportional chamber filled with a mixture of 90% Xe and 10% CH_4 is used to detect the generated photons in 256 channels per plane

and allows the assignment of the measured X-ray clusters to reconstructed tracks. Xenon was chosen as chamber gas because of its high X-ray absorption factor due to its large atomic charge. With this configuration a positron-pion rejection of more than 1:100 can be reached.

Calorimeter

The HERMES calorimeter consists of two halves of 42×10 modules each. The detector halves can be moved vertically to protect the detector from possible radiation damage caused by accidental beam loss during HERA fill preparation. Each of the 840 modules is build of a lead glass block of the dimensions 9×9×50 cm^3 and an attached photo-multiplier to detect the energy of produced photon showers. The energy resolution of the calorimeter for electrons was measured to be [Dür95]

$$\frac{\Delta E}{E} = 1.47\% + \frac{5.14\%}{\sqrt{E/\mathrm{GeV}}}. \tag{4.6}$$

The depth of a F101 glas block corresponds to 18 radiation lengths, which means that electrons will lose all their energy in the calorimeter. On the other hand, hadrons will deposit only a fraction of their energy in the calorimeter since their nuclear interaction length in lead glass is much longer. This means that the ratio of measured energy deposited[2] and reconstructed momentum will be ≈ 1 for electrons and < 1 for hadrons and can be used to distinguish the two particle classes. It should be noted, that a shower in the calorimeter can be spread out over more than one block and that the total cluster energy has to be summed up by a cluster-finding algorithm.

Hodoscopes

At HERMES two hodoscope walls are available. The first hodoscope (H1) consists of 2×42 scintillator paddles with attached photomultipliers and is mounted in front of the TRD. It is only used for trigger (and TOF) purposes since the radiation length of 2.3% does not allow a precise energy measurement. The second hodoscope (H2) is located behind the TRD and is designed as preshower counter. It consists of a 1.1 cm lead layer in front of a hodoscope plane identical to H1. While hadrons hardly produce showers in the lead wall and hence only produce a minimum ionising signal in the scintillator, there

[2]To be precise, the total energy deposited has to be used here, i.e. the energy seen in the preshower (which imposes also 2 radiation length, see next paragraph) has to be added to the calorimeter signal.

is enough material (two radiation length) available for electrons to produce showers that will deposit more energy in the scintillator. As in the calorimeter the ratio of measured shower energy and reconstructed momentum becomes a measure for the particle type.

4.3.3 Luminosity Monitor

To be able to compare the DIS cross sections of different target spin states, it is necessary to monitor the luminosity by a physically independent and spin-independent process to correct for variations in target thickness or beam position. At HERMES the luminosity monitor measures the rate of beam particles scattered on the electrons of the target atoms, which is a purely electrodynamic process (Møller/Bhabha scattering) that is well understood.

The detector is two calorimeter modules consisting each of 12 $NaBi(WO_4)_2$ crystals each with a corresponding photo-multiplier. The modules are small enough to fit into the gap of the main calorimeter and are moved close to the beam when stable HERA running conditions are established. The detector measures the coincidence of beam and target electron (and their energies) and has a very low background. The coincidence rate is about 130 Bq for a beam current of 20 mA and a ^{3}He target density of 10^{15} nucl/cm^2.

In 1996 the luminosity monitor was also used to crosscheck the calibration of the BRP. For this kind of measurements the ABS is operated in a mode where the average electron polarisation is not zero but high. Since the Bhabha scattering is spin dependent, the coincidence rate electrons and positrons seen in the calorimeters should show an asymmetry which is a measure for the average electron polarisation in the cell. The results of this analysis are compatible with the BRP measurements [Ben98].

4.3.4 Trigger

The HERMES first level trigger is operated in a very flexible way by using fast programmable logic units (PLUs). It makes use of discriminator signals derived from the hodoscopes, the Čerenkov counter and column-wise summed calorimeter signals. It uses the HERA electron bunch timing as main clock. The readout decision is made up within a few hundred nanoseconds. Besides trigger conditions for the detection of events that are of physical interest, a number of technical triggers are necessary to measure trigger efficiencies and to do background studies.

Physics Triggers

The main purpose of the first level triggers is to induce the readout of all detector components if an event of physical interest is detected. Therefore the central trigger requirement for DIS events is the detection of a scattered electron in the fast detectors. The following typical trigger conditions isolate these kind of events with high efficiency and low contamination by other processes. The coincidence of all four conditions is required for firing the trigger:

A cluster of 3.5 GeV was found in the calorimeter.
This condition is tested by summing up the calorimeter signals columnwise and requiring that the sum of two columns is above a limit. An energy threshold of 3.5 GeV is equivalent to a cut of $y < 0.87$ which is used to exclude kinematical regions with high radiative corrections (see Chapter 5.3.2 and Table 5.2). Since 1996 the trigger threshold has been lowered to the equivalent of a leptonic shower with an energy of 1.4 GeV. This has had an drastic influence on the trigger efficiency since now also hadronic showers can reach the trigger limit. This background is dominated by hadronic tracks coming from the collimators in front of the target[3].

A preshower signal is above a minimum ionising level.
This condition helps to suppress hadronic showers that deposited enough energy to fulfil the previous condition.

A signal in hodoscope H1 was found.
This makes sure that there was a full backtrack and helps to suppress photon background.

The signals fulfil timing conditions.
The main background source in the setup described so far comes from the HERA proton ring. Protons that leave the orbit and hit the proton beam pipe behind the experiment can produce hadronic showers of high energy which will enter the backside of the calorimeter. Since the protons pass the trigger detectors at different times than the electrons, a time windows set around the HERA electron clock suppress the proton background efficiently.

For further suppression of the proton background, in 1996 an additional hodoscope was installed in front of the magnet. There is also set of veto-scintillators around the proton beam pipe available, but it was not necessary

[3]In 1996 only one of 10 recorded events actually contained a positron. In this analysis a software cut of 3.5 GeV is applied to all data.

to include these detectors in the trigger condition. Typical trigger rates are in the order of 150 Bq with a target density of $1.2 \cdot 10^{15}$ nucl/cm^2 and a electron beam current of 30 mA. About half of this rate is induced by the proton background.

There are physical triggers for other kinds of analysis available. For instance it is possible to trigger on two low-energy tracks if one searches for decaying particles produced with low cross sections or at kinematical regions where the scattered electron is not entering the detector acceptance [MKP96]. Since these triggers are not relevant for this analysis they are not discussed here.

Gain Monitoring System

A special trigger is used by the Gain Monitoring System (GMS). All detectors using photo multipliers (hodoscopes, Čerenkov, calorimeter and luminosity monitor) are connected via glass fibres to a light source which can be attenuated and sends short light pulses with a wave length of 500 nm to the detectors. The photo multiplier signals are compared to the reference signal of a photo diode to detect variations in the detector gains and dead channels.

Higher Level triggers

The first level trigger described so far only produces a read out decision. Once the information of the other detectors is available, more complex trigger mechanisms can be set up using Digital Signal Processors (DSPs). It would be possible to check the TRD signals for the presence of an electron. Another possibility is the use of a trigger matrix to decide if hits in the hodoscopes and the calorimeter are actually defining a spatial track. This kind of trigger algorithms would be located on the event builder level and are called second level triggers. At HERMES a second level is presently not implemented although the technical prerequisites are available.

Once an event is built (i.e. all detector data is packed into a standardised event record) and transferred to the online hosts (see next section), it can be distributed to CPUs applying much more complex and slower algorithms than a second level trigger could do. For example a coarse front tracking could be done to suppress events that are triggered at low calorimeter thresholds by hadronic showers from the collimators.

4.3.5 Data Acquisition

The HERMES Data Acquisition system (DAQ) is divided in two spatially separate parts. The frontend electronics is located in a trailer close to the experiment. It is connected to the online workstation cluster via 2 SCSI interfaces realized as a fibre optical link. The backbone of the frontend is based on Fastbus technology with CERN Host Interfaces (CHIs) as masters which are equipped with DSP-based Struck Fastbus Readout Engines (FREs) to improve their performance. The drift chamber signals are read out by LeCroy TDCs (Time to Digital Converters), while the vertex and magnet chambers use APC and PCOS4, respectively, based readout systems without timing or analog information. Each photomultiplier tube as well as the TRD channels is fed to TDCs and ADCs (Analog to Digital Converters). The collected event information is processed by the FREs and can be compressed by almost a factor of 2 before an event is built and sent to the distributing online workstation (Alpha 3000X) located in the counting room. During data taking the incoming events are written as EPIO (Experimental Physics Input Output Package, [CN93]) files (called runs) to a 56 GB disk array hosted by further workstations linked via FDDI. Between two HERA fills the raw data files are then transfered via the a FDDI connection to a taping robot located in the computing centre at the DESY main site. Additionally the data is locally written to tape for backup purposes. The maximal DAQ throughput is 1.5 MB/s corresponding to an event rate of 150 Bq. In 1997 an upgrade of the distributing workstation to an Alpha 5/266 doubled this bandwidth. In 1995 3.8k runs of a total raw data amount of 1.5 TeraBytes was taken while in 1996 8k runs corresponding to 3.4 TeraBytes were written.

Dead Time

Relevant to analysis is the DAQ dead time fraction, i.e. the number of events that were triggered but were not read out because the DAQ was busy with the processing of an earlier event. Actually the dead time fraction δ_i is defined for each trigger i individually by

$$\delta_i = 1 - \frac{T^i_{acc}}{T^i_{gen}}, \tag{4.7}$$

where T^i_{acc} and T^i_{gen} is the number of accepted respectively generated triggers of a certain type. Since the DAQ performance depends on the trigger rates, the trigger dead time fractions are calculated for short time periods of 10 seconds called bursts. In case all triggers are generated randomly in time, a distinction

of trigger types is not necessary, but in practice there are prescaled (quasi-periodic) and periodic triggers which might introduce interference effects.

4.4 The HERMES Software

The HERMES software splits up into two parts, the online system which is used to run the experiment and record the raw data, and the offline software which processes this data and transforms it into a form that allows physicists to do their analysis work in an easy-to-use framework. Of course this division is not strictly true, since some physical analysis is performed (semi-) online to detect detector problems early. On the other hand only the offline treatment of the data allows precision calibration and systematic studies which might also affect the online performance (e.g. pedestal data for sparsification). While the kernel of the online system is using an rather old-fashioned software design (which has been shown in other experiments to work with high reliability), parts of the online monitoring system and the whole offline system is using a novel modular and datastructure-driven layout. In the following this part of the HERMES software will be described in more detail with an emphasis on the reconstruction program since this is most relevant for the analysis.

4.4.1 Main Software Modules

The main feature of the HERMES offline software is its high modularity, i.e. it is divided in multiple packages, each with clearly defined functionality. A package might consist of a number of executables and a library and via library calls a certain functionality can be used by user programs or other packages. The following (incomplete) list describes the main HERMES packages:

ADAMO ("ALEPH **DAta MOdell**") : This is the central entity-relationship based database underlying all of the following modules [Che76, FP93]. Through highly organised data structure and description it allows safe and portable data handling. The logical structure of the data is formulated using the Data Definition Language (DDL) and is stored and passed along with the data. Using an ADAMO-processor, DDLs are translated into structure definitions for Fortran or C which then are used to access the data in programs. ADAMO supports the storage of data in various formats (Generic ADAMO File, GAF).

DAD ("**Distributed** ADAMO **database**") : Since ADAMO does not support distributed databases, a client-server extension was developed at HER-

MES [Wan95]. It allows the central maintenance and distribution of all relevant data and implements efficient interprocess communication mechanisms in ADAMO format which is a basic prerequisite for modular software design. It also allows the efficient storage of data using on-the-fly (de)compression.

PINK ("PINK **is not** KUIP") : Although ADAMO provides a command line driven interactive shell for data analysis, a much more powerful tool was created at HERMES by implementing an interface to ADAMO and DAD in the script language Tcl [Ous94]. Together with the Tk package PINK allows the easy creation of Graphical User Interfaces (GUIs) for visualisation purposes (see appendix C.1) The PINK-browser (realized in Tcl/Tk) is a flexible tool to analyse ADAMO data in all formats. A windowless version called FLOYD is useful for rapid prototyping of analysis jobs as well as for the implementation of small help programs [Ack95, Fun95].

HMC ("HERMES **Monte Carlo**") : This is the main HERMES Monte Carlo based on GEANT [Bru93]. It consists of various event generators and is able to do a very detailed simulation of all HERMES detectors [GMV97].

PEPSI (**"Polarised Electron-Proton Scattering Interactions"**) : is the important physics generator for polarised Monte Carlo studies at HERMES [PEPSI]. It is available as a stand-alone library and is included in HMC. PEPSI is an extension of LEPTO [IER96].

HDC ("HERMES **DeCoder**") : translates the raw data from EPIO format to the ADAMO format as it is used in further analysis. HDC is parametrised by various (time-dependent) mapping, geometry and calibration data coming from central DAD servers so that it is easy to process raw data from different data taking periods. In online mode HDC feeds online servers with data from the online EPIO stream for monitoring purposes.

HRC ("HERMES **ReConstruction**") : reads event data either from HMC or HDC and reconstructs tracks using a tree-search algorithm [Wan96]. It provides basic particle identification information for each track. The reconstruction algorithm will be discussed in more detail in Section 4.4.3.

ACE (**"Alignment, Calibration and Efficiency"**) : is a module that calculates calibration and efficiency data for the tracking detectors in various ways [Kol98].

HEP ("HERMES **Event Processor**") : is an interactive shell for data analysis, but can also be used as an analysis frame for user code, preferably in Fortran. It incorporates all ADAMO and DAD features together with PAW and provides handling of analysis cuts and other features.

HANNA : this is another event-driven analysis frame that does not come with an interactive shell like HEP. It is used for fast processing of data using C code and is able to synchronise slow control data with the event stream. Although HANNA can be used without HBOOK, it provides a parametrisable cut package with histograming and statistics functionality [Fun96].

HLFLIB("HERMES **Library For analysis**") : is a collection of various functions that are useful for data analysis.

4.4.2 Data Production Scheme

Figure 4.8 shows the basic layout of the HERMES data production scheme. The raw EPIO event files are decoded and reconstructed and then stored as Data Summary Tapes (DSTs) on the central HERMES disk array. This first part of the production is the most resource intensive step and takes several weeks per year of raw data. It is performed on a LINUX cluster running on ten Dual-Pentium PCs [WF97]. In parallel to the DST production, the slowcontrol production (see Appendix C.2) reads slowcontrol data from the decoded runs as well as from record files written during data taking. The results of this production are enhanced slowcontrol data files which contain all relevant data in time-ordered form. The slowcontrol production is much faster than the DST production and needs a few days to process the data of one year. It usually runs in the background on the HERMES SGI cluster. The DSTs together with the enhanced slowcontrol data files are the input to all analysis. There exist two analysis frames which are capable of reading the two inputs in parallel and synchronise them. However, it turns out that at this level still too much data is contained in the files, which is necessary for expert studies but is not useful for physics analyses and only has the effect of slowing down the analysis programs. Hence a new data format, the μDST has been invented to speed up physical studies. The μDSTs contain both slowcontrol and event data in a compact format[4] and are the final output of the HERMES production scheme.

[4]Though this is not the end of sparsification. As mentioned earlier the low trigger threshold in 1996 lead to a high contamination of events where only hadronic tracks could be reconstructed. Hence there exist filtered μDSTs called nDSTs to get rid of these tracks. The format of the nDSTs is the same as for the μDSTs.

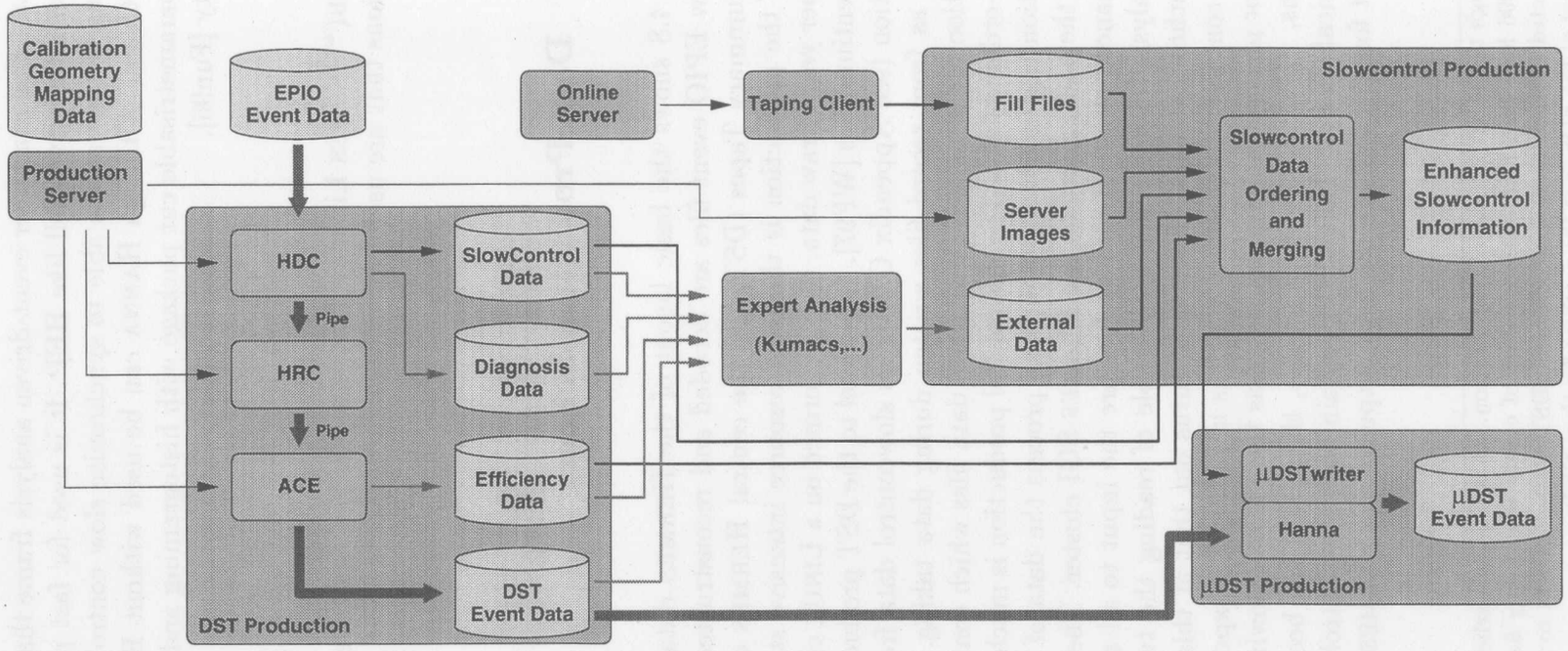

Figure 4.8: Layout of the Offline Software. *The big boxes group programs and data that are relevant for the DST, slowcontrol and µDST productions. Although these productions are hierarchical in the sense that they need data from the previous levels, they are technically independent and run separately. Small boxes indicate programs processing the data, cylinders show data files stored on disks and/or tape. The thick arrows shows the flow of event data, thin lines indicate the exchange of slowcontrol and calibration data.*

4.4.3 Event Reconstruction

The main part of the data handling that is also important to the physical analyses is the reconstruction of particle tracks from the information recorded by the tracking detectors. This is done separately for the forward and the backward region, yielding partial tracks. The identification of forward and backward partial tracks belonging to one physical track in the magnet region is called bridging and results in a set of full tracks per event. A detailed description of the HERMES reconstruction algorithms can be found in [Wan96].

Tree-Search

Before HRC constructs spatial partial tracks, it uses the detector hits in each of the three wire directions (x, u and v) to reconstruct track projections. The algorithm that is used here matches the detector information with patterns from a database which represent all possible tracks. This is done by a recursive tree-search algorithm which doubles the resolution per recursion step by considering only matching sub-patterns and converges very fast (see Figure 4.9). Since the tracking detectors are not perfectly efficient, the reconstruction algorithm is able to tolerate a certain number of missing hits in a track pattern. Furthermore the organisation of the pattern database makes use of the fact that only straight tracks have to be stored since the magnetic fields in the forward and backward regions are negligible. It also uses symmetry and scaling properties of the patterns to compress the database, and this is what only makes the application of the pattern matching algorithm at HERMES possible.

After a track projection was identified by the tree-search stage, the track parameters (slope, offset and the corresponding uncertainties) are calculated from the detector hits by a χ^2-fit where the individual detector resolutions are considered in the form of weights. The projections are combined to 3-dimensional partial tracks by combining the u and v projections and comparing the result to tracks found in the x projection.

As can be seen from Table 4.2 for the back region 2×4 planes per projection are available for reconstruction, while the front region is equiped with 2+4 planes per projection only. Unfortunately in 1995 the efficiency of the vertex chambers was too low, so only the front chambers could be used to define front tracks. Since the longitudinal extension of the FCs does not allow the partial tracks to be fit with the high accuracy needed to reach the anticipated kinematical resolution, a special bridging method was used to enhance the forward tracking by using information from the back tracks.

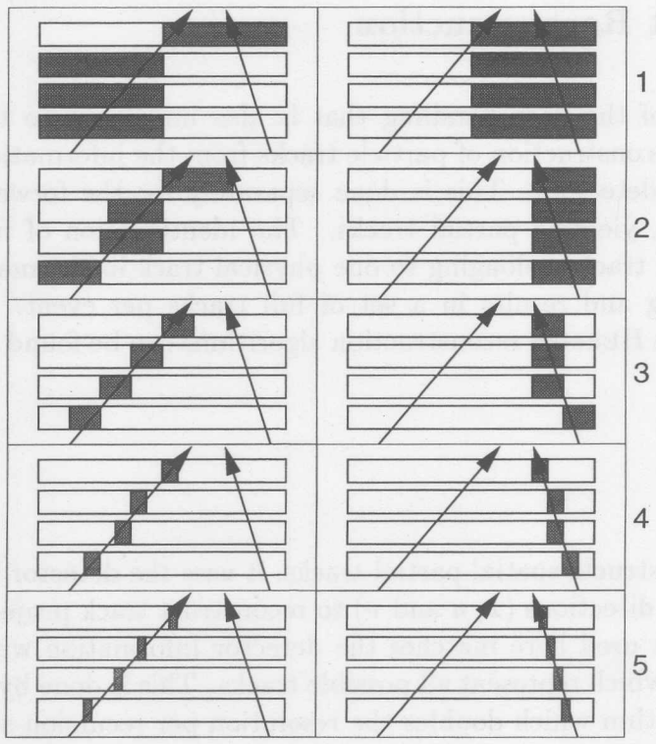

Figure 4.9: Pattern Matching and Tree-Search. *Here the algorithm is demonstrated for two tracks. First one coarse pattern with high road width which matches the detector information is selected. Then the road width is recursively bisected by matching daughter patterns with higher resolution (from top to bottom). If at a certain recursion step no daughter pattern is found the potential track is skipped.*

For the backward partial tracks the information of the corresponding particle identification detectors is linked to the track to allow the determination of the track type.

Bridging

The partial tracks found in the forward and backward region are combined to full tracks by comparing their projected track position in the middle of the spectrometer magnet, which is very similar for the forward and backward track. Alternatively a Kalman filter algorithm can be employed to identify forward and backward tracks by using the magnet chamber information.

In 1995, the forward tracks reconstructed from the FCs alone show a high uncertainty. To remedy this the matching point of a backtrack was included in a refit of the forward track which then improves the precision considerably.

Once a combination of two partial tracks is found, the parameters of the forward track (position and angles at the magnet entrance) is used to consult a lookup table which contains the position and direction after the magnet for discrete momentum values. Using the known bending angle a precise determination of the track momentum is possible by interpolation. The lookup table was generated by tracking particles through a Monte Carlo model of the setup, which was parametrised by a measured field map of the HERMES spectrometer magnet.

For low-momentum tracks which are deflected so much by the dipole field that they do not reach the backward region it is possible to do a coarse momentum measurement by applying a shooting method to fit the magnet chamber hits.

Resolution

The angle and momentum resolution of the reconstructed tracks can be derived by comparing the true values from Monte Carlo generated events with the reconstructed values from HRC. For this analysis a precise knowledge of the resolutions of the individual tracking detectors is necessary, which can be extracted from data by exploiting the fact that a track can be reconstructed neglecting a certain detector plane. The width of the distribution of the distance of the measured hit position in the plane from the reconstructed track is then a measure for the resolution of the plane[5].

However, the Monte Carlo and the reconstruction algorithm will make use of the same magnetic field map for the spectrometer magnet and need to be crosschecked by physical calibration processes which deliver tracks with defined momentum correlation. One such process is the decay of neutral kaons K^0_S into two charged pions (branching ratio 68.6%). By calculating the invariant mass of the two-pion system

$$\begin{aligned} m_{2\pi} &= (\boldsymbol{p}_{\pi^+} + \boldsymbol{p}_{\pi^-})^2 \\ &= 2m_\pi^2 + \sqrt{(m_\pi^2 + p_{\pi^+}^2)(m_\pi^2 + p_{\pi^-}^2)} + 2p_{\pi^+}p_{\pi^-}\cos\phi, \end{aligned} \tag{4.8}$$

where $p_{\pi^\pm}$ are the moments of the two oppositely charged pions and ϕ is their opening angle in the laboratory reference system, a very clean K^0_S-sample can be retrieved by using the long decay length of the K^0_S (Figure 4.10). The measured K^0_S mass of 496.39±0.08 MeV deviates less than 0.25% from the

[5]In fact the centroid of this distribution should be zero and can be used for alignment purposes.

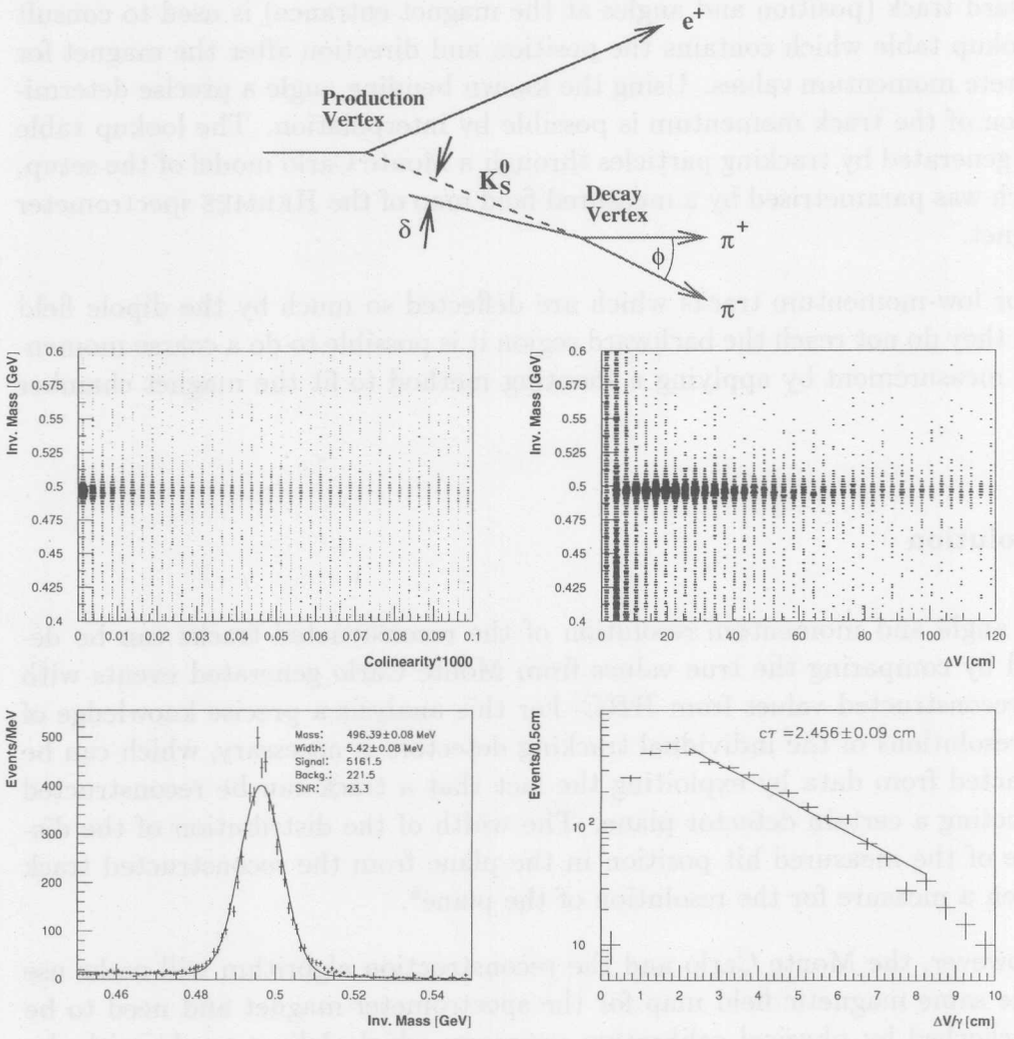

Figure 4.10: Reconstruction of Neutral Kaons. **Top:** *A short lived Kaon originating from the DIS event at the primary vertex decays after some time into two charged pions. The two pion tracks and the scattered lepton are reconstructed.* **Middle-left:** *The invariant mass (4.8) of the two-pion system is plotted against the collinearity* $(1 - \cos^{-1}\delta)$ *of the vertex distance and the momentum of the hypothetical* K^0_S. **Middle-right:** *The invariant mass is plotted against the distance of production and decay vertex.* **Bottom-left:** *The distribution of the invariant mass is shown after cuts on collinearity and vertex distance.* **Bottom-right:** *The lifetime of a* K^0_S*-sample is measured by fitting an exponential to the (relativistically corrected) vertex separation. The deviation of the measured value from the world value of 2.675±0.006 cm is also seen in Monte Carlo data and is understood as an acceptance effect and cut artefacts.*

world value of 497.57±0.03 MeV [PDG94], and together with the width of the mass distribution it is a measure for the over-all calibration of the spectrometer. A detailed analysis yields an energy resolution of better than 1% and an angular resolution of 1 mrad for pion tracks from K^0_S-decays with an average momentum of 4 GeV/c for the 1995 data reconstructed without vertex chambers [Wan96]. The spectrometer resolution using all tracking devices is expected to be better.

Efficiency

The total track reconstruction efficiency $\mathcal{E}_{tot}$ can be expressed as

$$\mathcal{E}_{tot} = \mathcal{E}_{front} \cdot \mathcal{E}_{back} \cdot \mathcal{E}_{bridge}, \tag{4.9}$$

where $\mathcal{E}_{front/back}$ are the reconstruction efficiencies for the forward and backward partial tracks and $\mathcal{E}_{bridge}$ is the bridging efficiency.

For the tree-search algorithm the partial track efficiencies can be derived analytically from the detector plane efficiencies which are extracted by ACE from data for intervals of 10 seconds during data production [Kol98]. The bridging efficiency can be derived from Monte Carlo simulations. For the correction applied in 1995 to the forward tracks, the efficiency can also be extracted from data by comparing the number of reconstructed tracks with and without modified forward tracks.

The version of ACE that was used to process the 1995 helium data did not distinguish the detector efficiencies for different particle types, which can be different [Neu97]. Hence the tracking efficiency is not used for rate corrections but only to identify drops in the detector performance caused by things like voltage trips. Since during normal operation all factors of (4.9) are high and stable, rather tight cuts can be used and the systematic uncertainty introduced on the asymmetries is neglected.

4.5 Unpolarised Measurements

Although it is not topic of this work, it should be pointed out, that HERMES is also able to perform a variety of measurements using unpolarised gas targets of high density. Among other things that allows the extraction of structure function ratios, the determination of hadro-production cross sections and the study of nuclear effects like nuclear transparency. First results of these analyses have been presented and will be published soon.

Chapter 5

Extraction of Asymmetries

The number of events of a certain type in the two spin states can be expressed as

$$\begin{aligned} N^{+} &= \mathcal{E}\sigma \int_{+} \mathcal{L}(t)\left(1 + A\overline{D}^{+} p_T(t) p_B(t)\right) dt, \\ N^{-} &= \mathcal{E}\sigma \int_{-} \mathcal{L}(t)\left(1 - A\overline{D}^{-} p_T(t) p_B(t)\right) dt, \end{aligned} \tag{5.1}$$

where A is the spin asymmetry of the process, σ is the integral of the unpolarised differential cross-section over the kinematical region of interest, $\mathcal{E}$ is the acceptance and efficiency for the same region (assumed to be spin-independent), $\mathcal{L}(t)$ denotes the time-dependent luminosity, $p_B(t)$ and $p_T(t)$ denote the polarisations of the beam and target and $\overline{D}$ gives the event-by-event photon depolarisation factor as defined in (2.24) averaged over all events in this spin state. Note that $\overline{D}$ varies for different particle types; even if D is purely a function of inclusive kinematics, these distributions might differ for different semi-inclusive processes. To measure the asymmetry, one resolves the two equations (5.1) for A and obtains:

$$A = \frac{N^{+} \int_{-} \mathcal{L}(t)dt - N^{-} \int_{+} \mathcal{L}(t)dt}{N^{+}\overline{D}^{-} \int_{-} \mathcal{L}(t) p_T(t) p_B(t) dt + N^{-}\overline{D}^{+} \int_{+} \mathcal{L}(t) p_T(t) p_B(t) dt}. \tag{5.2}$$

At this point, some short remarks about the error calculation are appropriate. First note that the observed hadron numbers N_h are not Poisson distributed and their errors are not exactly given by $\sqrt{N_h}$. The reason for this lies in the fact that the probability to observe a hadron in an event with an identified positron is not small enough to use the Poisson approximation and

that more than one hadron can be seen per event. Furthermore, the particle numbers observed on the same data sample (e.g. one spin state) are not independent, i.e., to describe the errors one does not only need the variances on the single particle numbers but also their covariances. Appendix A.1 contains the derivation of the true error on the hadron numbers and the related correlation coefficients. In Appendix A.2 the same quantities are derived for the asymmetries.

Technically the analysis is performed using the HANNA-frame (see Appendix C.3) with μDSTs. Events without identified leptons were stripped from the hydrogen μDSTs to save space and analysis time - reduction factors of 20% could be achieved here[1]. The processing of the 95 ^{3}He data takes approximately 1.5 hours on an 200 MHz PentiumPro PC running LINUX, the hydrogen data taken in 1996 can be processed in 45 minutes. The code for applying cuts, extracting the particle numbers and correlations, calculating the asymmetries and finally extracting the quark spin distributions is the same for data analysis as well as for all Monte Carlo applications (i.e., the generation of the purity matrix or test samples for systematic studies and consistency checks).

5.1 Data Quality

The HERMES spectrometer is a complex apparatus consisting of a number of independent subsystems which are all required to be operational to perform a valid analysis. Whenever one subdetector was not working properly the corresponding data can not be used for analysis. There are multiple sources of this data quality information: some events (like HV trips etc.) are recorded automatically during data acquisition while other periods with known problems are excluded by hand. Most of the quality criteria are derived offline from consistency checks which are calculated for short time intervals[2]. Generally these criteria should not be correlated to the physical process under study. For example it is not allowed to apply tight cuts on particle yields if an asymmetry is calculated, since the yield and hence the cut result would be spin-dependent.

In this work the results of the quality analysis as performed for the inclusive analyses were used, but generally more stringent cuts were applied. Both detector halves and all PID detectors were required to be operational, which is not necessary for the inclusive case. In the following the main quality criteria are described; Table 5.1 shows a list of the most important of them. More

[1] See footnote 4 on page 49.

[2] At HERMES usually the 10 second intervals called bursts are used to perform data quality analyses.

Criterion	1995	1996
Beam Current	$I_e \in [8, 32]$ mA	$I_e \in [8, 50]$ mA
Beam Polarisation	$p_B \in [.4, .7]$	$p_B \in [.3, .8]$
Target Polarisation	$p_T \in [.3, .6]$	$p_T \in [.8, .99]$
Target Density	$n \in [.85 \cdot 10^{15}, 1.4 \cdot 10^{15}] \frac{\text{Nucl}}{\text{cm}^2}$	—
Plane Eff. FC	$\min(\mathcal{E}_{FC}) \in [.8, 1]$	—
Plane Eff. BC	$\min(\mathcal{E}_{FC}) \in [.94, 1]$	—
Lumi Rate	$R_{Lumi} \in [40, 210]$ Bq	$R^{fit}_{Lumi} \in [5, 60]$ Bq
Trigger Lifetime	$\mathcal{E}_{DAQ} > .5$	$\mathcal{E}_{DAQ} > .8$
Burst Length	$T_{Burst} \in [9, 11]$ sec	$T_{Burst} \in [0, 11]$ sec
Good Bursts/Run	$N^{good}_{Burst}/N^{tot}_{Burst} > .4$	—
Bad Periods/Run	$N^{bad}_{Period}/N^{tot}_{Burst} < .1$	—
Good Bursts/Fill	$N_{Burst} > 100$	—

Table 5.1: List of Quality Criteria. *See Section 5.1.*

detailed documentation of the inclusive data quality handling can be found in [HER97a] and [Has97].

5.1.1 Beam Quality

For the analysis of polarised observables the most important beam-related quantities are the beam polarisation and current. The time development of polarisation was fitted for each fill to be less sensitive to statistical fluctuations of the polarimeter measurements. A lower polarisation limit was required to get rid of data with low weights. Also a minimum beam current was required since for low current data not enough statistics per burst are collected to perform reliable quality checks.

Other beam parameters like beam position and slope at the interaction point or proton background rates are available for data quality checks, but cuts on these quantities do not influence the extracted asymmetries since they are covered by other criteria. High background periods are excluded by the cut on the trigger dead time and the coincidence rate of the luminosity monitor.

5.1.2 Target Quality

Unlike the beam polarisation which can not be inverted during a HERA fill, the target polarisation is flipped on a short time scale to reduce systematic effects. The time periods in which the target spin direction was changing from

one spin state to the other were excluded from the analysis. Similarly to the beam polarisation, lower and upper limits for the measured target polarisations were set to exclude data of low weight or unphysically high polarisations. For the hydrogen data the target polarisation was smoothed as in the case of the beam polarisation to decrease the influence of outlying measurements. For the helium data an additional cut was applied on the target density, which is derived from the pressure in the pumping cell.

5.1.3 Tracking Quality

The tracking quality is primarily given by the performance of the tracking detectors but is also affected by changes of the alignment during service accesses to the experimental area. After applying appropriate corrections, the reconstruction efficiency was stable for long time periods. Changes caused by the optimisation of operation parameters of the chambers do not affect the asymmetry measurement since they are on a time scale which is much longer than the spin flipping.

For the 1995 data the minimal plane efficiency of each detector region (top, bottom, front, back) was used to detect short drops of the high voltage ("trips") which happen if the current drawn by a chamber exceeds a certain limit due to a spike in the background. The bursts before and after a period of bursts with decreased plane efficiency might also be affected by the trip and are therefore excluded as well. In 1996 the trip detection was done by evaluating the slow control messages of the high voltage system. Alternatively the number of hits per burst for each plane can be counted. If the high voltage drops, a plane shows significantly fewer hits than its neighbours and the corresponding bursts plus the previous and following ones are marked bad.

5.1.4 PID Quality

The quality of the components of the particle identification system is checked by a bootstrap-method. To check the performance of one detector hard cuts with low contamination on the other three PID detectors are used to identify the particle type. The detector distributions for the hypotheses are then compared to reference distributions and periods with problems can be identified. While for inclusive studies it is possible to give up the information of either the TRD or the Čerenkov counter (PID downshifting scheme) without raising the contamination of the positron sample significantly, this is only done for periods with a bad TRD in 1995 to ensure as pure as possible hadron samples

for this semi-inclusive analysis.

5.1.5 Miscellaneous Quality Criteria

There are a couple of additional cuts applied to the data to avoid known systematical effects on the asymmetry extraction. For instance, the first three and the last burst of each run are not used, since at the beginning of each run initialisation processes take place which might have effects on the tracking efficiency and time synchronisation. The last burst of a run might not be completely contained in the run but partially written to the next one. A variety of data quality checks are performed at earlier stages of the data production, primarily in the decoder and the μDST-writer, which have access to redundant representations of the data and consistency criteria which can be used to isolate periods with unreliable detector performance. Finally in 1995, runs which have a high fraction of bad bursts are not used in the analysis, as well as HERA fills which do not contain enough good bursts to calculate significant asymmetries. In 1996 these cuts have not been necessary since the machine and experimental performance were much more stable.

5.2 Track and Event Selection

All geometrical and kinematical cuts used for track and event selection are listed in Table 5.2. The cuts applied to tracks are mostly fiducial constraints to avoid systematic effects at the edges of the spectrometer acceptance. Some of these constraints actually don't affect the data but are useful for Monte Carlo productions.

Each track passing the geometrical cuts is linked to one or more particle classes according to Table 5.3. For 1995 the *pid* value is calculated using a downshifting scheme for periods of bad TRD performance:

$$pid = \begin{cases} pid_3 + 0.31 \cdot P_{TRD} - 0.48 & \text{if TRD is operational,} \\ pid_3 & \text{if TRD is bad,} \end{cases} \tag{5.3}$$

where the first case represents the valley cut (see Figure 4.7). The quantity pid_3 was defined in (4.5) and P_{TRD} is the TRD response.

The track with the highest reconstructed momentum identified as a positron is then used to define the DIS kinematics. Events without reconstructed positrons are rejected. Cuts on the inclusive kinematics are done to extract a

Tracks		
Quantity	Range	Unit
$\lvert\theta_y\rvert$	$[40, 140]$	mrad
Horizontal Position at Calorimeter	$[-175, 175]$	cm
Vertical Position at Calorimeter	$[30, 100]$	cm
Longitudinal Vertex Position	$[-18, +18]$	cm
Lateral Vertex Position	$[0, 0.75]$	cm
Momentum	≥ 0.5	GeV/c
DIS kinematics		
Quantity	Range	Unit
Q^2	≥ 1	$(\text{GeV/c})^2$
W^2	≥ 10	GeV^2
y	$[0, 0.85]$	
E Calorimeter	≥ 3.5	GeV
Hadron kinematics		
Quantity	Range	Unit
z	$[0.2, 1]$	
x_F (π only)	$[0.1, 1]$	

Table 5.2: Cuts on Event Level. *These constraints are grouped into three subsets: Cuts that are applied to each track to eliminate inhomogeneities at the edges of the spectrometer acceptance, kinematical cuts that are using the inclusive kinematics of the leading positron to select DIS events and hadronic cuts that are used to suppress hadrons originating from the target fragmentation region.*

	PID		Momentum	
Class	1995	1996	1995	1996
Lepton	> 2	> 0	—	—
Hadron	< -1	< -2	—	—
$\pi^{\pm}$	< -1	< -2	6–21 GeV/c	4–13.3 GeV/c

Table 5.3: Particle Classes. *Note that the pion samples for the two years are not comparable due to the use of different Čerenkov radiators.*

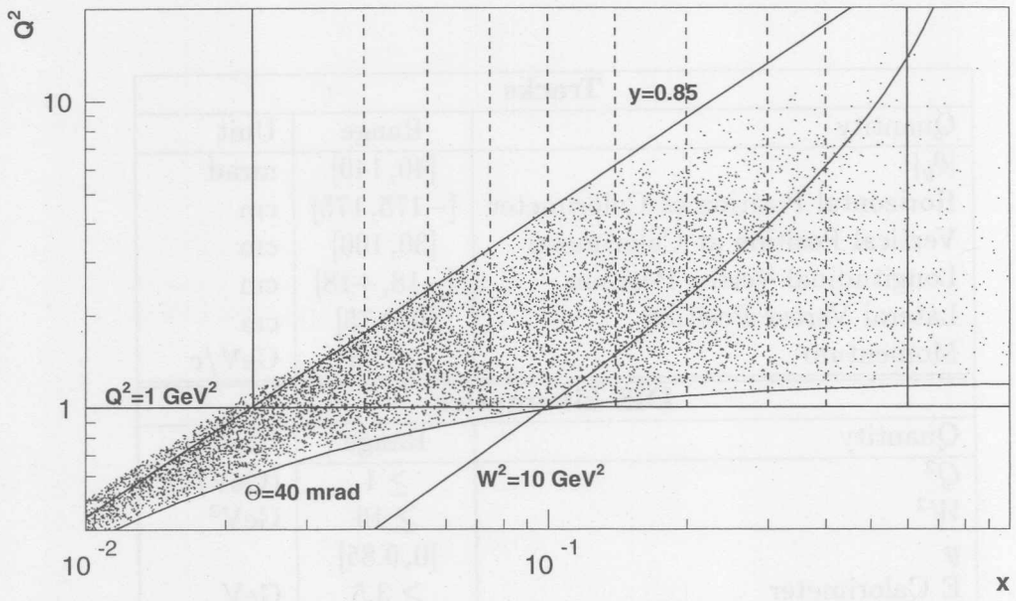

Figure 5.1: Event Distribution in the Kinematical Plane. *The distribution of reconstructed event kinematics is plotted in the (x, Q^2)-plane together with the boundaries introduced by kinematical cuts. The vertical dashed lines visualise the x-binning used in this analysis (see also Table B.1).*

pure sample of DIS events and to make sure that the influence of radiative corrections is small (see Section 5.3.2). The distribution of reconstructed events as well as the effects of the cuts are shown in Figure 5.1.

The cuts on hadron kinematics select hadrons that predominantly originate from the current fragmentation region, since those are assumed to be more sensitive to the quark structure of the nucleon than hadrons from the target region. Since for the calculation of Feynman's scaling variable the particle mass has to be known, x_F is not well defined for the hadron sample.

5.3 Corrections

Asymmetry measurements are potentially insensitive to apparatus effects that vary on time scales which are large compared to the spin flip period. For instance, all acceptance corrections cancel as long as the geometrical and kinematical track distributions do not depend on the spin state, which is true to a high degree. In the following the main sources of expected distorting effects

on the measured asymmetries are discussed.

5.3.1 Kinematical Smearing

Kinematical smearing describes a systematic difference between measured and true kinematical quantities by effects of the apparatus. The main source of kinematical smearing is the interaction of scattered particles with components inside the spectrometer. In particular electrons and positrons lose parts of their energy due to multiple scattering, even in small amounts of material. A second source of systematic shifts of the measured quantities is introduced by calibration and alignment offsets of the tracking devices, as well as by the reconstruction algorithm itself.

To derive the true kinematical distribution from the measured one, the kinematical plane is segmented into bins (denoted in the following by the index i). One way to describe smearing effects is to introduce the migration matrix $\mathcal{M}_{ij}$ which gives the probability that an event which was measured in bin i actually belongs to bin j for all combinations of bins. The measured distribution M_i and the true one N_i are then connected by the relation

$$M_i = \sum_j \mathcal{M}_{ij} N_j. \tag{5.4}$$

Technically the migration matrix can be derived from Monte Carlo simulations and this system of equations can be inverted. The described unfolding method was used in [Ack96] to calculate corrections to unpolarised data on an (x, Q^2)-binned kinematical plane with an iterative algorithm based on Bayes' theorem [Ago95]. For the chosen binning the correction factors are found to be less than 3% for structure function ratios.

However the knowledge about the smearing of the unpolarised distributions does not allow a direct estimation of the effects on the asymmetries. On one hand most of the effects cancel by building the ratio of rates but on the other hand the asymmetries on the proton (Figure 5.4) show such a strong x-dependence that already a small amount of high-x events which are smeared to a lower x-region can lead to sizable corrections. In Figure 5.2 the result of a corresponding Monte Carlo study using HMC (see Section 4.4.1) on a proton target is shown [Gut98]. For the asymmetries on helium the smearing effects are expected to be much smaller since they show a much smaller x-dependence [Fer97]. Hence the helium asymmetries used in this work are not corrected for kinematical smearing effects.

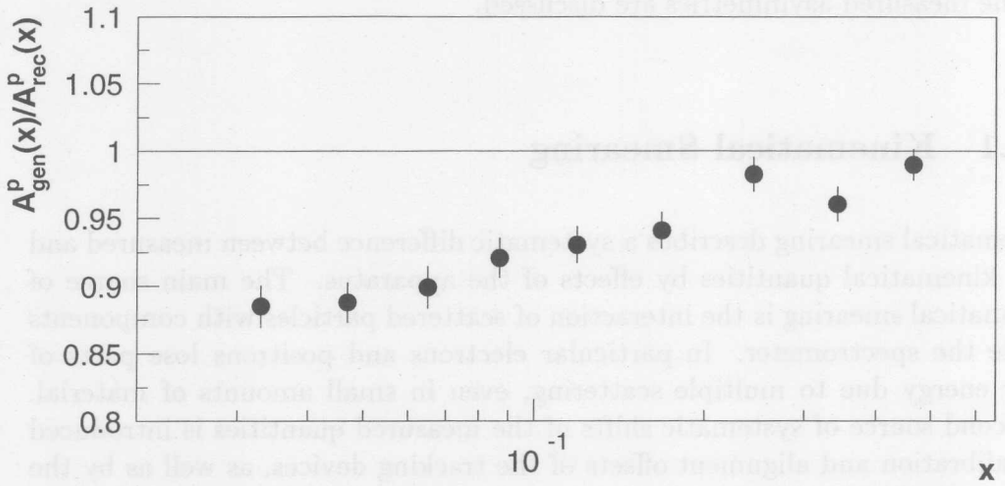

Figure 5.2: Corrections for Kinematical Smearing. *The ratio of the generated asymmetry over the reconstructed asymmetry is plotted. The measured asymmetries have to be multiplied by this ratio to obtain the true asymmetry.*

5.3.2 Radiative Corrections

In Chapter 2 the deep inelastic scattering was described in first order QED (Born level), i.e., only the interchanged virtual photon was considered. Of course the measured physical process implies also higher order corrections as shown in Figure 5.3 (left). The electro-weak correction caused by γ/Z_0 interference can be neglected at HERMES energies since $Q^2 \ll M_{Z_0}$. Technically the corrections from radiative processes can be described as with kinematical smearing, so we use the correction factor

$$\eta(x,y) = \frac{d^2\sigma_{exp}}{d^2\sigma_{Born}}, \tag{5.5}$$

denoting the ratio between measured cross section and the cross section of the lowest order process. The quantity $\eta(x,y)$ can be calculated by integrating over the high order processes under consideration of the experimental acceptance. In Figure 5.3 (right) the result as used to correct unpolarised structure functions [Ack96] is shown, calculated using the program TERAD [Brü93] which is based on the model of Ahkundov, Bardin and Shumeiko [ABS86].

For inclusive polarised radiative corrections a model from Akushevich and Shumeiko [AS94] can be used. Similar to the case of kinematical smearing, asymmetries are in general less affected by radiative corrections [AS94]. However a cut of $y < 0.85$ was applied to avoid the region with a high unpolarised correction. A formalism and implementation for applying radiative corrections

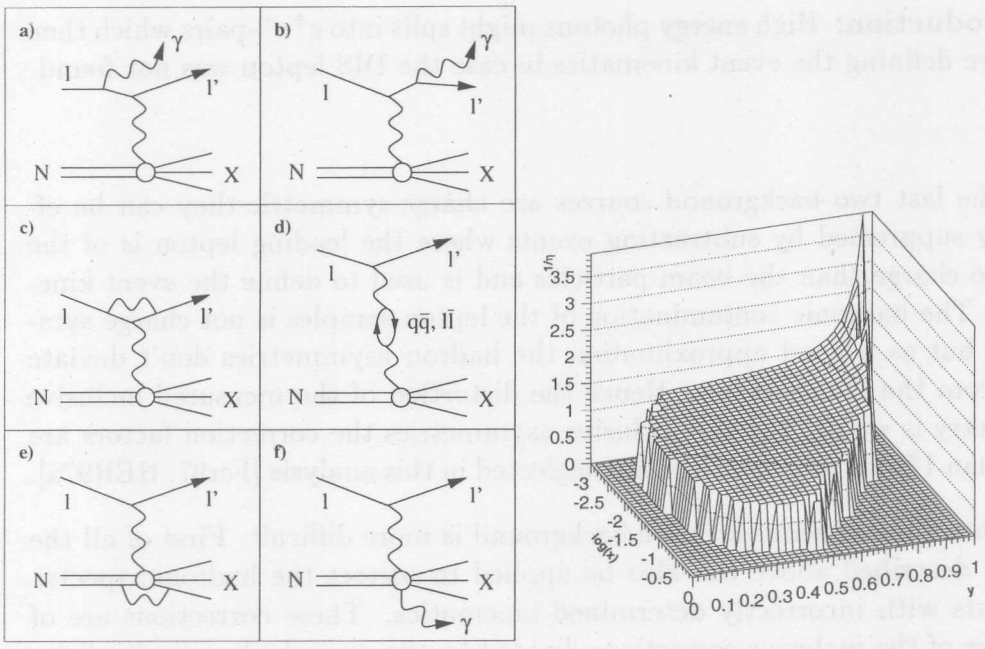

Figure 5.3: Radiative Corrections. **Left:** *The most important corrections at* HERMES *energies are shown: a) Bremsstrahlung in initial state, b) Bremsstrahlung in final state, c) vertex correction, d) vacuum polarisation, e) hadronic vertex correction, f) hadronic Bremsstrahlung.* **Right:** *The radiative correction factor for unpolarised cross sections as calculated with* TERAD.

to semi-inclusive processes was under development while this analysis was performed. Preliminary results give absolute corrections for the asymmetries in the order of a few percent of the statistical errors [Ihs98], hence these correction factors have not been used in this work.

5.3.3 Background

There are different kinds of background sources to the measurements of inclusive asymmetries:

Misidentified hadrons: The lepton sample is contaminated to a small degree with hadrons which might define a wrong event kinematic if they are reconstructed with high momentum or the DIS lepton was not found.

Photoproduction: In this process the DIS lepton might be scattered under a small angle and escape in the acceptance gap of the spectrometer. The produced vector meson might decay into leptons (or photons, see next point) which are then identified as DIS lepton.

Pairproduction: High energy photons might split into e^+e^--pairs which then are defining the event kinematics in case the DIS lepton was not found.

Since the last two background sources are charge-symmetric they can be efficiently suppressed by subtracting events where the leading lepton is of the opposite charge than the beam particles and is used to define the event kinematics. The hadronic contamination of the lepton samples is not charge symmetric, but as a good approximation the hadron asymmetries don't deviate much from the inclusive one. Hence the distortion of the measured inclusive asymmetry is small. For the inclusive asymmetries the correction factors are lower than 1% for all x-bins and are neglected in this analysis [Fer97, HER97a].

The handling of semi-inclusive background is more difficult. First of all the concept described above can also be applied to correct the hadronic spectra for events with incorrectly determined kinematics. These corrections are of the order of the inclusive corrections divided by the mean hadron multiplicity and hence also very small. In addition hadronic processes like photoproduction produce additional hadronic background which is not correlated to the physical process under study. In the purity method these processes are included in the Monte Carlo generation and are hence potentially covered by the analysis, however the models for photo production at medium energies are not yet well-tuned to describe the measured data. The hadronic background from e.g. ρ_0-decays can be extracted from the number of reconstructed rhos in the data if the reconstruction efficiency is known. Studies show negligible effects for the cuts chosen.

5.3.4 Trigger Lifetime

As mentioned in Section 4.3.5 the DAQ will not be able to read out all events at high trigger rates and the individual triggers will have a certain dead time fraction δ_i. To correct for this effect, the luminosity $\mathcal{L}$ integrated in (5.1) and (5.2) is computed as

$$\mathcal{L}(t) = (1 - \delta_i(t))\, R_{Lumi}(t), \tag{5.6}$$

where $R_{Lumi}(t)$ is the coincidence rate of the luminosity monitor and $\delta_i(t)$ is the dead time fraction of the trigger used for the analysis as defined in (4.7).

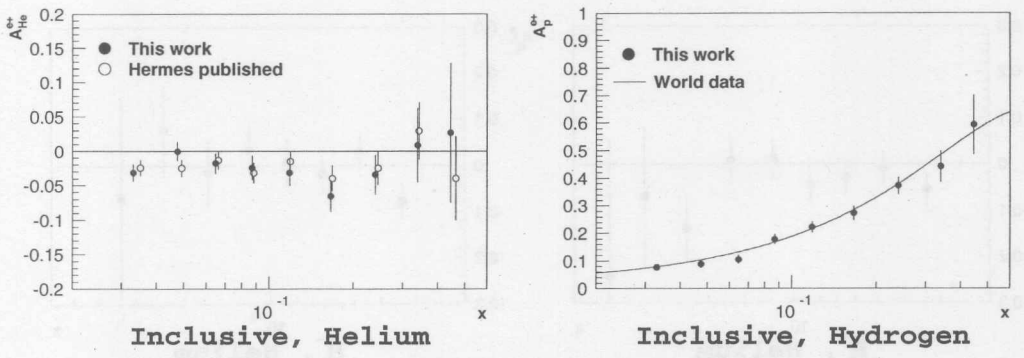

Figure 5.4: Inclusive Asymmetries. *The left plot shows the inclusive asymmetry as extracted from the ^{3}He data taken in 1995, while to the right the results on the hydrogen data from 1996 are shown. Only statistical errors are shown. The hydrogen data points of this analysis were used to fit a curve of the same shape but with different norm (parameter P_1) than a fit to world data. See Table B.4 for numerical values of the asymmetries.*

5.4 Extracted Asymmetries

Figure 5.4 shows the extracted inclusive asymmetries from the 1995 ^{3}He and the 1996 hydrogen data as defined by (5.2). The helium asymmetries are compatible within the statistical errors with the values used to measure $g_1^n(x)$ [HER97b]. Small differences are caused by the increased cut of W^2>10 GeV^2 as compared to 4 GeV^2 in the $g_1^n(x)$ analysis. To cross-check results of the hydrogen analysis, the data was compared to a fit to the published world data[3] of A_p^1. The good agreement shows that the preliminary systematic error of the target polarisation stated in Table 4.1 is overestimated.

Figure 5.5 shows the extracted semi-inclusive asymmetries for both targets. The hadron asymmetries are compared to preliminary SMC results from [SMC98]. It should be noted, that the pion asymmetries only cover pions with a certain momentum range, which is different for the two targets because the Čerenkov radiator was changed (compare Tables 4.3 and 5.3). The higher pion threshold in 1995 is the reason for much bigger uncertainties on the pion data as compared to the hadron data of the same year.

[3]The parametrisation of the world data fit to g_1/F_1 is of the form $g_1/F_1(x) = a_1 + a_2 x + a_3 x^2$ with $a_1 = 0.0212, a_2 = 1.804, a_3 = -1.294$ [Stö97]. For the comparison to the extracted asymmetries this ratio is multiplied by $(1+\gamma^2)$ (compare equation (2.28)).

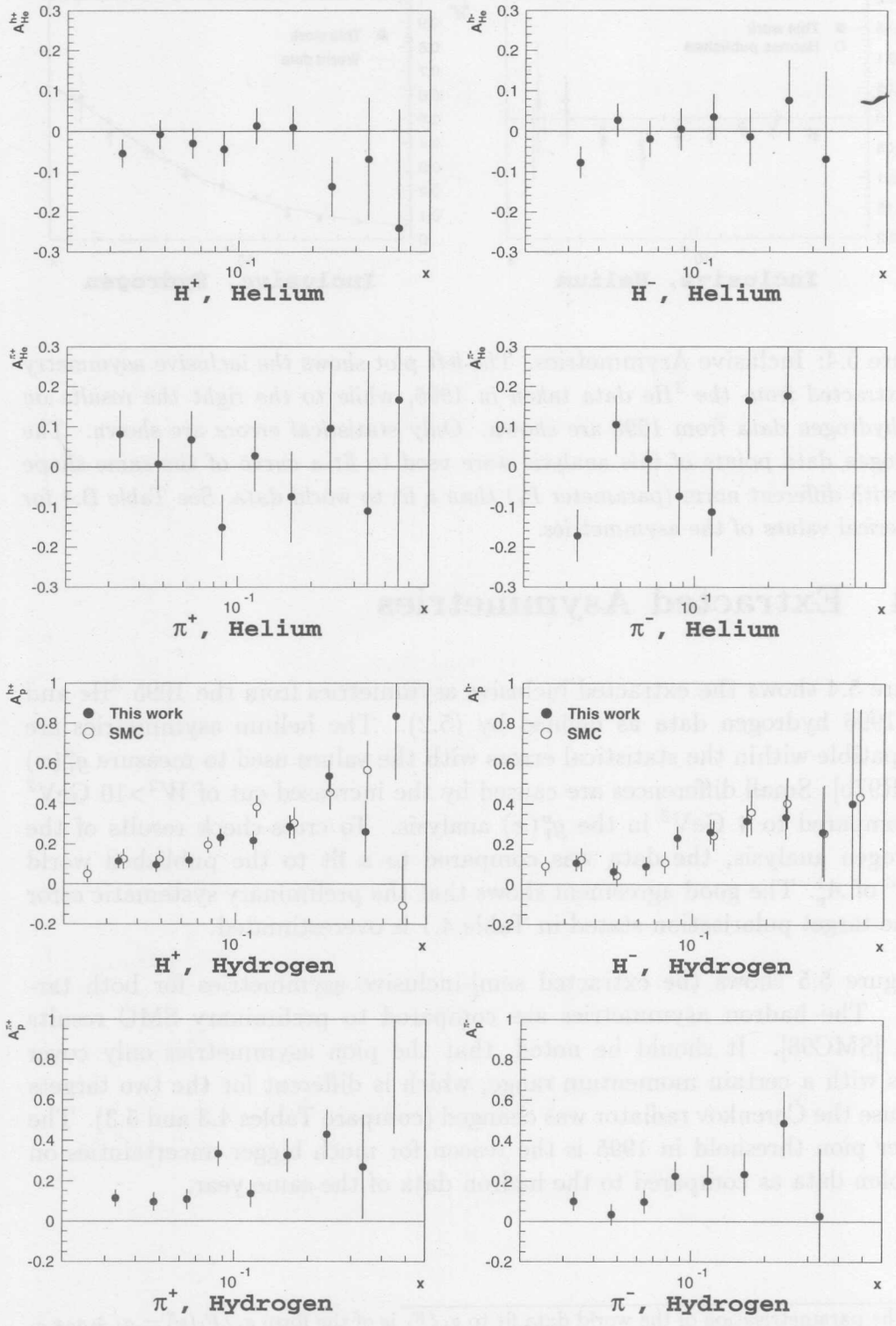

Figure 5.5: Semi-inclusive Asymmetries. *(Statistical errors only).*

Chapter 6

Using Purities to extract polarised Parton Density Functions

In the previous chapter the extraction of the inclusive and semi-inclusive particle asymmetries was described and performed for HERMES data taken on two different targets. Now we will take up again the purity formalism from Section 3.6 to extract polarised parton density functions from these asymmetries.

In the first part of the following chapter the Monte Carlo generation of purities will be discussed. Then different alternative assumptions about the polarisations of the sea quarks will be introduced as a method to reduce the degrees of freedom in equation (3.14), which is a technical necessity to be able to invert this system of equations. After this, the purity formalism will be extended in a way that allows the inclusion of the asymmetries measured on helium in a combined fit on both data sets. At the end of this chapter we will than have all prerequisites to use the the helium and proton data of the 1995 and 96 running periods to obtain the polarised parton density functions of the nucleon as the main result of this work.

6.1 Generation of Purities

From definition (3.11) follows that we need two different inputs for generating purities. First we need some information about the structure of the nucleon in form of the unpolarised quark densities $q(x)$ and second we need a model for the hadronisation in form of the fragmentation functions $D_h^q(z)$. The basic

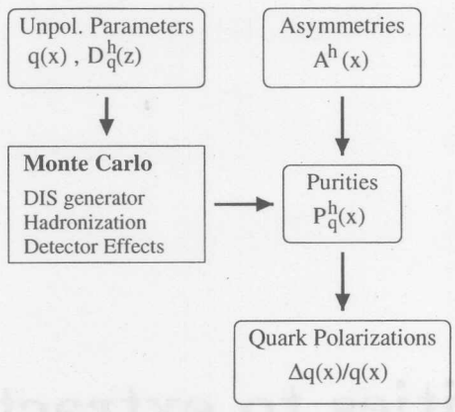

Figure 6.1: The Purity Extraction Method. *An unpolarised Monte Carlo generator parametrised by unpolarised data ($q(x), D_q^h(z)$) generates the purity matrix $P_q^h(x)$ which then is used to convert the measured hadron asymmetries into quark polarisations.*

dataflow of the method is shown in Figure 6.1; the calculation of the purities is performed by a Monte Carlo method.

The Monte Carlo consists out of three major parts, where the first two are responsible for the generation of the actual physical event [Sjö94, IER96, PEPSI] and the third one does include detector effects. First, in the DIS generator a point in the DIS kinematical plane is selected (which defines the inclusive event information) and the unpolarised quark densities are used to decide on which quark the scattering is performed[1]. In the second step the kinematics of the struck quark as well as the structure of the target remnant is passed to the hadronisation module which then generates the semi-inclusive part of the event information. At this point the physics part of the event simulation is done and the kinematics of all generated particles are known. Now the Monte Carlo has to simulate which particles are actually seen by the detector and would be reconstructed as tracks. There is a detailed model of the HERMES-detector available based on GEANT, which is able to simulate with a high accuracy all responses of the tracking and particle identification detectors as well as effects due to interactions with material [GMV97, Bru93]. However the CPU-consumption of this Monte Carlo is so high that a different approach was used for this analysis, which basically requires a good simulation of the geometrical and momentum acceptance of the spectrometer and is not so sensitive to background effects. To achieve this, the simple box model of the detector acceptance was augmented by the use of the HRC momentum lookup tables to simulate the exact momentum cut-offs and also to generate

[1] In general more complex processes like quark-gluon-fusion are also simulated, but not discussed here.

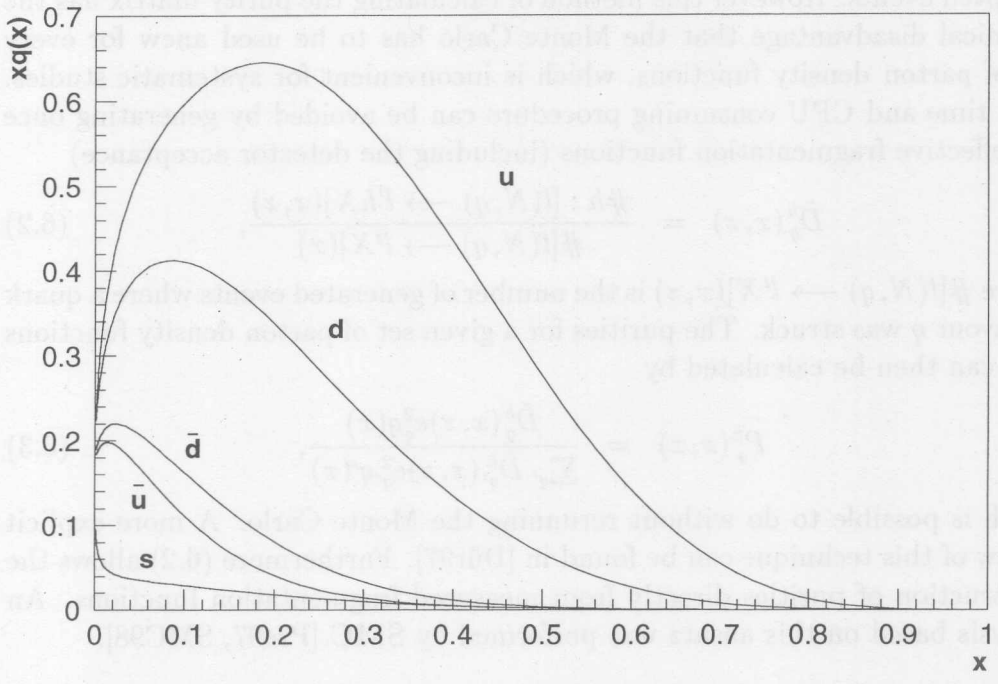

Figure 6.2: Parton Density Functions. *The parametrisations from [GRV95] were evaluated for the Q^2 measured at* HERMES *(Table B.1).*

the proper geometry of the backward tracks, so that the same fiducial cuts as on the reconstructed data could be applied.

To minimise systematic effects it is desirable to measure all unpolarised input in the same kinematic region and with the same apparatus as used for the measurement of the hadron asymmetries. This allows one to tune the quark densities as well as the hadronisation parameters in such a way that agreement between Monte Carlo and experimental data becomes optimal. Indeed this approach was used for the hadronisation stage [Gei98]. However the global fits to world data together with the well-understood evolution to our energy range yield an accuracy for the quark densities that could not be achieved with the HERMES unpolarised data (Figure 6.2).

Using the discussed inputs the purity matrix now can be generated. An entry in this matrix is given by

$$P_q^h(x,z) = \frac{\#h : [l(N,q) \longrightarrow l'hX](x,z)}{\#h : [lN \longrightarrow l'hX](x,z)}, \tag{6.1}$$

where $\#h : [l(N,q) \longrightarrow l'hX]$ denotes the number hadrons of type h in all accepted events where the lepton scattered off a quark of flavour q in the nucleon N while $\#h : [lN \longrightarrow l'hX](x,z)$ gives the number of hadron h in all

accepted events. However this method of calculating the purity matrix has the technical disadvantage that the Monte Carlo has to be used anew for every set of parton density functions, which is inconvenient for systematic studies. This time and CPU consuming procedure can be avoided by generating once the effective fragmentation functions (including the detector acceptance)

$$\tilde{D}_q^h(x,z) = \frac{\#h : [l(N,q) \longrightarrow l'hX](x,z)}{\#[l(N,q) \longrightarrow l'X](x)}, \tag{6.2}$$

where $\#[l(N,q) \longrightarrow l'X](x,z)$ is the number of generated events where a quark of flavour q was struck. The purities for a given set of parton density functions $q(x)$ can then be calculated by

$$P_q^h(x,z) = \frac{\tilde{D}_q^h(x,z)e_q^2 q(x)}{\sum_{q'} \tilde{D}_{q'}^h(x,z)e_{q'}^2 q'(x)}, \tag{6.3}$$

which is possible to do without rerunning the Monte Carlo. A more explicit review of this technique can be found in [Dür97]. Furthermore (6.2) allows the construction of purities directly from measured fragmentation functions. An analysis based on this ansatz was performed by SMC [Pre97, SMC98].

Using the LUND string fragmentation model tuned to HERMES data (see Figure 3.3) and the leading order parton densities from [GRV95], the proton purities are generated as shown in Figure 6.3. Here the same cuts as used for the data extraction (Table 5.2) were applied which is the reason for the drop of the purities for $z < 0.2$ in the two-dimensional plots. Above this cut the purities used in this analysis are almost flat in z. See also Figure 6.4 for the purities of the neutron as needed for the interpretation of helium data. The generation of a high-statistics purity sample of $20 \cdot 10^6$ events takes about 10 hours.

The dependence of the purity matrix on the input parameters contributes to the systematical error on the extracted quark polarisations as will be discussed in Section 6.6.2. Note that the treatment of the statistical errors of the purity matrix is not trivial since all entries are correlated. But the statistical uncertainty can be suppressed by generating large purity samples so that its size is negligible compared to the systematical effects due to different parton density functions and hadronisation models. For this reason the statistical error on the purities will be neglected in this analysis.

6.2 Inverting the Purity Equation

The extraction of the quark polarisations in the nucleon from the particle asymmetries as they were measured in Chapter 5 is technically equivalent to

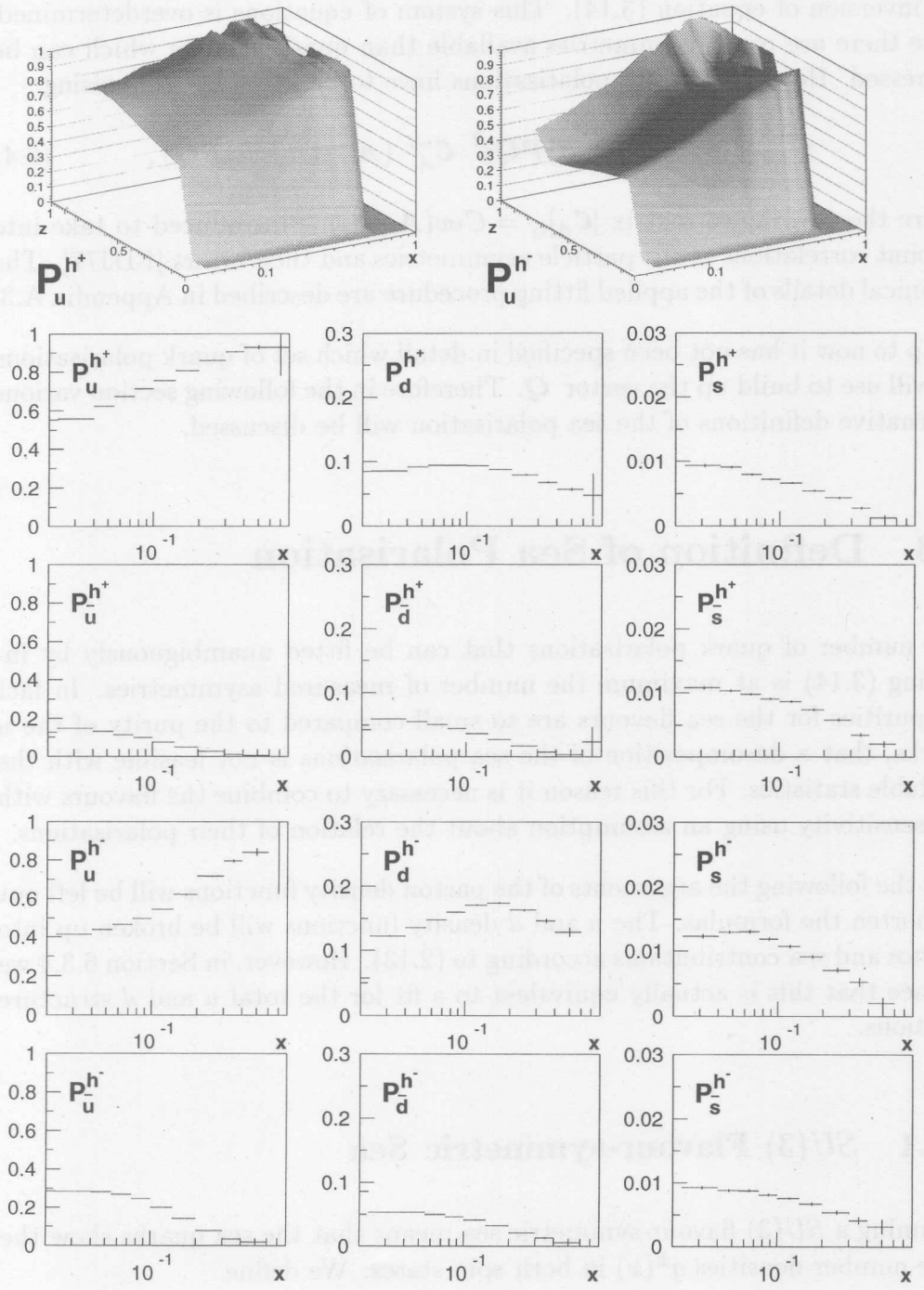

Figure 6.3: Quark Purities on Hydrogen. *The upper two-dimensional plots show some hadron purities for the u quark in the (z, x)-plane. The uneven structure at high x is an artefact from low Monte Carlo statistics in that region. The lower plots show the complete set of hadron purities for each x_{Bj}-bin integrated over $0.2 < z < 1$. Note that the scales differ for the various quark flavours.*

the inversion of equation (3.14). This system of equations is overdetermined, since there are more asymmetries available than quark flavours which can be addressed. Hence the quark polarisations have to be fitted by minimising

$$\chi^2 = (\boldsymbol{A} - (1+R)\boldsymbol{\mathcal{P}}\boldsymbol{Q})^T \, \boldsymbol{\mathcal{C}}_A^{-1} \, (\boldsymbol{A} - (1+R)\boldsymbol{\mathcal{P}}\boldsymbol{Q}), \tag{6.4}$$

where the covariance matrix $[\boldsymbol{\mathcal{C}}_A]_{ij} = Cov(\boldsymbol{A}_i, \boldsymbol{A}_j)$ is introduced to take into account correlations of the particle asymmetries and their errors [EDJ77]. The technical details of the applied fitting procedure are described in Appendix A.3.

Up to now it has not been specified in detail which set of quark polarisations we will use to build up the vector $\boldsymbol{Q}$. Therefore in the following section various alternative definitions of the sea polarisation will be discussed.

6.3 Definition of Sea Polarisation

The number of quark polarisations that can be fitted unambiguously by inverting (3.14) is at maximum the number of measured asymmetries. In fact the purities for the sea flavours are so small compared to the purity of the u quarks, that a decomposition of the sea polarisations is not feasible with the available statistics. For this reason it is necessary to combine the flavours with low sensitivity using an assumption about the relation of their polarisations.

In the following the arguments of the parton density functions will be left out to shorten the formulas. The u and d density functions will be broken up into valence and sea contributions according to (2.13). However, in Section 6.3.4 we will see that this is actually equivalent to a fit for the total u and d structure functions.

6.3.1 $SU(3)$ Flavour-symmetric Sea

Assuming a $SU(3)$ flavour-symmetric sea means that the sea quarks show the same number densities $q^{\pm}(x)$ in both spin states. We define

$$\frac{1}{6}\Delta\bar{q}_{SU(3)} = \Delta u_s = \Delta\bar{u} = \Delta d_s = \Delta\bar{d} = \Delta s = \Delta\bar{s}, \tag{6.5}$$

where the factor $1/6$ was introduced such that $\Delta\bar{q}$ gives the polarised structure function for the total sea. The contribution of the sea to the measured asymmetries can then be written as

$$P^h_{\bar{q}_{SU(3)}} \cdot \frac{\Delta\bar{q}_{SU(3)}}{\bar{q}} = \frac{\Delta\bar{q}_{SU(3)}}{6}\left(\frac{P^h_{u_s}}{u_s} + \frac{P^h_{\bar{u}}}{\bar{u}} + \frac{P^h_{d_s}}{d_s} + \frac{P^h_{\bar{d}}}{\bar{d}} + \frac{P^h_{s}}{s} + \frac{P^h_{\bar{s}}}{\bar{s}}\right), \quad (6.6)$$

and subsequently the purity of the sea is defined as

$$P^h_{\bar{q}_{SU(3)}} = \frac{1}{6}\left(\frac{\bar{q}}{u_s}P^h_{u_s} + \frac{\bar{q}}{\bar{u}}P^h_{\bar{u}} + \frac{\bar{q}}{d_s}P^h_{d_s} + \frac{\bar{q}}{\bar{d}}P^h_{\bar{d}} + \frac{\bar{q}}{s}P^h_{s} + \frac{\bar{q}}{\bar{s}}P^h_{\bar{s}}\right), \quad (6.7)$$

where we defined the unpolarised sea $\bar{q}$ as[2]

$$\bar{q} = u_s + \bar{u} + d_s + \bar{d} + s + \bar{s}. \quad (6.8)$$

6.3.2 Polarisation-symmetric Sea

Since the $SU(3)$ flavour-symmetry of the sea is known to be broken in the unpolarised case (see Section 2.6.1), there is no strong reason that assumption (6.5) is strictly true. An alternative assumption would be that the sea polarisations are the same for all flavours:

$$\left(\frac{\Delta\bar{q}}{\bar{q}}\right)_{Pol} = \frac{\Delta u_s}{u_s} = \frac{\Delta\bar{u}}{\bar{u}} = \frac{\Delta d_s}{d_s} = \frac{\Delta\bar{d}}{\bar{d}} = \frac{\Delta s}{s} = \frac{\Delta\bar{s}}{\bar{s}}, \quad (6.9)$$

In this case the purity of the sea is defined simply as the sum of all sea contributions,

$$P^h_{\bar{q}_{Pol}} = P^h_{u_s} + P^h_{\bar{u}} + P^h_{d_s} + P^h_{\bar{d}} + P^h_{s} + P^h_{\bar{s}}, \quad (6.10)$$

and since

$$\Delta\bar{q}_{Pol} = \frac{\Delta\bar{q}}{\bar{q}}u_s + \frac{\Delta\bar{q}}{\bar{q}}\bar{u} + \frac{\Delta\bar{q}}{\bar{q}}d_s + \frac{\Delta\bar{q}}{\bar{q}}\bar{d} + \frac{\Delta\bar{q}}{\bar{q}}s + \frac{\Delta\bar{q}}{\bar{q}}\bar{s}, \quad (6.11)$$

the unpolarised sea is fixed to the form of (6.8).

6.3.3 Unpolarised Sea

Another choice for the sea polarisation is to assume that it does not contribute at all to the nucleon spin. Of course this variant is not motivated physically

[2] One is free to choose any definition of $\bar{q}$ as long as the same definition is used in (6.6) and (6.7). Here the unpolarised sea was chosen in the canonical way to be consistent with the QPM picture and section 6.3.2.

but allows one to check how significant the extractions using assumption (6.9) or (6.5) are.

Assuming an unpolarised sea is technically equivalent to ignore all contributions from sea quarks to the asymmetries in (3.12) or to set the sea purity to zero:

$$P^h_{\bar{q}_{Unpol}} = 0. \tag{6.12}$$

6.3.4 Valence and Sea Contributions of u and d Quarks

Up to now we have split the valance and sea parts of the u and d quarks according to (2.13). However, with the Monte Carlo generator used in this analysis, this is equivalent to a fit for the total structure functions. In the current implementation of LEPTO there is no difference in the fragmentation of valence and sea part of the u and d flavours, i.e. the purities of these quarks can be expressed as

$$P^h_{q_v} = P^h_q \cdot \frac{q_v}{q}, \qquad P^h_{q_s} = P^h_q \cdot \frac{q_s}{q}. \tag{6.13}$$

Under this condition the splitting of the u and d quark fields in a valence and sea part in equation (3.14) is equivalent to a fit on the sum of both contributions. From (6.13) and (2.13) follows:

$$P^h_q \frac{\Delta q}{q} = P^h_{q_v} \frac{\Delta q_v}{q_v} + P^h_{q_s} \frac{\Delta q_s}{q_s}. \tag{6.14}$$

It should be noted that in case of a combined fit the sea definition (6.8) changes to

$$\bar{q} = \bar{u} + \bar{d} + s + \bar{s}, \tag{6.15}$$

and that the factor 6 in equation (6.5) has to be replaced by 4.

6.4 Interpretation of ^{3}He Data

It is not trivial to use the asymmetries from the helium target in the purity method since the helium nucleus consists of a mixture of polarised and unpolarised nucleons. If one would use a purity matrix generated on an unpolarised helium target to translate the measured hadron asymmetries into quark polarisations, the result would only be the effective polarisation of the quarks in

the nucleus and not the polarisations in a nucleon. Hence these polarisations had to be transformed in a subsequent step into the quark polarisations of the proton. Note that in this scheme we would have to apply the model for the nucleus at two different points, once while generating the purities and a second time for the interpretation of the effective quark polarisations.

In this analysis a different approach is pursued by translating the measured asymmetries of helium $\boldsymbol{A}_{He}$ first into the asymmetries $\boldsymbol{A}_n$, as they would be seen on a neutron target. Then on an ideal neutron target the purities $\boldsymbol{\mathcal{P}}_n$ are generated as shown in Figure 6.4 and finally the following extended version of equation (3.14)

$$\begin{pmatrix} \boldsymbol{A}_p \\ \boldsymbol{A}_n \end{pmatrix} = (1+R) \begin{pmatrix} \boldsymbol{\mathcal{P}}_p \\ \boldsymbol{\mathcal{P}}_n \end{pmatrix} \boldsymbol{Q} \tag{6.16}$$

is inverted to extract the quark polarisations from both kinds of targets.

To answer the question of how to transform an asymmetry A^h_{He} measured on helium into an asymmetry A^h_n on the neutron, we split it in the following way into proton and neutron contributions:

$$A^h_{He} = f^h_p p^p_{He} A^h_p + f^h_n p^n_{He} A^h_n, \tag{6.17}$$

where $p^p_{He} = -0.027$ and $p^n_{He} = 0.865$ are the effective proton and neutron polarisations in the ^{3}He nucleus [FGP90], A^h_p is the asymmetry as it would be measured in scattering off bare protons and $f^h_{p,n}$ are the proton (neutron) dilution factor giving the probability that the reaction took place on one of the two protons or the neutron. The dilution factors obviously add up to one and f^h_p can be rewritten in the following way:

$$\begin{aligned} f^h_p &= \frac{2\sigma^p_h}{\sigma^{He}_h} \\ &= 2\frac{N^p_h}{N^{He}_h}\frac{\mathcal{L}_{He}}{\mathcal{L}_p} = 2\frac{N^p_h}{N^{He}_h}\frac{N^{He}_{DIS}}{N^p_{DIS}}\frac{\sigma^p_{DIS}}{\sigma^{He}_{DIS}} \\ &= 2\frac{n^p_h}{n^{He}_h}\frac{\sigma^p_{DIS}}{\sigma^{He}_{DIS}}, \end{aligned} \tag{6.18}$$

where $\sigma^{p,n,He}_h$ is in extension to Chapter 5 the integral of the unpolarised differential cross-section over the kinematic region of interest on the proton, neutron or helium, $\mathcal{L}_{p,He}$ is the integrated luminosity on either target, $N^{p,He}_h$ is the number of hadrons seen in the final states of the events on a selected target and $n^{p,He}_h$ are the averaged hadron multiplicities on both targets. If we assume

$$\sigma^{He}_h = \sigma^d_h + \sigma^p_h, \tag{6.19}$$

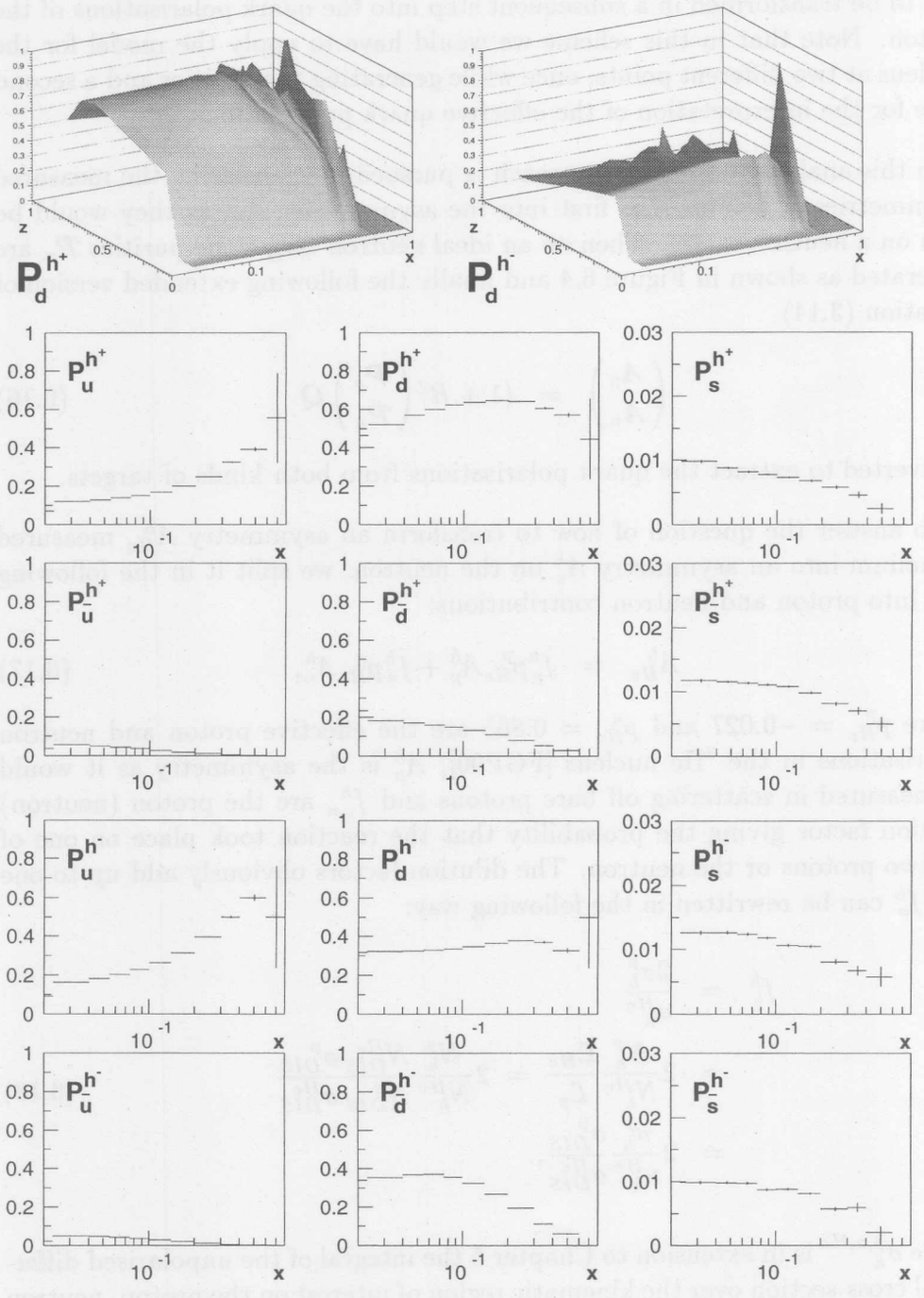

Figure 6.4: Quark-Purities on Neutron. *The neutron purities are not only the iso-spin and charge conjugated purities of the proton because of the charge factor in (3.11). See also caption of Figure 6.3.*

we can express f_p^h only in terms of measured quantities:

$$f_p^h(x,Q^2) \;=\; 2\frac{n_h^p}{n_h^{He}}\left(\frac{F_2^p(x,Q^2)}{2F_2^d(x,Q^2)+F_2^p(x,Q^2)}\right). \tag{6.20}$$

Figure 6.5 gives an impression of the (x,Q^2) dependence of f_p^{DIS} for inclusive processes ($n_{DIS}^p = n_{DIS}^{He} = 1$). See Table B.2 in Appendix B for the measured mean particle multiplicities on both targets. Note that the multiplicity ratios for pions are large because of different Čerenkov momentum thresholds of the datasets.

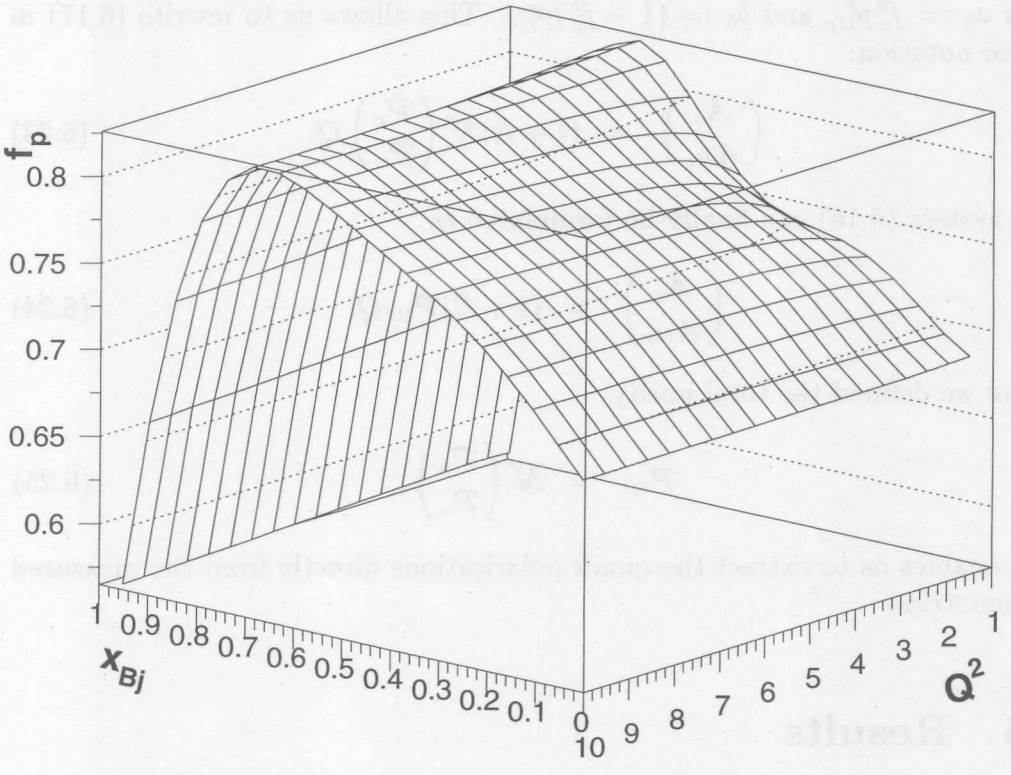

Figure 6.5: Inclusive Dilution Factor f_p^{DIS} on ^{3}He. *The values were calculated using the NMC P15 data set [NMC92]. Note that the vertical axis is cut off at the bottom.*

Using $f_p^h + f_n^h = 1$, (6.17) and (6.20) we have found the recipe to transform an asymmetry measured on helium into the asymmetry on the neutron:

$$A_n^h \;=\; \frac{1}{p_{He}^n(1-f_p^h)}\left(A_{He}^h - f_p^h p_{He}^p A_p^h\right), \tag{6.21}$$

which holds for every kinematic bin.

To express (6.16) in terms of the measured asymmetries, the nuclear mixing matrix $\mathcal{N}$ is defined as

$$\mathcal{N} = \begin{pmatrix} 1 & & & & \\ & \ddots & & 0 & \\ & & 1 & & \\ a_{h_1} & & & b_{h_1} & \\ & \ddots & & & \ddots \\ & & a_{h_m} & & b_{h_m} \end{pmatrix}, \tag{6.22}$$

with $a_h := f_p^h p_{He}^p$ and $b_h := (1 - f_p^h) p_{He}^n$. This allows us to rewrite (6.17) in vector notation:

$$\begin{pmatrix} \boldsymbol{A}_p \\ \boldsymbol{A}_{He} \end{pmatrix} = (1+R)\mathcal{N} \begin{pmatrix} \mathcal{P}_p \\ \mathcal{P}_n \end{pmatrix} \boldsymbol{Q}. \tag{6.23}$$

The system (6.16) can finally be formulated as

$$\begin{pmatrix} \boldsymbol{A}_p \\ \boldsymbol{A}_{He} \end{pmatrix} = (1+R)\mathcal{P}_{tot}\boldsymbol{Q}, \tag{6.24}$$

where we defined the total purity

$$\mathcal{P}_{tot} = \mathcal{N} \begin{pmatrix} \mathcal{P}_p \\ \mathcal{P}_n \end{pmatrix}, \tag{6.25}$$

that enables us to extract the quark polarisations directly from the measured asymmetries.

6.5 Results

After discussing all necessary input quantities to the inversion of equation (3.14) the extracted polarised parton density functions will be presented in the following section. In Chapter 7 the results will then be compared to other methods, measurements and theoretical predictions. The estimation of systematic uncertainties on the results will be discussed in Section 6.6.

6.5.1 Polarised Parton Density Functions

In Figure 6.6 the resulting quark spin distributions are shown as extracted from inclusive and hadron asymmetries (Figures 5.4 and 5.5) using the LUND string

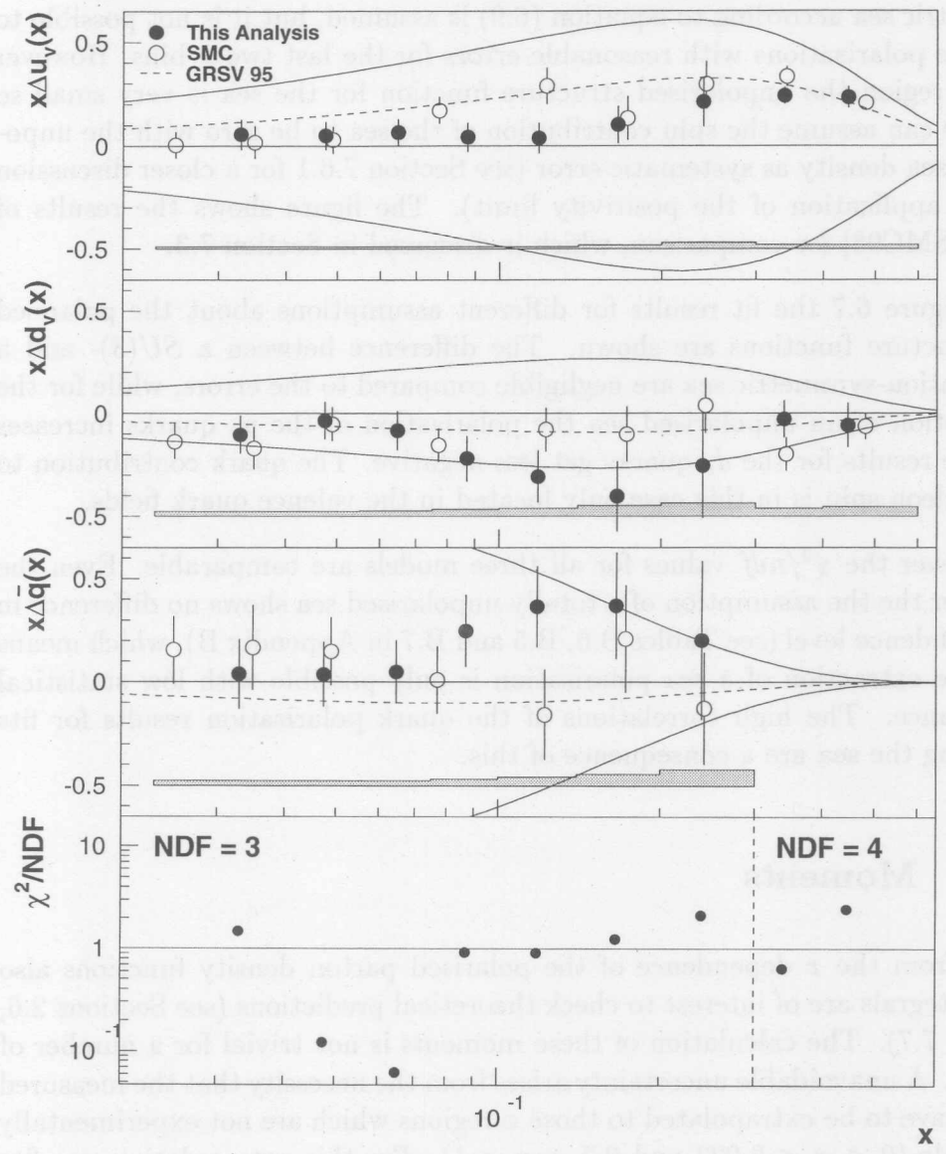

Figure 6.6: The Extracted Polarised PDFs. *The hadron and inclusive asymmetries on the ^{3}He and hydrogen targets were used to extract the polarised parton density functions according to equation (6.24). A polarisation-symmetric sea was assumed and the results are plotted for the measured Q^2 of each bin. The grey bands show the systematic errors. The solid line indicates the unpolarised PDFs (positivity limit) as parametrised by [GRV95], the dashed lines show the polarised part from [GRSV95]. The open points show the results from SMC [SMC98] for a $SU(3)$-symmetric sea at $Q^2 = 10$ (GeV/c)^2. The sea result from SMC was multiplied by 6 to be compatible with definition (6.5).*

fragmentation model (Section 3.3). For the first seven x bins a polarisation-symmetric sea according to equation (6.9) is assumed, but it is not possible to fit three polarisations with reasonable errors for the last two x bins. However in this region the unpolarised structure function for the sea is very small so that we can assume the spin contribution of the sea to be zero with the unpolarised sea density as systematic error (see Section 7.6.1 for a closer discussion of this application of the positivity limit). The figure shows the results of SMC [SMC98] for comparison, which is discussed in Section 7.3.

In Figure 6.7 the fit results for different assumptions about the polarised sea structure functions are shown. The difference between a $SU(3)$- and a polarisation-symmetric sea are negligible compared to the errors, while for the assumption of an unpolarised sea the polarisation of the u_v quarks increases and the results for the d_v quarks get less negative. The quark contribution to the nucleon spin is in this case only located in the valence quark fields.

However the χ^2/ndf values for all three models are comparable. Even the fit under the the assumption of a totally unpolarised sea shows no difference in the confidence level (see Tables B.6, B.5 and B.7 in Appendix B), which means that the extraction of a sea polarisation is only possible with low statistical significance. The high correlations of the quark polarisation results for fits including the sea are a consequence of this.

6.5.2 Moments

Apart from the x dependence of the polarised parton density functions also their integrals are of interest to check theoretical predictions (see Sections 2.6, 7.5 and 7.7). The calculation of these moments is not trivial for a number of reasons. A unavoidable uncertainty arises from the necessity that the measured PDFs have to be extrapolated to those x regions which are not experimentally accessible ($0 < x < 0.023$ and $0.7 < x < 1$). For this extrapolation one fits parametrised functions $f_q(x)$ suggested by a reasonable physical model to the data and integrates this function in the unmeasured region. A more technical problem is imposed by the fact, that for statistical reasons the polarised parton density functions are measured in rather wide bins (especially in the high x region). This means that one can not simply fit the measured asymmetries with the model function $f_q(x)$ but one has to take into account the bin population (or event) density $n(x)$. For the same reason the integral over the measured region (i.e. the region covered by bins) is not simply given by the sum of the bin values. For a correct integration a model function $f_q(x)$ as well as the density function $n(x)$ has to be known. For a more detailed discussion of this problem refer to Appendix A.4.

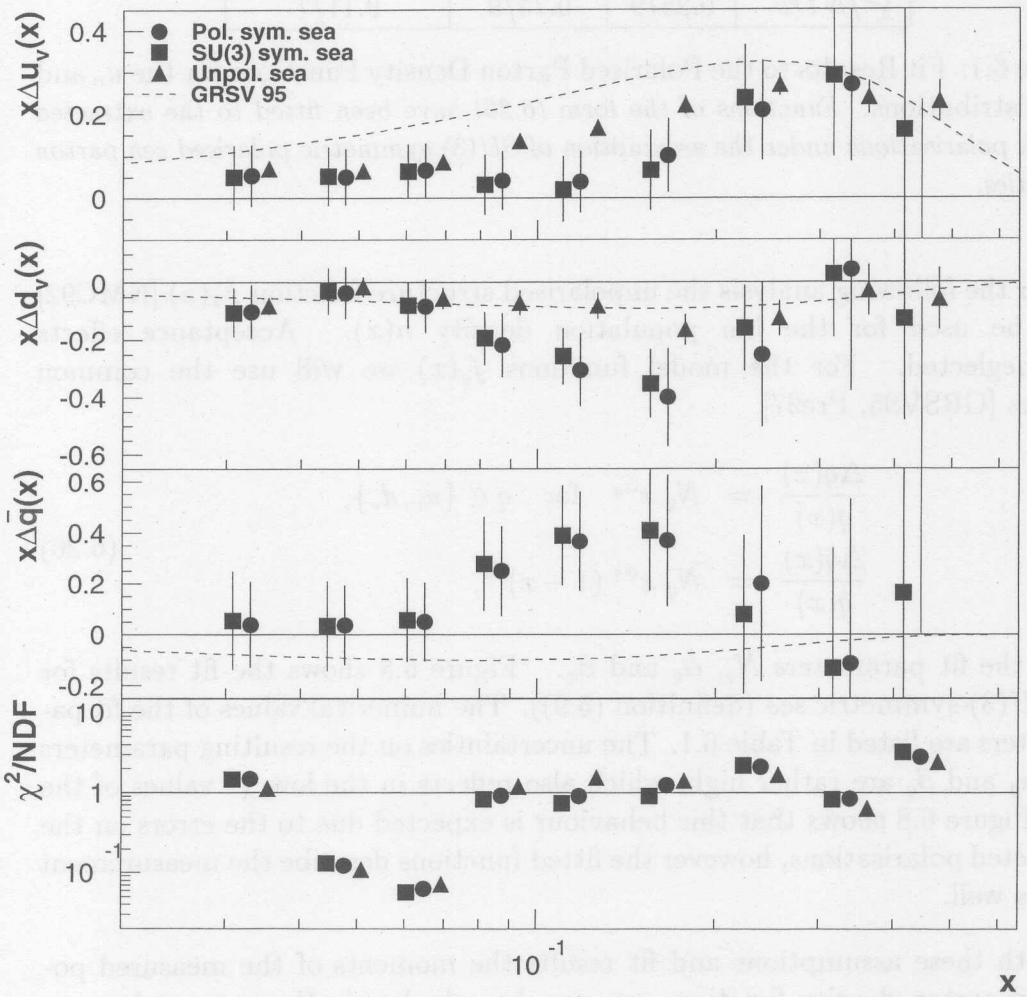

Figure 6.7: Results for different Sea Definitions. *The results for a $SU(3)$ symmetric and an unpolarised sea are located at the same x as the points for the polarisation-symmetric sea, they were shifted for a clear layout. The dashed lines show the polarised distributions from [GRSV95]. Statistical errors only, the results as well as the parametrised PDFs are plotted at the measured Q^2. The dots of the first seven bins and the triangles of the last two bins correspond to the data plotted in Figure 6.6.*

Parameter	Δu_v	Δd_v	$\Delta\bar{q}$
N_q	$1.5_{\pm 0.7}$	$-0.96_{\pm 0.5}$	$1.7 \cdot 10^{4}{}_{\pm 3.5 \cdot 10^{4}}$
α_q	$1.2_{\pm 0.44}$	$0.15_{\pm 0.22}$	$3.8_{\pm 0.85}$
β_q	—	—	$16_{\pm 6.6}$
χ^2/NDF	0.25/9	0.73/9	0.11/7

Table 6.1: Fit Results to the Polarised Parton Density Functions for the u_v and d_v Distributions. *Functions of the form (6.26) have been fitted to the extracted quark polarisations under the assumption of $SU(3)$ symmetric polarised sea parton densities.*

For the following analysis the unpolarised structure function $F_2(x)$ [NMC92] will be used for the bin population density $n(x)$. Acceptance effects are neglected. For the model functions $f_q(x)$ we will use the common ansatz [GRSV95, Pre97]

$$\begin{aligned} \frac{\Delta q(x)}{q(x)} &= N_q \, x^{\alpha_q} \quad \text{for} \quad q \in \{u_v, d_v\}, \\ \frac{\Delta \bar{q}(x)}{\bar{q}(x)} &= N_{\bar{q}} \, x^{\alpha_{\bar{q}}} \, (1-x)^{\beta_{\bar{q}}}, \end{aligned} \tag{6.26}$$

with the fit parameters N_q, α_q and β_q. Figure 6.8 shows the fit results for an $SU(3)$-symmetric sea (definition (6.9)). The numerical values of the fit parameters are listed in Table 6.1. The uncertainties on the resulting parameters N_q, α_q and β_q are rather high, which also reflects in the low χ^2 values of the fits. Figure 6.8 shows that this behaviour is expected due to the errors on the extracted polarisations, however the fitted functions describe the measurement points well.

With these assumptions and fit results the moments of the measured polarised parton density functions can now be calculated. However we have to take into account, that the distributions are measured at different Q^2 in each bin (see Table B.1) and that we are actually interested in the moments at a fixed Q^2. For this reason we had to evolve the polarisations $\Delta q/q$ to a common Q_0^2 before calculating the fits and integrals. In this analysis a simpler approach is pursued by assuming that the polarisations are approximately independent of Q^2. This procedure is motivated by the fact that the measured inclusive asymmetry g_1/F_1 depends only weakly on Q^2 since the evolution of g_1 and F_1 is approximately the same for our x region [GS96b, AP77]. Under this assumption we can calculate a moment at Q_0^2 by multiplying the polarisation $\Delta q/q$ by the unpolarised density $q(x, Q^2)$ evaluated at Q_0^2. The resulting first and second moments are listed in Table 6.2 for $Q_0^2 = 2.3$ (GeV/c)^2, which is the mean Q^2 of the HERMES data.

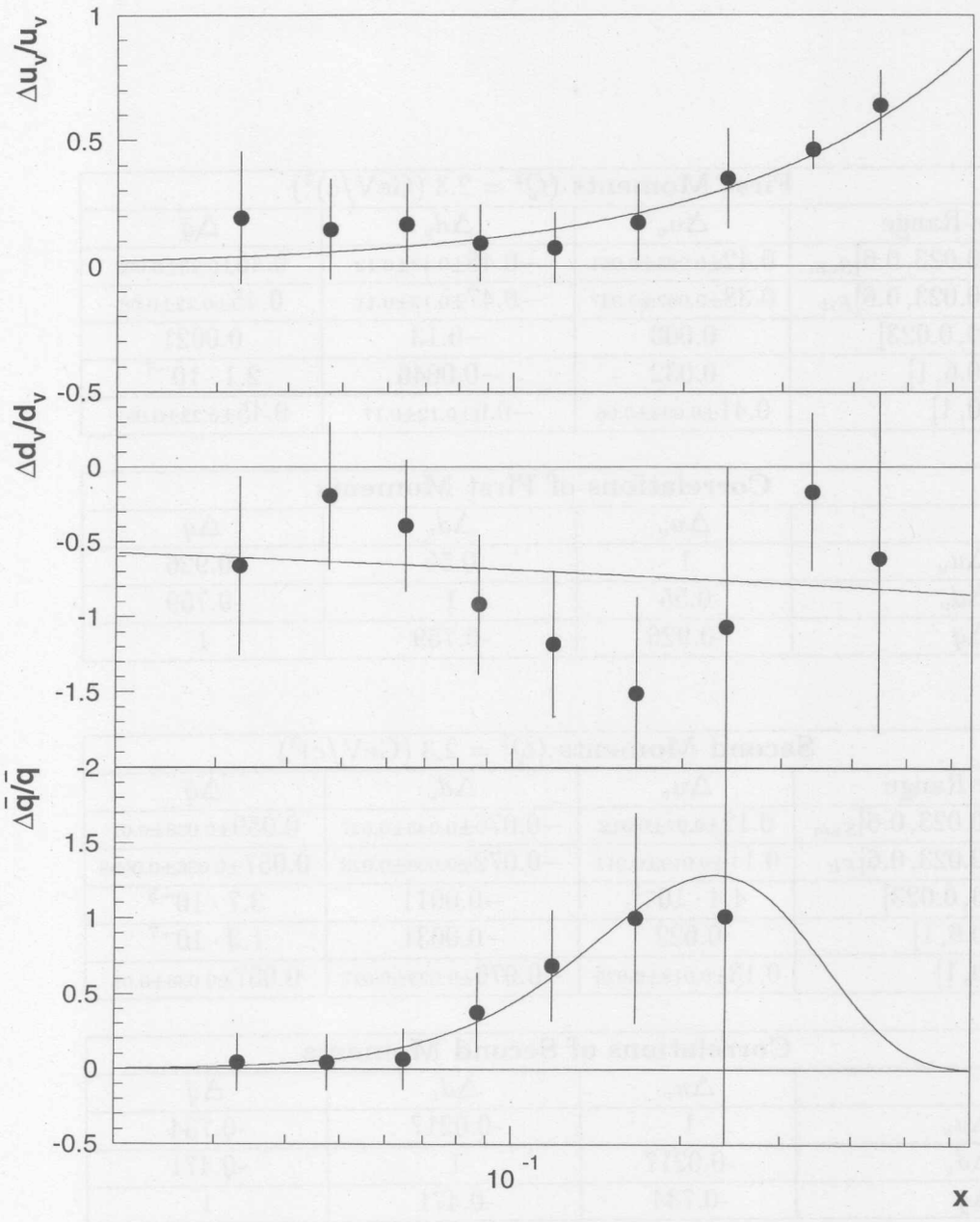

Figure 6.8: Fits to Quark Polarisations. *Model functions of the form (6.26) have been fitted to bin-wise measured quark polarisations according to the procedure described in Appendix A.4. The fit results are shown as lines, the measured polarisations under the assumption of $SU(3)$-symmetric polarised sea PDFs are plotted as dots for the measured Q^2. The fit results are used mainly for extrapolating the unmeasured region. Statistical errors only.*

First Moments ($Q^2 = 2.3$ (GeV/c)^2)			
x-Range	Δu_v	Δd_v	$\Delta \bar{q}$
$[0.023, 0.6]_{Sum}$	$0.42_{\pm 0.095 \pm 0.051}$	$-0.48_{\pm 0.13 \pm 0.12}$	$0.46_{\pm 0.23 \pm 0.082}$
$[0.023, 0.6]_{Fit}$	$0.38_{\pm 0.092 \pm 0.047}$	$-0.47_{\pm 0.12 \pm 0.11}$	$0.45_{\pm 0.22 \pm 0.08}$
$[0, 0.023]$	0.003	-0.13	0.0021
$[0.6, 1]$	0.032	-0.0046	$2.1 \cdot 10^{-7}$
$[0, 1]$	$0.41_{\pm 0.092 \pm 0.06}$	$-0.6_{\pm 0.12 \pm 0.17}$	$0.45_{\pm 0.22 \pm 0.082}$

Correlations of First Moments			
	Δu_v	Δd_v	$\Delta \bar{q}$
Δu_v	1	0.55	-0.926
Δd_v	0.55	1	-0.759
$\Delta \bar{q}$	-0.926	-0.759	1

Second Moments ($Q^2 = 2.3$ (GeV/c)^2)			
x-Range	Δu_v	Δd_v	$\Delta \bar{q}$
$[0.023, 0.6]_{Sum}$	$0.12_{\pm 0.02 \pm 0.012}$	$-0.076_{\pm 0.035 \pm 0.027}$	$0.059_{\pm 0.038 \pm 0.01}$
$[0.023, 0.6]_{Fit}$	$0.11_{\pm 0.019 \pm 0.011}$	$-0.072_{\pm 0.029 \pm 0.023}$	$0.057_{\pm 0.036 \pm 0.0098}$
$[0, 0.023]$	$4.4 \cdot 10^{-5}$	-0.0011	$3.7 \cdot 10^{-5}$
$[0.6, 1]$	0.022	-0.0031	$1.3 \cdot 10^{-7}$
$[0, 1]$	$0.13_{\pm 0.019 \pm 0.025}$	$-0.076_{\pm 0.029 \pm 0.027}$	$0.057_{\pm 0.036 \pm 0.01}$

Correlations of Second Moments			
	Δu_v	Δd_v	$\Delta \bar{q}$
Δu_v	1	-0.0217	-0.734
Δd_v	-0.0217	1	-0.471
$\Delta \bar{q}$	-0.734	-0.471	1

Table 6.2: Moments of Polarised Parton Density Functions for the u_v and d_v Distributions. *See text.*

The moments in the measured region have been integrated in two ways, by summing up the polarised parton density functions in a "naive" way according to (A.24) and also by using the fitted function to apply population density corrections as described in equation (A.25). The latter result was used to derive the total moment. To take the extrapolation uncertainty into account a systematic error of 100% has been assigned to the contributions of the extrapolated regions. It has been argued that for high x values the polarised PDFs are limited by the unpolarised distributions, which would lead to negligible contributions to the integrals [SMC98]. However the results of this analysis shows that this is only true for the sea quarks, the contribution to the valence quarks is sizable. The table lists also the correlations of the moments. These have been calculated only for the measured region by adding the variance matrices of the contributing bins and are therefore only estimated values. A mathematically sound extraction of the correlations is not trivial. A global fit of all three model functions had to be performed yielding the correlations of the parameters which then had to be taken into account for the calculation of the correlations of the moments. Appendix B contains fit results and moments calculated for other symmetry assumptions of the sea and valence/sea combinations of the u and d quarks. No significant differences are seen.

6.6 Systematic Error

After presenting the results of this purity analysis, we will discuss in this section the various systematic uncertainties on the extracted polarised PDFs as indicated as error band in Figure 6.6. The total systematic error on the result originates from two different classes of input uncertainties: Systematic errors on the measurement of the asymmetries and the variation of the purity matrix when different unpolarised parton density functions and fragmentation models are used for its generation. In this section an estimation of these contributions to the systematic error on the result will be presented. Strictly speaking the χ^2 of the fit allows one to check how well the linear model (3.14) describes the data, which also can be interpreted as a systematic uncertainty. However the statistical errors on the asymmetries are too large to allow such an interpretation. In particular the χ^2/ndf values of all fits don't show outliers that are big compared to one (see Appendix B).

6.6.1 Errors on Asymmetries

The contributions of the systematic errors of the asymmetries to the result were estimated by performing the fit (6.4) once with a matrix of statistical covariances $\mathcal{C}_A^{stat}$ only and once with the total covariances $\mathcal{C}_A^{tot} = \mathcal{C}_A^{stat} + \mathcal{C}_A^{sys}$. The difference of the diagonal elements in the covariance matrices of both results are interpreted as the squared systematic error:

$$\mathcal{C}_Q^{sys} = \mathcal{C}_Q^{tot} - \mathcal{C}_Q^{stat}. \tag{6.27}$$

Target Polarisation

The systematic errors on the asymmetries on the polarised helium and hydrogen targets are not correlated since both the sources and the polarimeters were implemented by using very different techniques. The relative systematic errors were assumed to be $\delta p_T^{He} = \Delta p_T^{He}/p_T^{He} = 5\%$ in 1995 and $\delta p_T^p = \Delta p_T^p/p_T^p = 7\%$ for 1996 (see Table 4.1) and propagate directly to all measured asymmetries of the corresponding year. Hence the contribution to the covariance matrix is:

$$\left[\mathcal{C}_A^{sys,Targ}\right]_{ij} = cor(\delta p_{T,i}, \delta p_{T,j}) \cdot A_i \delta p_{T,i} \cdot A_j \delta p_{T,j}, \tag{6.28}$$

where the correlation $cor(\delta p_{T,i}, \delta p_{T,j})$ of the errors is one for asymmetries of the same year and vanishes for different years. $\delta p_{T,i}$ is the same for all asymmetries from one year.

Beam Polarisation

Unlike the target polarisation, the beam polarisation was measured with the same apparatus for both sets of asymmetries. Therefore parts of the systematic errors are correlated. The main contribution to the uncertainty is given by a calibration constant which is derived as a function of the rise time constant and asymptotic polarisation in equation (4.1). This constant has a fractional error of $\delta p_B^{rise} = 3.29\%$ [Bar95] and is the same (and expected to be 100% correlated) for both years. Other contributions to the systematic errors are assumed to be uncorrelated have values of $\Delta p_B^{He}/p_B^{He} \leq 4.0\%$ in 1995 and $\Delta p_B^p/p_B^p = 0.87\%$ for 1996 [Bar95, Tip97]. The contribution to the covariance matrix is then given by

$$\left[\mathcal{C}_A^{sys,Beam}\right]_{ij} = \left((\delta p_B^{rise})^2 + cor(\delta p_{B,i}, \delta p_{B,j}) \delta p_{B,i} \delta p_{B,j}\right) \cdot A_i A_j, \tag{6.29}$$

with the same meaning of the correlation and indices on the polarisations as in (6.28).

Smearing corrections

As discussed in Section 5.3.1 the measured asymmetries have to be corrected for kinematic smearing of the spectrometer. This correction factors are derived from Monte Carlo studies and therefore have uncertainties of statistical nature (coming from the final number of generated events) as well as of systematic origin (for instance the correction factor on asymmetries depends on the asymmetry itself). The total error on the correction factors (see Figure 5.2) enters the spin decomposition analysis as a systematic error. Its contribution to the covariance matrix is given by

$$\left[\mathcal{C}_A^{sys,Smear}\right]_{ij} = cor(\Delta S_i, \Delta S_j) \cdot A_i \Delta S_i \cdot A_j \Delta S_j, \tag{6.30}$$

where the correlation $cor(\Delta S_i, \Delta S_j)$ of the absolute errors ΔS on the smearing correction factors is one for asymmetries of the same year and is assumed to vanish for different targets.

Yield Fluctuations

The careful statistical evaluation of the data taken on helium revealed that the statistical error on the measured asymmetries is underestimating the true error, which is explained by yield fluctuations causing wrong asymmetries[3]. For this kind of analysis an ensemble of asymmetries is extracted from the data sample by randomising the sign of the target polarisation. The distribution of this asymmetries is centred around zero and shows a width ΔA_{tot} which is higher than the statistical error of the asymmetries ΔA_{stat} as calculated from equation (A.7):

$$\Delta A_{tot} = \sqrt{\Delta A_{stat}^2 + \Delta A_{yield}^2}. \tag{6.31}$$

The contribution ΔA_{yield} can be determined separately for all asymmetries and is interpreted as a systematic error coming from yield fluctuations[4]. Usually the systematic contribution is normalised to the statistical error: $y = \Delta A_{yield}/\Delta A_{stat}$. The measured values for 1995 are $y_{e+} = 44\%$, $y_{h+} = 40\%$ and $y_{h-} = 31\%$ [HER97a, Tal98]. Assuming that the yield fluctuations show the same correlations as the asymmetries, $cor(A_i, A_j)$, their contribution to the covariance matrix can be expressed as

$$\left[\mathcal{C}_A^{sys,Yield}\right]_{ij} = cor(A_i, A_j)\Delta A_i \Delta A_j \cdot \left(\sqrt{(1+y_i^2)(1+y_j^2)} - 1\right). \tag{6.32}$$

[3] A similar study was done for the hydrogen asymmetries. No significant effect was found in this case [Stö98].

[4] In this short summary the true asymmetry which is also contributing to ΔA_{tot} was neglected. For a detailed description of the method see [HER97a].

Systematic error of $R(x, Q^2)$

An additional contribution to the systematic error is given by the uncertainty of the ratio of longitudinal and transverse cross sections $R(x, Q^2)$ which due to (3.8) can be treated as a correlated systematic uncertainty on the measured asymmetries. One has to take into account, that the depolarisation factor in (3.8) also depends on $R(x, Q^2)$. The contribution to the covariance matrix is then given by

$$\left[\mathcal{C}_A^{sys,R}\right]_{ij} = A_i \cdot A_j \cdot \delta R^2, \tag{6.33}$$

where

$$\delta R = \frac{y}{(2-y)(1+R(x,Q^2))^2} \Delta R(x, Q^2); \tag{6.34}$$

is evaluated for the mean y, x and Q^2 values of each bin.

6.6.2 Errors on Purities

A proper estimation of systematic error on the fitted quark polarisations caused by uncertainties on the purities is hard to accomplish for two reasons. First it is not easy to introduce (correlated) uncertainties on the purity matrix $\mathcal{P}$ in equation (3.14), but more important it is not trivial to quantify this uncertainties and correlations analytically as a function of e.g. the errors on the unpolarised parton density functions and on the fragmentation parameters (provided that these are known). For this reason the analysis was performed with two different parton density function sets ([GRV95] and [MRS94a, MRS94b]) and fragmentation models (LUND string model and independent fragmentation, see Section 3.3), using the difference in the results as a measure for the contribution of the purity uncertainties to the final systematic error. Since the second parton density function set is a next-to-leading-order (NLO) fit using the modified minimal subtraction ($\overline{\text{MS}}$) factorisation/renormalisation scheme [ESW96] (in contrast to the discussion in Section 3.5) the systematic error introduced by this difference might be overestimated.

6.6.3 Decomposition of Systematic Errors

We now will disentangle the fractional contributions of the discussed systematic uncertainties to the total systematic errors as shown in the error bands in Figure 6.6. The fraction of a given error was estimated by fitting the quark

polarisations with all systematic errors but the one under study. As in (6.27) the roots of the differences in the diagonal elements of the covariance matrices are then used as a measure for the contribution of this error, one difference divided by the sum of all defines the relative contribution of the associated error. Note that this is not strictly correct since the sum of the single differences will differ from the total systematic uncertainty as calculated by (6.27).

Figure 6.9 allows one to get an approximative feeling for the relative contributions of the systematic uncertainties, it shows that the error contributions differ for the various extracted polarisations. The main effect is caused by the yield fluctuations in the helium data, which affects the u_v polarisation less than the d_v and sea results, since the neutron asymmetries do not have as much impact on this quark polarisation as the hydrogen asymmetries. The remaining contributions divide up roughly to the same extent into experimental uncertainties originating from the polarisation measurements and uncertainties about the model assumptions used in the flavour decomposition. However, as seen in Figure 6.6, the systematic error is at all points much smaller than the statistical error, so that a more precise investigation of the model assumptions is not necessary. But this might change as soon as asymmetries with better precession will become available.

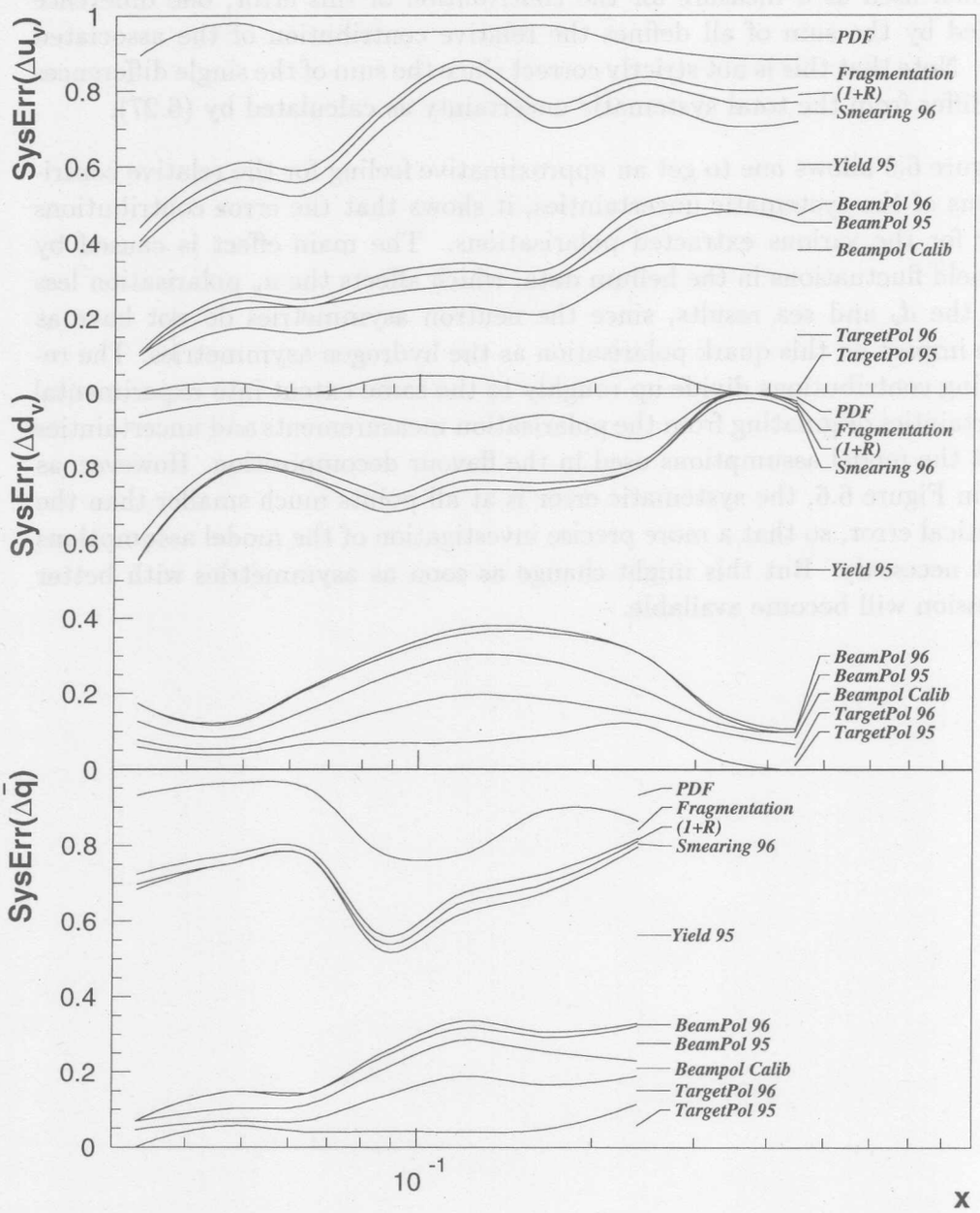

Figure 6.9: Composition of Systematic Errors. *For each flavour the areas in between the lines show the relative contributions of various systematic error sources adding up to one (see text).*

Chapter 7

Comparison to other Methods

After the purity method as described in Chapter 3.6 was applied to extract the polarised parton density distributions from the measured particle asymmetries, the results of this analysis as presented in the previous chapter will now be compared to the results of other measurements and expectations. In the first part an overview over other extraction methods and analyses is given, before in the second part predictions from more theoretical based considerations are presented.

7.1 Charge Asymmetries

The polarised parton distribution functions of valence quarks can be found by measuring the charge asymmetry of pions on at least two targets. From equations (3.2) and (3.4) the following expressions for the yields of charged pions on a proton target can be derived:

$$\begin{aligned} N_{\pi^+} &\propto (4u(x) + \bar{d}(x))D^+ + (d(x) + 4\bar{u}(x))D^- + (s(x) + \bar{s}(x))D_s, \\ N_{\pi^-} &\propto (d(x) + 4\bar{u}(x))D^+ + (4u(x) + \bar{d}(x))D^- + (s(x) + \bar{s}(x))D_s, \end{aligned} \tag{7.1}$$

with the same proportionality constant for both charges. Building the difference yields

$$N_{\pi^+-\pi^-} = N_{\pi^+} - N_{\pi^+} \tag{7.2}$$

$$\propto (4u_v(x) - d_v(x))(D^+ - D^-), \tag{7.3}$$

where we used (2.13) and (2.14). Obviously all sea contributions cancel in this expression. Now the spin asymmetry of the yield difference on the proton can

be expressed like

$$\begin{aligned} A_p^\pi(x) &= \frac{N^+_{\pi^+-\pi^-} - N^-_{\pi^+-\pi^-}}{N^+_{\pi^+-\pi^-} + N^-_{\pi^+-\pi^-}} \\ &= \frac{4\Delta u_v(x) - \Delta d_v(x)}{4u_v(x) - d_v(x)}, \end{aligned} \tag{7.4}$$

where $N^\pm_{\pi^+-\pi^-}$ denotes the yield difference for both spin configurations. Similar calculations yield

$$\begin{aligned} A_d^\pi(x) &= \frac{\Delta u_v(x) + \Delta d_v(x)}{u_v(x) + d_v(x)}, \\ A_{He}^\pi(x) &= \frac{-\Delta u_v(x) + 4\Delta d_v(x)}{7u_v(x) + 2d_v(x)}, \end{aligned} \tag{7.5}$$

for deuterium and ^{3}He targets.

By combining two targets the valence quark spin distributions can be isolated from (7.4) and (7.5). This kind of analysis was performed for 1995 and 1996 helium and hydrogen data in [Men97], however the high Čerenkov threshold in 1995 allows only the extraction of pion asymmetries with low statistics and together with the fact that the yield differences are of the order of a quarter of the single charge yields this results in a rather high uncertainty for the extracted polarised parton distributions. The method can be extended to hadron asymmetries by applying correction factors which are derived from Monte Carlo studies.

7.2 Monte Carlo Fit

The dataflow of the Monte Carlo fit method is shown in Figure 7.1. This technique is very similar to the purity method used in this analysis. The main difference is that relation between the measured particle asymmetries and the quark polarisations is no longer assumed to be linear[1] as in equation (3.14). Instead a polarised Monte Carlo is used to generate particle asymmetries for given quark polarisations. These asymmetries are then χ^2-compared to the measured asymmetries and the quark polarisations are varied by an optimisation algorithm until the minimum in χ^2 is found. The errors and correlations of the quark polarisations are extracted by fitting an ellipsoid to all points in

[1] In fact for a linear Monte Carlo the method is formally equivalent to the purity method [PTV95]. Non-linear effects (e.g. by breaking the factorisation theorem) are expected to be small.

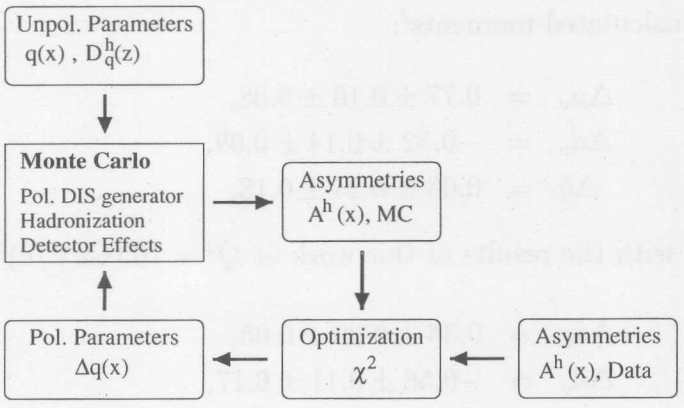

Figure 7.1: The Fit Extraction Method. *A polarised Monte Carlo uses fixed unpolarised parameters $q(x), D_q^h(z)$ as well as the polarised parameters $\Delta q(x)$ to be extracted to generate a set of asymmetries. This set is compared to the measured asymmetries and the polarised parameters are iteratively adjusted so that χ^2 reaches a minimum.*

the $(\Delta q, \chi^2)$-space that were generated during the optimisation process. The method needs enormous computing resources since for each optimisation step the asymmetries have to be generated with good accuracy. For realistic sample sizes careful convergence studies and checks of the extracted errors and correlations have to be done. The method was used in [Tal98] to extract quark polarisation, but unfortunately a mistake in the Monte Carlo generator for helium asymmetries was found after the publication, so a comparison of the results is not presented here.

7.3 SMC Results

The Spin Muon Collaboration (SMC, NA47) [SMC97a] used a 190 GeV polarised muon beam from the CERN SPS on a dynamic nuclear polarised solid target and took data in the years 1991-96. (Deuterated) Butanol and ammonia have been used as target materials. SMC had a spectrometer setup comparable to HERMES and was able to measure semi-inclusive hadron asymmetries. A method very similar to the analysis performed in this work was used to extract polarised quark distributions from these asymmetries using hadron fragmentation functions measured with the same setup [SMC98, Pre97]. The extracted polarised PDFs (at $Q^2 = 10$ $(\mathrm{GeV/c})^2$) are shown in Figure 6.6 and show slightly different features than the results of this work. While the polarisation of the u_v quarks is higher in the mid x region, the polarisations of the d_v quark is smaller and the sea contribution is compatible with zero. The same trend is

reflected in the calculated moments[2]:

$$\begin{aligned} \Delta u_v &= 0.77 \pm 0.10 \pm 0.08, \\ \Delta d_v &= -0.52 \pm 0.14 \pm 0.09, \\ \Delta \bar{q} &= 0.06 \pm 0.24 \pm 0.18, \end{aligned} \tag{7.6}$$

to be compared with the results of this work at $Q^2 = 10$ (GeV/c)^2:

$$\begin{aligned} \Delta u_v &= 0.36 \pm 0.09 \pm 0.05, \\ \Delta d_v &= -0.58 \pm 0.11 \pm 0.17, \\ \Delta \bar{q} &= 0.44 \pm 0.22 \pm 0.08. \end{aligned} \tag{7.7}$$

Again the SMC u_v contribution to the nucleon spin is higher, while the sea appears to be unpolarised. The results for d_v are compatible.

7.4 Non-Relativistic Quark Model

The non-relativistic quark model describes the ground state of the proton by the following totally symmetric combination of the $SU(6)$ $(= SU(3)_{Flavour} \times SU(2)_{Spin})$ parton wave functions [Nac86, PRS94]:

$$\begin{aligned} |p^\uparrow> \;=\; & \frac{1}{\sqrt{18}}(2|u^\uparrow u^\uparrow d^\downarrow> + 2|u^\uparrow d^\downarrow u^\uparrow> + 2|d^\downarrow u^\uparrow u^\uparrow> - |u^\uparrow d^\uparrow u^\downarrow> \\ & - |d^\uparrow d^\uparrow u^\downarrow> - |u^\downarrow u^\uparrow d^\uparrow> - |u^\downarrow d^\uparrow u^\uparrow> - |d^\uparrow d^\downarrow u^\uparrow>). \end{aligned} \tag{7.8}$$

The wave function of the neutron is obtained by exchange of u and d quarks. It is well known that the model describes with good accuracy the static magnetic properties of the nucleons. The operator for the magnetic moment is given by

$$\vec{\mu} \;=\; \vec{\mu}_u + \vec{\mu}_d \;=\; \mu_u \vec{\sigma}_u + \mu_d \vec{\sigma}_d, \tag{7.9}$$

where $\vec{\sigma}$ is the vector of Pauli matrices and μ_q is the magneton of a Dirac particle:

$$\mu_q = \frac{e_q e \hbar}{2 m_q}. \tag{7.10}$$

[2] As in Figure 6.6 the sea result from SMC was multiplied by 6 to give the total sea contribution as defined in (6.5).

in other words the Bjorken sum rule is not violated. On the other hand the isosinglet combination a_8 derived from the moments under the assumption of a flavour symmetric sea does not agree with a difference of 2.2σ. This discrepancy will be further discussed in Section 7.8.

7.6 Inclusive Data

It is possible to obtain information about the polarised parton distributions from inclusive measurements alone. In the this section it will be shown how the positivity limit can be used for such an analysis and how the flavour non-singlet distributions can be used to check the consistency of inclusive and semi-inclusive data. The section will be closed by a short remark about a combined QCD analysis of inclusive data and weak coupling constants.

7.6.1 Polarisation of Valence Quarks

It is possible to find limits for the polarised PDFs from inclusive data only [DF97]. From equation (2.21) one derives under the assumption of iso-spin symmetry:

$$\begin{aligned} g_1^p(x) + g_1^n(x) &= \frac{1}{2}\left(\frac{5}{9}\Delta u_v(x) + \frac{5}{9}\Delta d_v(x) + \frac{2}{9}\Delta\bar{q}(x)\right), \\ g_1^p(x) - g_1^n(x) &= \frac{1}{6}\left(\Delta u_v(x) - \Delta d_v(x)\right), \end{aligned} \tag{7.16}$$

where $\Delta\bar{q}(x)$ is defined as the sum of all sea contributions weighted by the squared quark charge averaged over both iso-spin states:

$$\Delta\bar{q}(x) = \frac{5}{2}\left(\Delta\bar{u}(x) + \Delta\bar{d}(x) + \Delta u_s(x) + \Delta d_s(x)\right) + \Delta s(x) + \Delta\bar{s}(x). \tag{7.17}$$

By inverting (7.16) the valence spin distributions can be extracted separately:

$$\begin{aligned} \Delta u_v &= \frac{24}{5}g_1^p(x) - \frac{6}{5}g_1^n(x) - \frac{1}{5}\Delta\bar{q}(x), \\ \Delta d_v &= -\frac{6}{5}g_1^p(x) + \frac{24}{5}g_1^n(x) - \frac{1}{5}\Delta\bar{q}(x). \end{aligned} \tag{7.18}$$

From the definitions (2.20) one obtains the positivity limit

$$|\Delta q(x)| \leq q(x), \tag{7.19}$$

For the magnetic moments of the proton and the neutron one obtains

$$\begin{aligned} \mu_p &= <p^\uparrow|\vec{\mu}|p^\uparrow> = \frac{4}{3}\mu_u - \frac{1}{3}\mu_d, \\ \mu_n &= <p^\uparrow|\vec{\mu}|p^\uparrow> = \frac{4}{3}\mu_d - \frac{1}{3}\mu_u, \end{aligned} \tag{7.11}$$

which leads (for $m_u = m_d$) to a ratio of

$$\frac{\mu_n}{\mu_p} = -\frac{2}{3}, \tag{7.12}$$

which is in very good agreement with the experimental value of -0.685. However, for the helicity contributions of the partons one obtains

$$\begin{aligned} \Delta u &= <p^\uparrow|\vec{\sigma}_u|p^\uparrow> = \frac{4}{3}, \\ \Delta d &= <p^\uparrow|\vec{\sigma}_d|p^\uparrow> = -\frac{1}{3}, \end{aligned} \tag{7.13}$$

which can only describe the sign of the moments of the polarised parton density functions, but not their measured values.

7.5 Baryon Decays

As already pointed out in Section 2.6.2, the $SU(3)$ flavour octet isotriplet and isosinglet combinations a_3 and a_8 of the first moments of the quark distributions are related to coupling constants measured in weak neutron decay. From Table 6.2 one derives (assuming $SU(3)$ flavour symmetric moments)

$$\begin{aligned} a_3 &= \Delta u_v - \Delta d_v = 1.01 \pm 0.10 \pm 0.11, \\ a_8 &= \Delta u_v + \Delta d_v = -0.19 \pm 0.19 \pm 0.23, \end{aligned} \tag{7.14}$$

where the correlations of the moments were considered for calculating the errors. These results have to be compared with the values from (2.35) corrected for QCD effects:

$$\begin{aligned} a_3 &= (F+D) \cdot C_1^{NS} = 1.102 \pm 0.003, \\ a_8 &= (3F-D) \cdot C_1^{S} = 0.51 \pm 0.02, \end{aligned} \tag{7.15}$$

where C_1^{NS} is defined in (2.37) and in leading order $C_1^S = C_1^{NS} = 0.877$ for $Q^2 = 2.3\ (\mathrm{GeV/c})^2$ and $\Lambda_0 = 0.25$ GeV/c.

Obviously the values for the non-singlet quantity a_3 are in good agreement,

for each flavour, which allows to put limits on $\Delta\bar{q}(x)$:

$$\begin{aligned} |\Delta\bar{q}(x)| &\leq |5\Delta\bar{u}(x)| + |5\Delta\bar{d}(x)| + |2\Delta s(x)| \\ &\leq 5\bar{u}(x) + 5\bar{d}(x) + 2s(x). \end{aligned} \tag{7.20}$$

The equations (7.18) for the quark spin distributions read now:

$$\begin{aligned} \Delta u_v &\in \frac{6}{5}\left(4g_1^p(x) - g_1^n(x)\right) \pm \left(\bar{u}(x) + \bar{d}(x) + \frac{2}{5}s(x)\right), \\ \Delta d_v &\in \frac{6}{5}\left(4g_1^n(x) - g_1^p(x)\right) \pm \left(\bar{u}(x) + \bar{d}(x) + \frac{2}{5}s(x)\right), \end{aligned} \tag{7.21}$$

where $a \in b \pm c$ means that a is limited according to $|a - b| \leq c$.

To summarise, the equations (7.21) show that the valence spin distributions can be derived from the inclusive spin structure functions, however only with an uncertainty which is given by the unpolarised quark sea distributions. Figure 7.2 shows the results for this procedure using the proton and neutron[3] from SLAC as shown in Figure 2.6.

7.6.2 Polarisation of Non-Singlet Distribution

The second line of (7.16) shows that the sea contribution to the difference of $g_1^p(x)$ and $g_1^n(x)$ (flavour non-singlet) is cancelling under the assumption of iso-spin symmetry. For this reason it is possible to derive the difference of the polarised valence quark distributions from inclusive data alone. Figure 7.3 shows the non-singlet part for SLAC data as well as for the preliminary HERMES data. Furthermore the results of the fit to the semi-inclusive asymmetries are drawn for comparison. The data shows good agreement within the statistical uncertainties.

[3]Since the g_1^n is actually computed from the difference of deuterium and proton data, g_1^n and g_1^p are highly correlated. Hence a modified version of (7.21) with the measured quantities g_1^p and g_1^d as input was used to produce Figure 7.2:

$$\begin{aligned} \Delta u_v &\in 6g_1^p(x) - \frac{12}{5}\frac{g_1^d(x)}{1+1.5\omega_D} \pm \left(\bar{u}(x) + \bar{d}(x) + \frac{2}{5}s(x)\right), \\ \Delta d_v &\in -6g_1^p(x) + \frac{48}{5}\frac{g_1^d(x)}{1+1.5\omega_D} \pm \left(\bar{u}(x) + \bar{d}(x) + \frac{2}{5}s(x)\right), \end{aligned}$$

where $\omega_D = 0.05 \pm 0.01$ is the D-wave state probability of the deuteron [SMC95].

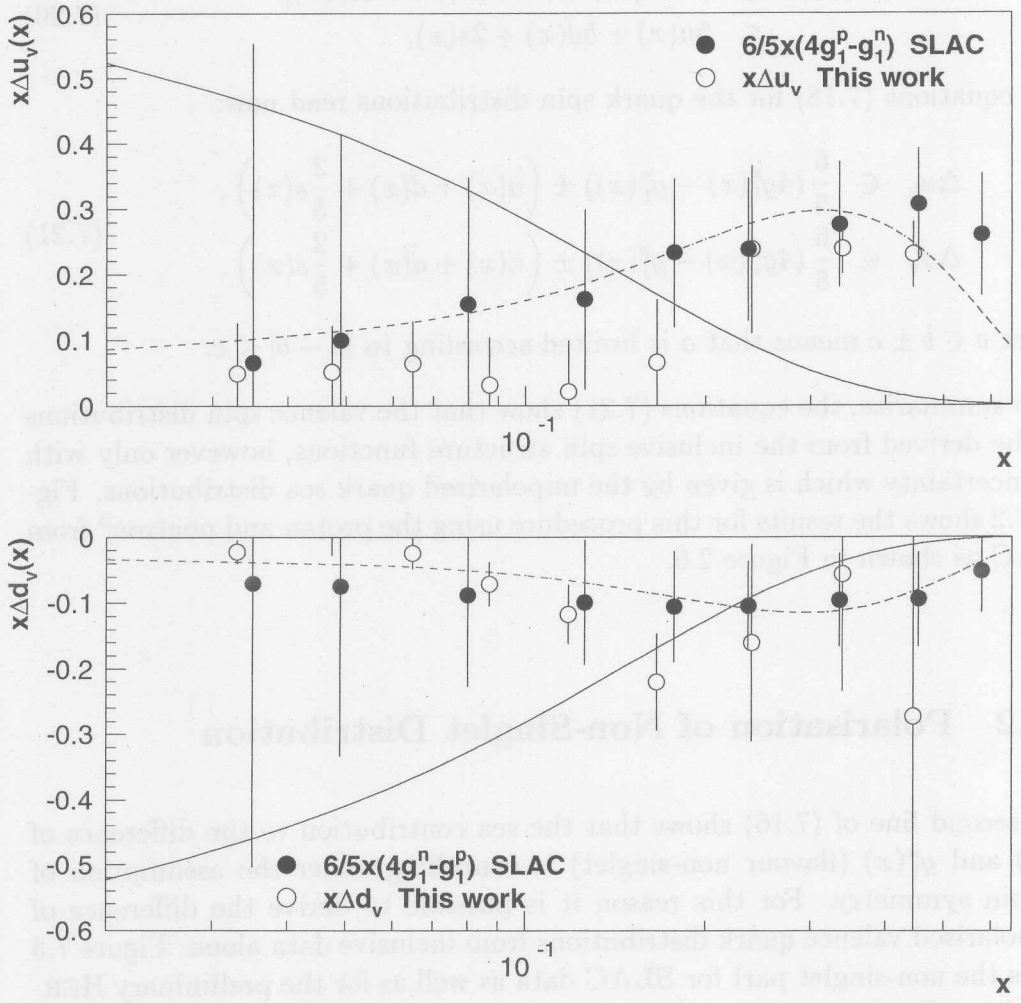

Figure 7.2: Valence Spin Distributions from Inclusive Data. *Solid points: the valence spin distribution $x\Delta u_v(x)$ and $x\Delta d_v(x)$ are derived from high precision inclusive spin structure functions of the proton and neutron as measured at* SLAC *(see Figure 2.6). The solid curves indicate the uncertainty due to the unknown quark sea polarisation – this maximum allowed range of fluctuation is calculated from the known unpolarised sea distributions [GRV95]. The dashed lines show the valence spin distribution as parametrised by [GRSV95]. The open points show the results of this work using inclusive and semi-inclusive asymmetries to fit the polarised quark distributions under the assumption of $SU(3)$-symmetric polarised sea PDFs (statistical errors only).*

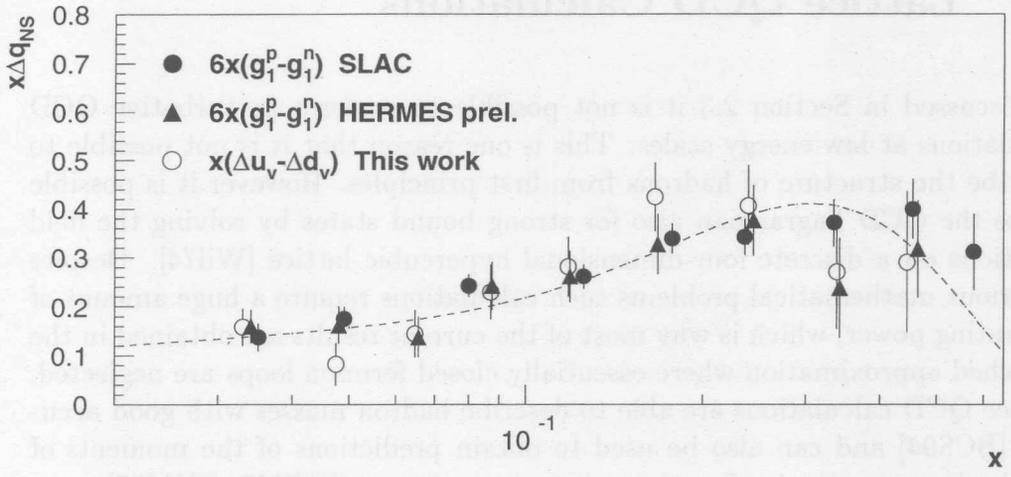

Figure 7.3: Non-singlet part of quark polarisations. *The triangles show the results as derived from preliminary* HERMES *data while the solid points show the same quantity from* SLAC *data (see Figure 2.6). The dashed line indicates the valence spin distribution as parametrised by [GRSV95]. The open points show the results of this work using inclusive and semi-inclusive asymmetries to fit the polarised quark distributions under the assumption of $SU(3)$-symmetric polarised sea PDFs (statistical errors only).*

7.6.3 QCD Analysis

In Section 7.5 the matrix elements F and D have been used to derive predictions for certain combinations of moments of the polarised parton density functions. A more sophisticated QCD analysis of the inclusive structure functions $g_1^p(x)$ and $g_1^n(x)$ together with F and D allows the fit of polarised PDFs as functions of x. The dotted lines in Figure 6.6 show the results of such an analysis as performed by [GRSV95]. Here the assumptions about the sea were $\Delta\bar{u}(x) = \Delta\bar{d}(x) = \Delta\bar{q}(x)$ and $\Delta s(x) = \Delta\bar{s}(x) = N_s\Delta\bar{q}(x)$, where $N_s \leq 1$ is an additional parameter of the fit that is found to be one. This kind of analysis is not a direct measurement of the polarised PDFs because their functional dependence on x has to be parametrised and it is not possible to extract valence quark distributions without assumptions about the sea polarisations. In contrast to that in the purity analysis these kinds of assumptions are only necessary because of the limited precision of the measured asymmetries. In principle they can be dropped as soon as data samples with increased statistics together with an improved particle identification are available.

7.7 Lattice QCD Calculations

As discussed in Section 2.3 it is not possible to perform perturbative QCD calculations at low energy scales. This is one reason that it is not possible to describe the structure of hadrons from first principles. However it is possible to use the QCD Lagrangian also for strong bound states by solving the field equations on a discrete four-dimensional hypercubic lattice [Wil74]. Despite of various mathematical problems such calculations require a huge amount of computing power, which is why most of the current results are obtained in the quenched approximation where essentially closed fermion loops are neglected. Lattice QCD calculations are able to describe hadron masses with good accuracy [BCS94] and can also be used to obtain predictions of the moments of polarised parton density functions. Latest results are [BGH97, GHM97]:

$$\begin{aligned} \Delta u_v &= 0.841(52), \\ \Delta d_v &= -0.245(15), \\ \Delta^{(1)} u_v &= 0.198(8), \\ \Delta^{(1)} d_v &= -0.0477(33), \end{aligned} \tag{7.22}$$

where $\Delta^{(1)} q$ denotes the second moment $M_2(q)$. The first moments are calculated for $Q^2 \approx 5$ (GeV/c)^2 while the second moments are given at $Q^2 \approx 2$ (GeV/c)^2. The corresponding numbers from this analysis are:

$$\begin{aligned} \Delta u_v &= 0.38 \pm 0.09 \pm 0.05, \\ \Delta d_v &= -0.59 \pm 0.11 \pm 0.17, \\ \Delta^{(1)} u_v &= 0.130 \pm 0.019 \pm 0.025, \\ \Delta^{(1)} d_v &= -0.076 \pm 0.029 \pm 0.027, \end{aligned} \tag{7.23}$$

where the features discussed in Section 7.3 appear again. The measured moments of the u_v quarks are lower than the lattice expectations, while the moments of d_v are measured to be more negative than calculated on the lattice.

7.8 Summary

The results from Chapter 6 have been compared to those of other measurements and expectations from theoretical calculations. The results indicate that the u_v quarks are carrying less helicity fraction of the nucleon as measured up to now. To compensate for that, the sea shows a slight positive polarisation. This phenomenon can be explained by the fact that the gluons that give rise

to the quark sea originate from the polarised valence quarks and are therefore polarised themselves. Hence one expects a polarisation transfer to the sea [CS77].

The most significant difference shows up in the comparison to predictions derived from baryon decays in Section 7.5. While the non-singlet quantity $\Delta u_v - \Delta d_v$ agrees well with the predicted value, the combination $\Delta u_v + \Delta d_v$ shows a deviation. As will be shown in the following, this might be caused by assuming $SU(3)$-symmetric polarised sea PDFs, which couples the light sea

$$\Delta\bar{q}_l = \Delta u_s + \Delta\bar{u} + \Delta d_s + \Delta\bar{d}, \tag{7.24}$$

and the strange sea $\Delta s + \Delta\bar{s}$. If this constraint is relaxed, the expression for a_3 in (7.14) is still true, while a_8 hast to be written as

$$a_8 = \Delta u_v + \Delta d_v + \Delta, \tag{7.25}$$

with $\Delta = \Delta\bar{q}_l - 2(\Delta s + \Delta\bar{s})$. Unfortunately the values for Δu_v and Δd_v from Table 6.2 can not be used to calculate Δ (and subsequently Δs), since they were retrieved under the incompatible assumption (6.5) about sea polarisations. To overcome this situation, a four-parameter fit had to be performed to extract a new set of quark asymmetries $\{\Delta u_v, \Delta d_v, \Delta\bar{q}_l, \Delta s = \Delta\bar{s}\}$. Due to statistical limitations from the hadron asymmetries the results of such an analysis are no longer significant. However, they indicate a positive polarisation of the light sea while the strange sea tends to become negative. This points into the same direction as results from extracting the flavour momenta by combining the inclusive first momenta $\Gamma_1^{p,n}$ with the weak matrix elements (2.35) using equations (2.33) and (2.34). Considering QCD corrections, one obtains at $Q^2 = 10\ (\mathrm{GeV/c})^2$ [EK95]:

$$\begin{aligned} \Delta u + \Delta\bar{u} &= 0.83 \pm 0.03, \\ \Delta d + \Delta\bar{d} &= -0.43 \pm 0.03, \\ \Delta s + \Delta\bar{s} &= -0.10 \pm 0.03. \end{aligned} \tag{7.26}$$

As a final remark it should be noted (as already pointed out in Section 6.5.1) that the measured hadron asymmetries are also compatible with the assumption of a totally unpolarised sea.

Chapter 8

Conclusion and Outlook

Since its commissioning in 1995 the HERMES experiment successfully took polarised semi-inclusive data using the new experimental technique of a polarised internal gas target. As a modern experiment HERMES also makes use of advanced software technologies. Part of this work was the implementation, test and maintenence of major software modules that are used both online, to run the experiment and offline, to analyse the data. An overview about the most important of these modules is given in Appendix C.

In the first part of this thesis, the inclusive and semi-inclusive (pion and hadron) spin asymmetries have been extracted from 1995 and 1996 data sets taken on polarised ^{3}He and hydrogen targets respectively.

The hadron and inclusive asymmetries have then been used to extract a set of polarised parton density functions of the nucleon for different assumptions about the sea polarisation. This analysis was performed by using unpolarised quantities called purities which are derived from unpolarised PDFs and fragmentation functions. Assuming $SU(3)$-symmetrical polarised sea PDFs, the first moment have been measured to be $\Delta u_v = 0.41 \pm 0.09 \pm 0.06$, $\Delta d_v = -0.60 \pm 0.12 \pm 0.17$ and $\Delta \bar{q} = 0.45 \pm 0.22 \pm 0.08$ at $Q^2 = 2.3$ (GeV/c)^2. Already at this point the precision of the results is comparable to the only other existing semi-inclusive measurement from SMC.

Using the asymmetries from 1995 and 1996 the spin flavour decomposition was only possible with rather strong symmetry assumptions for the polarisations of the various sea contributions. As pointed out in Section 7.8 it is desirable to relax this condition for a better understanding of the spin structure of the nucleon. The main obstacle for such an analysis is the statistical precision of the ^{3}He asymmetries, which is small compared to the accuracy of

the hydrogen data when the 1996 and 97 data sets are combined. For this reason the data taking on a polarised deuterium target is scheduled for the next two years to increase the sensitivity to the d_v and sea polarisations. In addition HERMES will be able to perform a complete hadron identification over the full accepted momentum region by converting the threshold Čerenkov counter into a RICH. Therefore one can look forward decreasing drastically the uncertainties on the results of analyses such as the one introduced in this work. We will then be able to resolve the quark spin structure of the nucleon by direct semi-inclusive measurements to a much better extent.

Appendix A

Formalism of the Analysis

In this appendix the most important parts of the analysis formalism are collected for quick reference.

A.1 Errors and Covariances of Particle Numbers

Of course the observed scattered positrons are Poisson-distributed and hence their variance $\sigma^2_{N_{e+}}$ equals their number N_{e+}. However this is not the case for the number of detected hadrons N^h as will be shown in the following [Pre97]. We define M as number of incoming positrons, p as the probability that a positron was scattered and n^h as the number of hadrons h per event. Furthermore the indexed variables $p_i \in \{0,1\}$ and $n^h_i \in \{0,1,2,\ldots\}$ are used to denote random variables.

For an introduction, the well-known error on N_{e+} is calculated:

$$\begin{aligned}
\sigma^2_{N_{e+}} &= < N^2_{e+} > - < N_{e+} >^2 \;=\; < \sum_{i,j} p_i p_j > - < \sum_i p_i >^2 \\
&= < \sum_i p_i^2 > + < \sum_{i \neq j} p_i p_j > - < \sum_i p_i >^2 \\
&= M < p_i^2 > + M(M-1) < p_i >^2 - M^2 < p_i >^2 \\
&= N_{e+}
\end{aligned} \tag{A.1}$$

Here the usual Poisson approximation of $Mp^2 = 0$ and the relation $< p_i^2 >=< p_i >= p$ were used. For the errors on N_h one obtains:

$$\begin{aligned}
\sigma^2_{N_h} &= < N_h^2 > - < N_h >^2 = < \sum_{i,j} p_i n_i^h p_j n_j^h > - < \sum_i p_i n_i^h >^2 \\
&= < \sum_i p_i^2 (n_i^h)^2 > + < \sum_{i \neq j} p_i n_i^h p_j n_j^h > - < \sum_i p_i n_i^h >^2 \\
&= M < p_i^2 >< (n_i^h)^2 > + M(M-1) < p_i >^2 < n_i^h >^2 - \\
&\quad M^2 < p_i >^2 < n_i^h >^2 \\
&= N_{e^+} < (n_i^h)^2 > = N_h \frac{< (n_i^h)^2 >}{< n_i^h >},
\end{aligned} \tag{A.2}$$

which is different from the value N_h that we would get for a Poisson distribution.

Using the same technique the statistical covariances for the numbers of measured particles can be calculated:

$$\begin{aligned}
cov(N_{h_1}, N_{h_2}) &= < N_{h_1} N_{h_2} > - < N_{h_1} >< N_{h_2} > \\
&= < \sum_i p_i^2 n_i^{h_1} n_i^{h_2} > + < \sum_{i \neq j} p_i n_i^{h_1} p_j n_j^{h_2} > - \\
&\quad < \sum_i p_i n_i^{h_1} >< \sum_i p_i n_i^{h_2} > \\
&= M < p_i^2 >< n_i^{h_1} n_i^{h_2} > + \\
&\quad M(M-1) < p_i >^2 < n_i^{h_1} >< n_i^{h_2} > - \\
&\quad M^2 < p_i >^2 < n_i^{h_1} >< n_i^{h_2} > \\
&= N_{e^+} < n_i^{h_1} n_i^{h_2} >; \\
cov(N_{e^+}, N_h) &= N_{e^+} n^h.
\end{aligned} \tag{A.3}$$

where $n_i^{e^+} = 1$ was used. Finally we find for the correlation coefficients of the particle numbers:

$$\begin{aligned}
cor(N_{h_1}, N_{h_2}) &= \frac{cov(N_{h_1}, N_{h_2})}{\sigma_{h_1} \sigma_{h_2}} \\
&= \frac{< n_i^{h_1} n_i^{h_2} >}{\sqrt{< (n_i^{h_1})^2 >< (n_i^{h_2})^2 >}}; \\
cor(N_{e^+}, N_h) &= \frac{n_i^h}{\sqrt{< (n_i^h)^2 >}}.
\end{aligned} \tag{A.4}$$

A.2 Errors and Covariances of Asymmetries

For convenience we rewrite (5.2) as

$$A = \frac{N^+L^- - N^-L^+}{N^+\overline{D}^-P^- + N^-\overline{D}^+P^+} =: \frac{Nom}{Denom} \tag{A.5}$$

using

$$\begin{aligned} L^{+(-)} &= \int_{+(-)} \mathcal{L}(t)dt, \\ P^{+(-)} &= \int_{+(-)} \mathcal{L}(t)p_T(t)p_B(t)dt. \end{aligned} \tag{A.6}$$

Then the statistical error on the asymmetry is[1]

$$\begin{aligned} (\Delta A)^2 = &\left[\Delta N^+ \left(\frac{L^-}{Denom} - \frac{\overline{D}^-P^-Nom}{Denom^2}\right)\right]^2 + \\ &\left[\Delta N^- \left(\frac{L^+}{Denom} + \frac{\overline{D}^+P^+Nom}{Denom^2}\right)\right]^2. \end{aligned} \tag{A.7}$$

The covariance matrix of the asymmetries is given by the transformation

$$\mathcal{C}_A = \frac{\partial \boldsymbol{A}}{\partial \boldsymbol{N}} \mathcal{C}_N \left(\frac{\partial \boldsymbol{A}}{\partial \boldsymbol{N}}\right)^T, \tag{A.8}$$

or in components

$$\begin{aligned} cov(A_i, A_j) &= \sum_{\mu,\nu} \frac{\partial A_i}{\partial N_\mu} \frac{\partial A_j}{\partial N_\nu} cov(N_\mu, N_\nu) \\ &= \frac{\partial A_i}{\partial N_{i+}} \frac{\partial A_j}{\partial N_{j+}} cov(N_{i+}, N_{j+}) + \frac{\partial A_i}{\partial N_{i-}} \frac{\partial A_j}{\partial N_{j-}} cov(N_{i-}, N_{j-}) \\ &\approx \frac{1}{2}\left[\frac{\partial A_i}{\partial N_{i+}} \frac{\partial A_j}{\partial N_{j+}} + \frac{\partial A_i}{\partial N_{i-}} \frac{\partial A_j}{\partial N_{j-}}\right] cov(N_i, N_j) \\ &\approx \frac{\partial A_i}{\partial N_{i\pm}} \frac{\partial A_j}{\partial N_{j\pm}} cov(N_i, N_j), \end{aligned} \tag{A.9}$$

where greek indices run over both spin states. Here we made use of the fact that an asymmetry A_i for a given particle type only depends on the count rates

[1] This is an approximation for the case $|a| \not\approx 1$. If the asymmetry is close to ± 1 one cannot assume a Gaussian distribution any more.

for this particle in both spin states (denoted as N_{i+} and N_{i-}) and that the two spin states are statistically uncorrelated ($cov(N_{i+}, N_{i-}) = 0$). Furthermore the approximations $N_{i\pm} \approx 1/2 N_i$ and $|\frac{\partial A_i}{\partial N_{i+}}| \approx |\frac{\partial A_i}{\partial N_{i-}}|$ were used. Under the same assumptions the errors on the asymmetries become $\sigma^2_{A_i} = \left(\frac{\partial A_i}{\partial N_{i\pm}}\right)^2 \sigma^2_{N_i}$ and hence

$$cov(A_i, A_j) \approx \frac{\sigma_{A_i}\sigma_{A_j}}{\sigma_{N_i}\sigma_{N_j}} cov(N_i, N_j), \tag{A.10}$$

or for the correlation coefficients

$$cor(\boldsymbol{A}) \approx cor(\boldsymbol{N}). \tag{A.11}$$

A.3 Singular Value Decomposition

For calculating the quark polarisations from the hadron asymmetries, one needs to solve equation (3.14). In general this system can be overdetermined since one might have measured more hadron asymmetries than quarks that one is interested in. If we denote the m measured asymmetries with $A_r = A^{h_r}$ and the n quark asymmetries with $Q_i = \Delta q_i / q_i$ then we want to choose $\boldsymbol{Q}$ in a way that

$$\begin{aligned} \chi^2 &= \sum_{R=1}^{m} \left(\boldsymbol{A}_r - \sum_{i=1}^{n} \boldsymbol{\mathcal{P}}_{ri} \boldsymbol{Q}_i \right)^2 \\ &= (\boldsymbol{A} - \boldsymbol{\mathcal{P}}\boldsymbol{Q})^T (\boldsymbol{A} - \boldsymbol{\mathcal{P}}\boldsymbol{Q}), \end{aligned} \tag{A.12}$$

becomes minimal. A standard method to do this is to differentiate (A.12) with respect to each $\boldsymbol{Q}_i$ and equating to zero, which results in the *normal equation*

$$\boldsymbol{\mathcal{P}}^T \boldsymbol{A} = (\boldsymbol{P}^T \boldsymbol{P}) \boldsymbol{Q}, \tag{A.13}$$

which leads to the formal solution

$$\boldsymbol{Q} = (\boldsymbol{P}^T \boldsymbol{P})^{-1} \boldsymbol{\mathcal{P}}^T \boldsymbol{A}. \tag{A.14}$$

Instead of evaluating this equation, there is a nice method called *singular value decomposition* (SVD) [PTV95] which makes use of the theorem, that any $m \times n$ matrix $\boldsymbol{\mathcal{P}}$ can be written as a product of an $m \times n$ column-orthogonal matrix $\boldsymbol{U}$, an $n \times n$ diagonal matrix $\boldsymbol{\mathcal{W}}$ with positive or zero elements (the *singular values*), and the transpose of a $n \times n$ orthogonal matrix $\boldsymbol{\mathcal{V}}$

$$\boldsymbol{\mathcal{P}}_{ij} = \sum_{k=1}^{n} \boldsymbol{\mathcal{U}}_{ik} \boldsymbol{W}_k \boldsymbol{\mathcal{V}}_{jk}, \tag{A.15}$$

where the diagonal of $\mathcal{W}$ is denoted by the vector $\boldsymbol{W}$. One can show that

$$\boldsymbol{Q} = \mathcal{V}[diag(1/\boldsymbol{W}_j)](\mathcal{U}^T\boldsymbol{A}) \tag{A.16}$$

minimises $\|\mathcal{P}\boldsymbol{Q} - \boldsymbol{A}\|$ and hence solves (3.14).

If one now takes into account the covariances between the measured asymmetries, one has to minimise χ^2 as defined in equation (6.4) at the beginning of Chapter 6. Since the covariance matrix $\mathcal{C}_A$ is symmetric and positive semi-definite one can apply the Cholesky decomposition

$$\mathcal{C}_A^{-1} = \mathcal{L}^T\mathcal{L}, \tag{A.17}$$

where $\mathcal{L}$ is a triangular matrix. With $\boldsymbol{A'} = \mathcal{L}\boldsymbol{A}$ and $\mathcal{P'} = \mathcal{L}\mathcal{P}$ equation (6.4) becomes again of the form (A.12):

$$\chi^2 = (\boldsymbol{A'} - \mathcal{P'}\boldsymbol{Q})^T(\boldsymbol{A'} - \mathcal{P'}\boldsymbol{Q}), \tag{A.18}$$

and we can find the optimal solution by (A.16).

Now the covariances between the extracted quark asymmetries $\boldsymbol{Q}$ can be estimated. From $Cov(\mathcal{M}\boldsymbol{x}) = \mathcal{M}Cov(\boldsymbol{x})\mathcal{M}^T$ follows

$$\begin{aligned} \mathcal{C}_Q &= \mathcal{P}^{-1}\mathcal{C}_A(\mathcal{P}^T)^{-1} \\ &= (\mathcal{P}^T\mathcal{C}_A^{-1}\mathcal{P})^{-1} \\ &= (\mathcal{P}^T\mathcal{L}^T\mathcal{L}\mathcal{P})^{-1} \\ &= \mathcal{P'}^{-1}(\mathcal{P'}^T)^{-1} \\ &= \mathcal{P'}^{-1}(\mathcal{P'}^{-1})^T, \end{aligned} \tag{A.19}$$

and finally with (A.16) and $\mathcal{U'}^T\mathcal{U'} = 1$

$$[\mathcal{C}_Q]_{ij} = \sum_{k=1}^{n} \frac{\mathcal{V'}_{ik}\mathcal{V'}_{jk}}{\boldsymbol{W'}_k}, \tag{A.20}$$

where $\mathcal{U'}$, $\mathcal{V'}$ and $\boldsymbol{W'}$ are the singular value components of $\mathcal{P'}$.

A.4 Fitting Functions to binned Data

In Section 6.5.2 we need to fit a parametrised model function $f(x)$ to data that is measured in bins F_i. This is often done by directly using the measured values at defined value of $\bar{x}_i$ as input to the fit neglecting the fact that there is actually no exact definition for $\bar{x}_i$. For a bin covering the interval $[x_i^l, x_i^h]$

common choices for $\bar{x}_i$ are the centre of the bin $(x_i^l + x_i^h)/2$ or the "centre of gravity" defined by

$$\bar{x}_i = \frac{1}{N} \int_{x_i^l}^{x_i^h} n(x)\, dx, \tag{A.21}$$

where $n(x)$ is the population density of the bins which either follows from physical principles or has to be measured separately and N is defined as the total population of the bin

$$N = \int_{x_i^l}^{x_i^h} n(x)\, dx. \tag{A.22}$$

Both choices of $\bar{x}_i$ fail in case $n(x)$ is not (approximately) constant over a bin[2]. In this case the measured values are given by the folding of the function $f(x)$ and the density function over the bin

$$F_i = \frac{1}{N} \int_{x_i^l}^{x_i^h} f(x) \cdot n(x)\, dx. \tag{A.23}$$

In a fit procedure one has to calculate this integral (and not simply $f(x)$) in each sampling step and compare it to the measured values.

For the calculation of moments (2.30) of the function $f(x)$ the same complications appear. In general it is not exact to calculate the moments of the measured region as

$$M_n^{meas,sum}(f) = \sum_i \bar{x}_i^{n-1}\, F_i\, (x_i^h - x_i^l). \tag{A.24}$$

To correct for the non-uniform bin population, one rather calculates

$$M_n^{meas,fit}(f) = \sum_i \frac{\int_{x_i^l}^{x_i^h} x^{n-1} f(x) dx}{\frac{1}{N} \int_{x_i^l}^{x_i^h} f(x) n(x) dx}\, F_i, \tag{A.25}$$

where one uses a fitted form of $f(x)$. This means that in the general case it is not even for the measured region possible to calculate moments without assuming a model function $f(x)$ and the knowledge of the population density $n(x)$.

[2] In our application this is for instance the case for the highest x-bin, where $\bar{x}_i \ll (x_i^l + x_i^h)/2$ due to a large bin width and the rapid decrease of the cross-section with x

Appendix B

Tables of Results

Bin	x	N_{evt}	D	Q^2	x	$z_{\pi+}$	$z_{\pi-}$	z_{h+}	z_{h-}
1	0.023-0.040	68404	0.727	1.218	0.033	0.360	0.355	0.362	0.349
2	0.040-0.055	76614	0.597	1.481	0.047	0.426	0.414	0.389	0.372
3	0.055-0.075	88486	0.503	1.730	0.065	0.471	0.457	0.404	0.386
4	0.075-0.100	87819	0.427	1.996	0.087	0.493	0.482	0.413	0.395
5	0.100-0.140	95753	0.377	2.395	0.118	0.509	0.497	0.412	0.394
6	0.140-0.200	70712	0.367	3.198	0.166	0.517	0.501	0.406	0.388
7	0.200-0.300	42704	0.378	4.551	0.239	0.529	0.507	0.400	0.379
8	0.300-0.400	11422	0.400	6.564	0.339	0.537	0.497	0.390	0.376
9	0.400-0.600	2813	0.438	9.183	0.446	0.549	0.540	0.371	0.368

Bin	x	N_{evt}	D	Q^2	x	$z_{\pi+}$	$z_{\pi-}$	z_{h+}	z_{h-}
1	0.023-0.040	204973	0.723	1.215	0.033	0.486	0.484	0.364	0.353
2	0.040-0.055	236076	0.591	1.470	0.047	0.562	0.559	0.390	0.381
3	0.055-0.075	278357	0.498	1.716	0.065	0.595	0.595	0.405	0.395
4	0.075-0.100	279542	0.422	1.979	0.087	0.615	0.606	0.413	0.402
5	0.100-0.140	303967	0.375	2.383	0.118	0.624	0.617	0.415	0.402
6	0.140-0.200	224632	0.366	3.185	0.166	0.639	0.629	0.411	0.395
7	0.200-0.300	130945	0.376	4.525	0.239	0.650	0.636	0.405	0.384
8	0.300-0.400	33475	0.399	6.524	0.338	0.672	0.647	0.396	0.374
9	0.400-0.600	7920	0.436	9.124	0.444	0.690	0.649	0.386	0.378

Table B.1: Kinematical Bins for Hydrogen (top) and ^{3}He (bottom). *For each bin the range in x, the number of reconstructed events with a DIS-positron together with the mean values for the depolarisation factor and the inclusive and hadronic kinematical variables are shown. The numbers are extracted from experimental data and are averaged over both spin states.*

Bin	$n_{\pi+}$	$\frac{<N^2_{\pi+}>}{n_{\pi+}}$	$n_{\pi-}$	$\frac{<N^2_{\pi-}>}{n_{\pi-}}$	n_{h+}	$\frac{<N^2_{h+}>}{n_{h+}}$	n_{h-}	$\frac{<N^2_{h-}>}{n_{h-}}$	n_{e-}
1	0.088	1.044	0.070	1.036	0.142	1.070	0.098	1.048	0.011
2	0.088	1.033	0.066	1.026	0.174	1.064	0.113	1.043	0.009
3	0.080	1.026	0.058	1.021	0.179	1.061	0.110	1.041	0.007
4	0.067	1.025	0.044	1.022	0.169	1.056	0.095	1.035	0.006
5	0.053	1.022	0.035	1.014	0.156	1.055	0.083	1.028	0.005
6	0.046	1.015	0.027	1.014	0.151	1.056	0.071	1.024	0.004
7	0.038	1.016	0.022	1.002	0.137	1.049	0.064	1.022	0.003
8	0.032	1.017	0.018	1.010	0.124	1.045	0.052	1.017	0.002
9	0.027	1.027	0.013	1.000	0.116	1.055	0.049	1.014	0.003

Bin	$n_{\pi+}$	$\frac{<N^2_{\pi+}>}{n_{\pi+}}$	$n_{\pi-}$	$\frac{<N^2_{\pi-}>}{n_{\pi-}}$	n_{h+}	$\frac{<N^2_{h+}>}{n_{h+}}$	n_{h-}	$\frac{<N^2_{h-}>}{n_{h-}}$	n_{e-}
1	0.043	1.010	0.035	1.006	0.143	1.061	0.106	1.046	0.005
2	0.042	1.005	0.033	1.002	0.173	1.058	0.119	1.042	0.004
3	0.036	1.004	0.026	1.004	0.175	1.056	0.114	1.040	0.003
4	0.028	1.003	0.019	1.003	0.161	1.053	0.100	1.033	0.002
5	0.022	1.003	0.014	1.004	0.145	1.051	0.085	1.029	0.002
6	0.018	1.002	0.011	1.002	0.135	1.048	0.074	1.027	0.001
7	0.014	1.001	0.008	1.004	0.122	1.040	0.062	1.025	0.001
8	0.012	1.005	0.006	1.000	0.109	1.042	0.051	1.016	0.001
9	0.012	1.000	0.006	1.000	0.109	1.030	0.046	1.011	0.000

Table B.2: Single Particle Multiplicities for hydrogen (top) and ^{3}He (bottom). *These numbers are extracted from experimental data and are averaged over both spin states.*

Bin	Cor (π^+,π^-)	Cor (h^+,h^-)	Cor (e^+,π^+)	Cor (e^+,π^-)	Cor (e^+,h^+)	Cor (e^+,h^-)
1	0.098	0.129	0.290	0.259	0.364	0.306
2	0.078	0.135	0.291	0.255	0.405	0.328
3	0.066	0.132	0.279	0.238	0.411	0.326
4	0.055	0.116	0.255	0.207	0.400	0.303
5	0.050	0.102	0.227	0.184	0.384	0.285
6	0.040	0.090	0.213	0.163	0.378	0.264
7	0.031	0.079	0.194	0.148	0.362	0.250
8	0.015	0.054	0.176	0.133	0.344	0.227
9	0.000	0.037	0.161	0.115	0.331	0.220

Bin	Cor (π^+,π^-)	Cor (h^+,h^-)	Cor (e^+,π^+)	Cor (e^+,π^-)	Cor (e^+,h^+)	Cor (e^+,h^-)
1	0.025	0.125	0.207	0.187	0.367	0.319
2	0.017	0.131	0.205	0.180	0.404	0.339
3	0.014	0.124	0.189	0.161	0.407	0.332
4	0.014	0.113	0.167	0.139	0.391	0.311
5	0.011	0.099	0.148	0.119	0.372	0.287
6	0.006	0.088	0.135	0.104	0.359	0.269
7	0.006	0.072	0.120	0.089	0.342	0.246
8	0.004	0.047	0.108	0.076	0.324	0.224
9	0.000	0.035	0.109	0.079	0.325	0.213

Table B.3: Correlations of Particle Numbers for hydrogen (top) and ^{3}He (bottom). *These numbers are extracted from experimental data and are averaged over both spin states.*

Bin	$A_{\pi+}$	$A_{\pi-}$	A_{h+}	A_{h-}	A_{e+}
1	0.114±0.042	0.098±0.047	0.113±0.035	0.106±0.041	0.076±0.012
2	0.096±0.047	0.032±0.053	0.095±0.036	0.063±0.043	0.089±0.014
3	0.108±0.051	0.095±0.058	0.118±0.038	0.089±0.047	0.105±0.015
4	0.333±0.060	0.224±0.074	0.232±0.044	0.233±0.057	0.179±0.019
5	0.136±0.066	0.200±0.082	0.218±0.047	0.262±0.062	0.223±0.020
6	0.326±0.084	0.234±0.108	0.286±0.057	0.317±0.079	0.273±0.025
7	0.430±0.124	0.488±0.159	0.537±0.079	0.337±0.111	0.372±0.032
8	0.270±0.258	0.025±0.337	0.262±0.153	0.262±0.224	0.441±0.057
9	1.013±0.581	1.845±0.823	0.834±0.317	0.403±0.475	0.593±0.109

Bin	$A_{\pi+}$	$A_{\pi-}$	A_{h+}	A_{h-}	A_{e+}
1	0.081±0.059	−0.172±0.065	−0.055±0.035	−0.077±0.040	−0.032±0.012
2	0.006±0.065	0.105±0.074	−0.008±0.036	0.027±0.042	−0.000±0.014
3	0.068±0.070	0.019±0.082	−0.030±0.037	−0.019±0.045	−0.018±0.015
4	−0.152±0.081	−0.073±0.097	−0.045±0.042	0.005±0.052	−0.024±0.018
5	0.027±0.088	−0.113±0.110	0.013±0.045	0.035±0.057	−0.031±0.019
6	−0.075±0.114	0.165±0.146	0.009±0.055	−0.014±0.071	−0.065±0.023
7	0.095±0.168	0.176±0.225	−0.137±0.074	0.076±0.100	−0.034±0.029
8	−0.110±0.375	−1.048±0.535	−0.069±0.152	−0.068±0.217	0.008±0.054
9	0.166±0.789	0.766±1.065	−0.241±0.296	1.303±0.443	0.027±0.102

Table B.4: Measured Asymmetries for hydrogen (top) and ^{3}He (bottom). *The hydrogen asyemmetries and errors are corrected for kinematical smearing (see Figure 5.2). Statistical errors only.*

	Polarisations			Correlations			Statistics	
Bin	$\Delta u_v/u_v$	$\Delta d_v/d_v$	$\Delta\bar{q}/\bar{q}$	$(\frac{\Delta u_v}{u_v}, \frac{\Delta d_v}{d_v})$	$(\frac{\Delta u_v}{u_v}, \frac{\Delta \bar{q}}{\bar{q}})$	$(\frac{\Delta d_v}{d_v}, \frac{\Delta \bar{q}}{\bar{q}})$	$\chi^2_{min}/3$	$CL(\chi^2_{min}, 3)$
1	$0.195_{\pm 0.264 \pm 0.0385}$	$-0.667_{\pm 0.597 \pm 0.147}$	$0.0445_{\pm 0.19 \pm 0.0284}$	0.884	-0.985	-0.939	1.48	0.217
2	$0.147_{\pm 0.199 \pm 0.0308}$	$-0.193_{\pm 0.492 \pm 0.127}$	$0.0446_{\pm 0.188 \pm 0.0289}$	0.845	-0.977	-0.921	0.123	0.946
3	$0.167_{\pm 0.16 \pm 0.0254}$	$-0.393_{\pm 0.441 \pm 0.122}$	$0.0656_{\pm 0.203 \pm 0.0322}$	0.815	-0.968	-0.912	0.0632	0.979
4	$0.0918_{\pm 0.152 \pm 0.024}$	$-0.921_{\pm 0.465 \pm 0.141}$	$0.378_{\pm 0.265 \pm 0.0506}$	0.804	-0.958	-0.914	0.925	0.428
5	$0.0736_{\pm 0.141 \pm 0.0222}$	$-1.19_{\pm 0.489 \pm 0.153}$	$0.689_{\pm 0.368 \pm 0.0781}$	0.813	-0.952	-0.926	0.911	0.435
6	$0.174_{\pm 0.151 \pm 0.0295}$	$-1.52_{\pm 0.638 \pm 0.197}$	$1.01_{\pm 0.697 \pm 0.149}$	0.836	-0.952	-0.942	1.23	0.295
7	$0.349_{\pm 0.198 \pm 0.052}$	$-1.07_{\pm 1.06 \pm 0.276}$	$1.02_{\pm 1.93 \pm 0.393}$	0.886	-0.960	-0.965	2.1	0.0974
8	$0.523_{\pm 0.354 \pm 0.0708}$	$0.267_{\pm 2.51 \pm 0.58}$	$-1.46_{\pm 8.31 \pm 1.53}$	0.914	-0.971	-0.975	0.843	0.47
9	$-0.239_{\pm 0.886 \pm 0.178}$	$-7.74_{\pm 7.1 \pm 1.63}$	$44.5_{\pm 43.9 \pm 8.77}$	0.953	-0.986	-0.985	2.79	0.0388

Table B.5: Extracted Quark Polarisations for Polarisation-symmetric Sea.

	Polarisations			Correlations			Statistics	
Bin	$\Delta u_v/u_v$	$\Delta d_v/d_v$	$\Delta\bar{q}/\bar{q}$	$(\frac{\Delta u_v}{u_v}, \frac{\Delta d_v}{d_v})$	$(\frac{\Delta u_v}{u_v}, \frac{\Delta \bar{q}}{\bar{q}})$	$(\frac{\Delta d_v}{d_v}, \frac{\Delta \bar{q}}{\bar{q}})$	$\chi^2_{min}/3$	$CL(\chi^2_{min}, 3)$
1	$0.178_{\pm 0.277 \pm 0.0352}$	$-0.683_{\pm 0.549 \pm 0.138}$	$0.0632_{\pm 0.219 \pm 0.0293}$	0.872	-0.986	-0.928	1.47	0.22
2	$0.154_{\pm 0.207 \pm 0.0279}$	$-0.161_{\pm 0.438 \pm 0.117}$	$0.041_{\pm 0.211 \pm 0.0282}$	0.821	-0.979	-0.900	0.13	0.942
3	$0.161_{\pm 0.163 \pm 0.0215}$	$-0.378_{\pm 0.374 \pm 0.11}$	$0.0761_{\pm 0.217 \pm 0.0291}$	0.771	-0.969	-0.877	0.0566	0.982
4	$0.0694_{\pm 0.158 \pm 0.0183}$	$-0.822_{\pm 0.383 \pm 0.123}$	$0.422_{\pm 0.278 \pm 0.0466}$	0.753	-0.961	-0.872	0.829	0.478
5	$0.0404_{\pm 0.15 \pm 0.0158}$	$-0.998_{\pm 0.378 \pm 0.127}$	$0.734_{\pm 0.369 \pm 0.0694}$	0.753	-0.957	-0.874	0.736	0.53
6	$0.114_{\pm 0.163 \pm 0.0201}$	$-1.33_{\pm 0.447 \pm 0.153}$	$1.12_{\pm 0.647 \pm 0.113}$	0.763	-0.958	-0.881	0.91	0.435
7	$0.397_{\pm 0.213 \pm 0.0415}$	$-0.677_{\pm 0.626 \pm 0.171}$	$0.406_{\pm 1.58 \pm 0.189}$	0.800	-0.965	-0.898	2.19	0.087
8	$0.563_{\pm 0.372 \pm 0.0515}$	$0.179_{\pm 1.33 \pm 0.335}$	$-1.69_{\pm 6.07 \pm 0.648}$	0.826	-0.973	-0.908	0.827	0.479
9	$0.455_{\pm 0.908 \pm 0.103}$	$-1.39_{\pm 3.77 \pm 0.809}$	$6.76_{\pm 31.8 \pm 3.42}$	0.898	-0.986	-0.945	3.22	0.0217

Table B.6: Extracted Quark Polarisations for $SU(3)$-symmetric Sea.

	Polarisations		Correlations	Statistics	
Bin	$\Delta u_v/u_v$	$\Delta d_v/d_v$	$(\frac{\Delta u_v}{u_v}, \frac{\Delta d_v}{d_v})$	$\chi^2_{min}/4$	$CL(\chi^2_{min}, 4)$
1	$0.256_{\pm 0.0404 \pm 0.0222}$	$-0.533_{\pm 0.19 \pm 0.0918}$	-0.697	1.12	0.344
2	$0.193_{\pm 0.0382 \pm 0.019}$	$-0.0826_{\pm 0.182 \pm 0.0789}$	-0.669	0.109	0.98
3	$0.217_{\pm 0.0359 \pm 0.0187}$	$-0.259_{\pm 0.172 \pm 0.0758}$	-0.663	0.0722	0.991
4	$0.298_{\pm 0.0371 \pm 0.0242}$	$-0.299_{\pm 0.18 \pm 0.0797}$	-0.618	1.21	0.306
5	$0.322_{\pm 0.0352 \pm 0.0255}$	$-0.316_{\pm 0.177 \pm 0.0788}$	-0.593	1.53	0.189
6	$0.382_{\pm 0.0374 \pm 0.0287}$	$-0.627_{\pm 0.202 \pm 0.0963}$	-0.591	1.41	0.226
7	$0.45_{\pm 0.0443 \pm 0.0359}$	$-0.528_{\pm 0.261 \pm 0.117}$	-0.567	1.66	0.155
8	$0.462_{\pm 0.0757 \pm 0.0419}$	$-0.167_{\pm 0.528 \pm 0.23}$	-0.600	0.641	0.633
9	$0.645_{\pm 0.14 \pm 0.0611}$	$-0.62_{\pm 1.16 \pm 0.504}$	-0.613	2.44	0.045

Table B.7: Extracted Quark Polarisations for Unpolarised Sea.

Parameter	Δu_v	Δd_v	$\Delta\bar{q}$
N_q	$1.4_{\pm 0.6}$	$-0.9_{\pm 0.51}$	$5.8 \cdot 10^{3}{}_{\pm 1.4 \cdot 10^4}$
α_q	$1_{\pm 0.4}$	$0.11_{\pm 0.24}$	$3.6_{\pm 0.8}$
β_q	—	—	$12_{\pm 8.6}$
χ^2/NDF	0.18/9	0.7/9	0.071/7

Table B.8: Fit Results to the Polarised Parton Density Functions for the u_v and d_v Distributions. *Functions of the form (6.26) have been fitted to the quark polarisations assuming a polarisation-symmetric sea. See Section 6.5.2.*

Parameter	Δu	Δd	$\Delta\bar{q}$
N_q	$1.1_{\pm 0.33}$	$-1.3_{\pm 0.61}$	$1.9 \cdot 10^{4}{}_{\pm 3.5 \cdot 10^4}$
α_q	$0.86_{\pm 0.2}$	$0.57_{\pm 0.21}$	$3.8_{\pm 0.73}$
β_q	—	—	$16_{\pm 6.4}$
χ^2/NDF	0.21/9	0.71/9	0.11/7

Table B.9: Fit Results to the Polarised Parton Density Functions for the total u and d Distributions. *Functions of the form (6.26) have been fitted to the quark polarisations assuming $SU(3)$-symmetric polarised sea PDFs. See Section 6.5.2.*

First Moments ($Q^2 = 2.3$ (GeV/c)^2)			
x-Range	Δu	Δd	$\Delta\bar{q}$
$[0.023, 0.6]_{Sum}$	$0.49_{\pm 0.062 \pm 0.047}$	$-0.41_{\pm 0.1 \pm 0.11}$	$0.31_{\pm 0.15 \pm 0.056}$
$[0.023, 0.6]_{Fit}$	$0.45_{\pm 0.059 \pm 0.043}$	$-0.39_{\pm 0.09 \pm 0.097}$	$0.3_{\pm 0.15 \pm 0.055}$
$[0, 0.023]$	0.022	-0.09	0.0015
$[0.6, 1]$	0.026	-0.0052	$1.4 \cdot 10^{-7}$
$[0, 1]$	$0.5_{\pm 0.059 \pm 0.058}$	$-0.48_{\pm 0.09 \pm 0.14}$	$0.3_{\pm 0.15 \pm 0.056}$

Correlations of First Moments			
	Δu	Δd	$\Delta\bar{q}$
Δu	1	0.184	-0.812
Δd	0.184	1	-0.588
$\Delta\bar{q}$	-0.812	-0.588	1

Second Moments ($Q^2 = 2.3$ (GeV/c)^2)			
x-Range	Δu	Δd	$\Delta\bar{q}$
$[0.023, 0.6]_{Sum}$	$0.13_{\pm 0.016 \pm 0.012}$	$-0.067_{\pm 0.032 \pm 0.025}$	$0.039_{\pm 0.025 \pm 0.0067}$
$[0.023, 0.6]_{Fit}$	$0.12_{\pm 0.014 \pm 0.011}$	$-0.062_{\pm 0.026 \pm 0.021}$	$0.038_{\pm 0.024 \pm 0.0066}$
$[0, 0.023]$	0.00025	-0.0008	$2.7 \cdot 10^{-5}$
$[0.6, 1]$	0.018	-0.0035	$8.7 \cdot 10^{-8}$
$[0, 1]$	$0.13_{\pm 0.014 \pm 0.021}$	$-0.066_{\pm 0.026 \pm 0.025}$	$0.038_{\pm 0.024 \pm 0.0067}$

Correlations of Second Moments			
	Δu	Δd	$\Delta\bar{q}$
Δu	1	-0.342	-0.513
Δd	-0.342	1	-0.315
$\Delta\bar{q}$	-0.513	-0.315	1

Table B.10: Moments of Polarised Parton Density Functions for the total u and d Distributions. *The same parametrisations (6.26) as for the valence distributions were used. See Section 6.5.2.*

Appendix C

Description of Software Modules

A complex high energy experiment as HERMES involves a huge amount of software to operate the apparatus and perform various kinds of analyses. Most of this software has to be developed for the special needs of the experiment. The HERMES software packages are used for data production, Monte Carlo and analysis. They consist of roughly 200k lines of source code (not counting lines from external libraries as CERNLIB, GEANT, etc.). In the course of this work a variety of software packages (≈70k source lines) were designed, implemented and maintained. This appendix introduces the more important of these packages in more detail.

C.1 PINK

As mentioned in Chapter 4.4 the HERMES software makes use of the entity-relationship based database ADAMO [Che76, FP93] with the extension DAD [Wan95], which allows the implementation of a client-server based software layout. This concept has turned out to be very powerful for developing and maintaining the separate software modules. Apart from DAD the PINK application is one of the most important underlying packages that helped to achieve this goal. PINK combines the APIs (Application Program(ming) Interfaces) of ADAMO and DAD with the easy to use shell language TCL [Ous94]. Although TCL does not use a strict object-oriented (OO) language model, the PINK interface was designed in an OO inspired fashion that implements the ADAMO and DAD entities as objects. The TCL extension TK adds a X11 window interface to PINK which allows the development of Graphical User Interfaces (GUIs) to literally all data that is accessible at HERMES. A library of TCL/TK procedures provides ready-to-use elements for the implementation

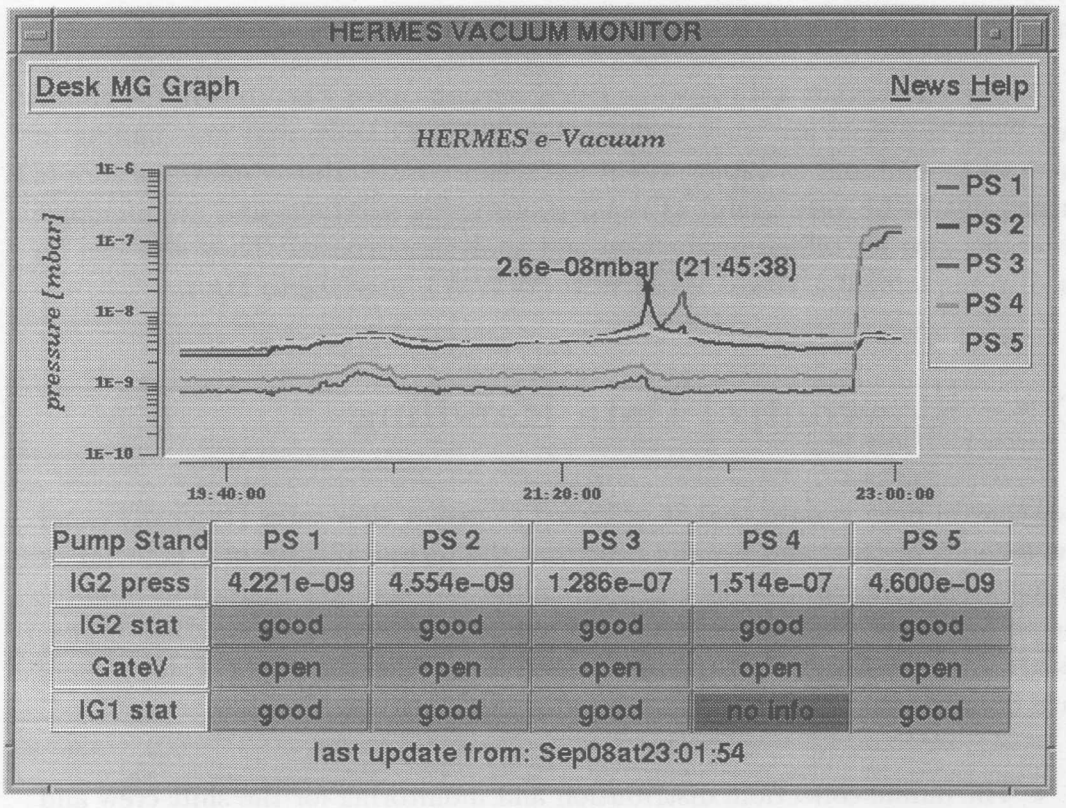

Figure C.1: Screen Dump of a PINK Monitor Client. *This example shows all main features of a monitoring client used online to display and control the status of the experimental hardware. The time graph visualises the history of important values (in this case the pressures at various pump stands). A cursor can be used to display the coordinates of each point on the curves. The coloured buttons at the bottom show the status of a variety of hardware components; the application can also be used to control the state of valves. The menu bar at the top part of the window hides additional features that are not frequently used.*

of PINK scripts.

Figure C.1 shows the screen dump of the PINK client that is used in the HERMES control room to monitor the vacuum status of the experimental region. More than 30 of such applications are used to run the various hardware components (see Appendix C.2).

Despite of the online application, the PINK browser `pb` plays an important role for the maintenance and debugging of software from the production chain (Figure 4.8) as well as for the data analysis. `pb` itself is a complex PINK script that allows the interactive view and inspection of all data tables (entities) and their relationships in an intuitive GUI. The browser is able to process all DAD

and ADAMO file formats and can also connect to DAD data servers.

Finally there exists a windowless PINK version called FLOYD. On the online side FLOYD scripts are used as watchdogs or check tasks that are running in the background and as taping client (see Figure C.2). But windowless scripts turned out to be very useful as rapid prototyping solutions and maintenance programs also for offline production and analysis purposes. They also can be used to implement a World Wide Web (WWW) interface to DAD.

C.2 Slowcontrol Data Handling

Slowcontrol data is data that is collected at rather slow rates (typically every few seconds or less) and usually describes the technical state of a detector or help system. Slowcontrol data is used online (during data taking) to monitor the performance of the experiment and offline (during data production or analysis) for calibration or data quality checks. Hence the processing of slowcontrol data divides into two parts:

- The online collection, distribution and monitoring for the shift crew and
- the offline preprocessing to allow easy access for detector experts and analysing physicists.

The layout of the online slowcontrol part is shown in Figure C.2. At HERMES the heart of the online monitoring software is a collection of DAD servers that are connected at one end to a couple of low-level clients (usually controlling some hardware component) and at the other end to high-level clients which are evaluating the data. As shown in the diagram, there are three kinds of connections between low-level clients and the hardware: In the simplest case the low-level client talks directly (via functions of the online library) to a piece of hardware. However for historical reasons, two other connection schemes are used at HERMES, where the controlling programs are not directly connected to the servers, but are talking indirectly to the low-level clients via shared memory or the online decoder. In both cases the low-level programs might have their own (usually command line driven) user interfaces. The high-level clients are used to process the data that is available at the servers. The taping client collects at this level all data from the servers and writes it to slowcontrol files, which are later the main input for the slowcontrol production. Other processes continuously display status information on graphical PINK displays in the HERMES main control room and others run in the background to check the hardware status and give alarms in case of malfunctions. All important

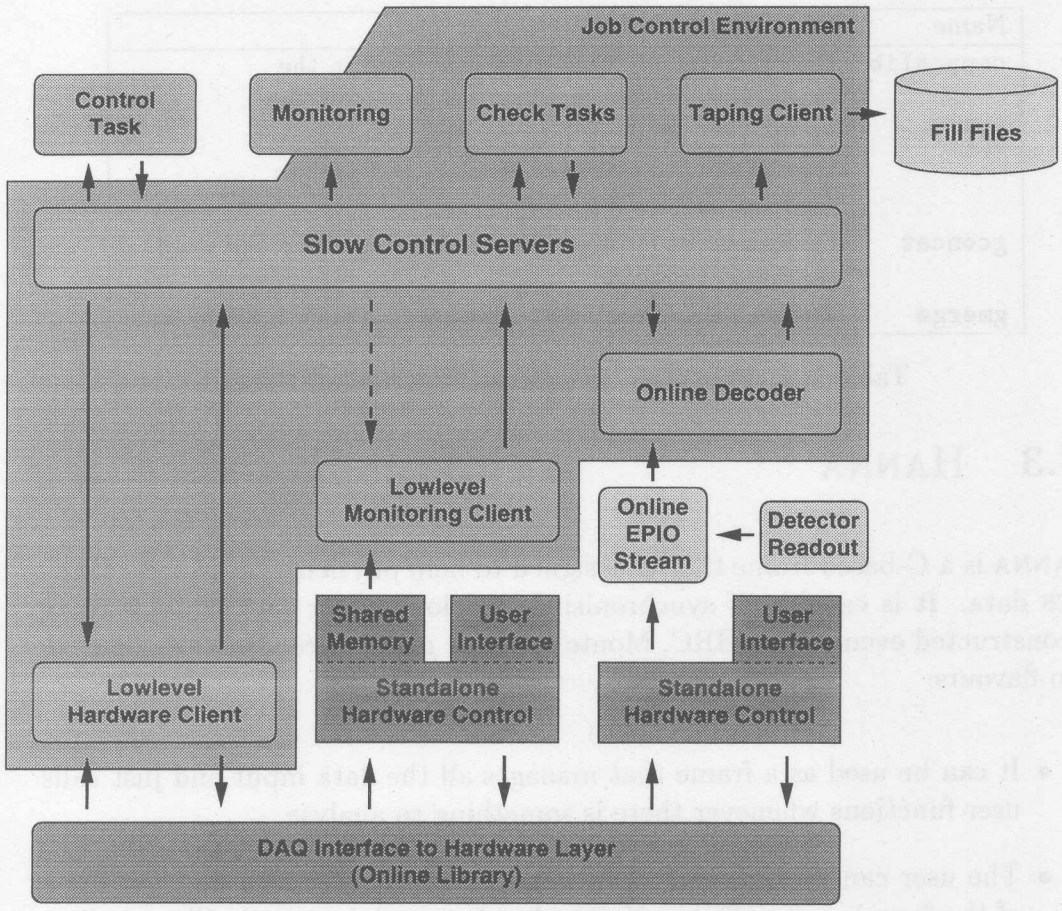

Figure C.2: Online Collection of Slowcontrol Data. *Boxes represent isolated programs, the arrows indicate the direction of data exchange. The job control environment monitors the availability of all online components that are essential to collect online slowcontrol data in* DAD *format and store it via the taping client to fill files.*

processes run under a special shell (jobcontrol) which takes care that processes are restarted on (abnormal) termination and automatically informs software responsible people on certain conditions.

Once the data is taken, the offline processing of the slowcontrol data as shown in Figure 4.8 can take place. A couple of help programs (see Table C.1) collects slowcontrol and other relevant data from various sources, filters the data stream, scales the update rates according to certain rules, and writes one time-ordered output file per HERA machine fill and one ore more for the time in between fills.

Name	Description
`copycalib`	Builds an image of all data contained in the production servers (calibration, mapping, etc.)
`gsplitt`	Splits a dataflow up into subfiles (one for each type of slowcontrol data (table)) and applies selection and modification rules.
`gconcat`	Concatenates multiple files into a single one and does consistency checks.
`gmerge`	Merges many input files together in a time ordered way.

Table C.1: Programs to process Slowcontrol Data.

C.3 HANNA

HANNA is a C-based frame that is designed to help physicists to analyse HERMES data. It is capable of synchronising the slowcontrol data while reading reconstructed events from HRC, Monte Carlo or μDST files. HANNA comes in two flavours:

- It can be used as a frame that manages all the data input and just calls user functions whenever there is something to analyse.
- The user can do the event data handling on his/her own and use some of the functions bundled in HANNALIB for special purposes like synchronising the slowcontrol data.

HANNA is not as voluminous as HEP, e.g. it does not contain any HBOOK functionality by default. Hence very small and resource saving analysis programs can be written by using HANNA as it is. As well, much more complex applications can be developed by linking the user code with HBOOK and other CERN libraries.

The HANNA frame

In its simplest form HANNA can be used as a frame. The user does not have to deal with any data input or book keeping, since HANNA interprets certain command line flags to detect what data has to be read and will feed this data to user functions. A user function is a short pice of code the user has to supply whenever he wants to take care of a certain event (e.g. a new run will be started, a new event has to be analysed, etc.). A list of all user callback functions is given in Table C.2. If the user does not want to deal with a certain

Name	Description
`int ha_main( );`	Has to be called from `main()` function to start up the HANNA frame.
`int user_init( );`	Called after the slowcontrol module is initialised.
`int user_end( );`	Called at the very end.
`int user_runinit( );`	Called whenever a new run is processed.
`int user_runend( );`	Called whenever a run was processed.
`int user_event( );`	Called whenever an event has to be processed.
`int user_slow( );`	Called whenever a new slow table is read.
`int user_burstinit( );`	Called only in μDST mode, whenever a new burst was read.
`int user_burstend( );`	Called only in μDST mode, whenever a new burst was processed.

Table C.2: List of HANNA's User Functions.

Name	Description
`int ha_debuginit( );`	Initialise HANNA debuging module and look up debugging levels from environment.
`int *ha_debugptr( );`	Get pointer to debugging level for a module.
`int ha_debugset( );`	Set the debugging value for a module.
`void ha_debuglist( );`	Print a list of module names and debug levels.
`int ha_addarg( );`	Add one entry to the list of command line switches (including default value and help line).
`void ha_usage( );`	Print a summary of all defined command line switches.
`int ha_slowinit( );`	Use slowcontrol syncing library.
`int ha_slowsync( );`	Synchronise the slowcontrol data for a given time.
`int ha_slowmodflag( );`	Modify a flag that controls a slowcontrol table.

Table C.3: Selected HANNALIB Functions.

condition, no function needs to be supplied and some HANNA dummy code will be executed.

The HANNA library

The HANNA library contains a collection of useful functions to be used in the user code. Parts of this library can also be used by more advanced users who want to take care of the event-handling themselves but need for example the synchronisation functionality to deal with slowcontrol data. Some example functions from the HANNA library are listed in Table C.3.

List of Figures

I'm grateful to the following persons and institutes for allowing me to use their figures or figure templates: Klaus Ackerstaff (Figure 5.3 and C.1), Bernd Braun (Figure 4.4), Antje Brüll (Figure 2.4), Philipp Geiger (Figure 3.3 and 4.6), Wolfgang Wander (Figure 4.5 and 4.9), Ralf Kaiser (Figure 4.7) and MPI-K Heidelberg (Figure 4.3).

List of Tables

Bibliography

[ABS86] A.A. Akhundov, D.Yu. Bardin and N.M. Shumeiko: *Electromagnetic corrections to elastic radiative tail in deep inelastic lepton-nucleon scattering*, Sov. J. Nucl. Phys. 44 (1986) 988.

[Ack95] K. Ackerstaff, M. Düren, M. Ferstl, M.-A. Funk, P. Green, Ph. Oelwein, P. Welch and W. Wander: *A Tcl/Tk based Database Interface to* Adamo *and* Dad, Proceedings of CHEP '95, Rio de Janeiro, 18.-22. 9. 1995.

[Ack96] K. Ackerstaff: *First Results from the* Hermes *Experiment Using Unpolarized Targets*, PHD Thesis, University of Hamburg (1996).

[AG83] B. Andersson, G. Gustafson et al.: *Parton Fragmentation and String Dynamics*, Phys. Rep. 97 (1983) 31.

[Ago95] G. D'Agostini: *Probability and Measurement Uncertainty in Physics – a Bayesian Primer –*, DESY Report 95-242 (1995).

[AP77] G. Altarelli and G. Parisi: *Asymptotic Freedom in Parton Language*, Nucl. Phys. B126 (1977) 298.

[AS94] I.V. Akushevich and N.M. Shumeiko: *Radiative effects in deep inelastic scattering of polarized leptons by polarized light nuclei*, J. Phys. G20 (1994) 513.

[Bar95] HermesPolarimeter Group (S. Barrow et al.): *Interim Report on the Measurement of the Positron Beam Polarization*, Hermes Internal Note 96-002 (1996).

[BCDMS90] BCDMS Collaboration (A.C. Benvenuti et al.): *A High Statistics Measurement of the Deuteron Structure Functions F2(x,Q^2) and R from Deep Inelastic Muon Scattering at High Q^2*, Phys. Lett. B237 (1990) 592.

[BCS94] F. Butler, H. Chen, J. Sexton, A. Vaccarino and D. Weingarten: *Hadron Masses from the Valence Approximation to Lattice QCD*, Nucl. Phys. B430 (1994) 179.

[Ben98] T. Benisch: *Polarisierte Bhabha-Streuung und Luminositätsmessung im* Hermes*-Experiment.*, PHD Thesis, University Erlangen-Nürnberg (1998).

[BGH97] C. Best, M. Göckeler, R. Horsley, L. Mankiewicz, H. Perlt, P. Rakow, A. Schafer, G. Schierholz, A. Schiller, S. Schramm and P. Stephenson: *Hadron Structure Functions from Lattice QCD – 1997*, Talk given at 5^{th} International Workshop on Deep Inelastic Scattering and QCD (DIS 97), Chicago, IL, 14-18 Apr 1997, e-print: hep-ph/9706502 .

[Bjo66] J.D. Bjorken: *Application of the Chiral $U(6) \times U(6)$ Algebra of Current Densities*, Phys. Rev. 148 (1966) 1467.

[BMT59] V. Bargman, L. Michel and V. Telegdi: *Precession of the Polarization of Particles Moving in an Homogenious Magnetic Field*, Phys. Rev. Lett. 2 (1959) 435.

[Bra97] B. Braun (for the Hermes collaboration): *The* Hermes *Polarimeter*, Proceedings of the 7^{th} Internationl Workshop on Polarized Gas Targets and Polarized Beams, 18.-22.8.1997 at the University of Illinois at Urbana-Champaign, to be published.

[Bru93] R. Brun et al.: Geant *Detector Description and Simulation Tool (Long Writeup W5013)*, CERN-CN Application Software Group, 1993.

[Brü93] A. Brüll: *Die Strukturfunktion des Nukleons bei kleinen Werten von x*, PHD Thesis, University Freiburg (1993).

[BS86] J. Buon and K. Steffen: HERA *Variable-energy "Mini" Spin Rotator and Head-on ep Collision Scheme with Choice of Electron Helicity*, Nucl. Instr. & Meth. A245 (1986) 248.

[CG69] C.G. Callan Jr. and D.J. Gross: *High-Energy Electroproduction and the Constitution of the Electric Current*, Phys. Rev. Lett. 22 (1969) 156.

[Che76] P. Chen: *The Entity-Relationship Model – Toward a Unified View of Data*, ACM Transactions on Database Systems 1 (1976) 9.

[CN93] CERN-CN devision: EPIO- *Experimental Physics Input Output Package*, CERN Program Library Long Writeup I101, CERN (1993).

[CR93] F.E. Close and R.G. Roberts: *Consistent Analysis of the Spin Content of the Nucleon*, Phys. Lett. B316 (1993) 165.

[CS77] F.E. Close and D. Sivers: *Whirlpools in the Sea: Polarization of Antiquarks in a Spinning Proton*, Phys. Rev. Lett. 39 (1997) 1116.

[DF97] M. Düren and M.-A. Funk: *Quark Spin Decomposition from Inclusive and Semi-Inclusive Polarised Data*, Hermes Internal Note 97-029 (1997).

[Dür95] M. Düren: *The* Hermes *Experiment: From the Design to the First Results*, Habilitation, University Erlangen-Nürnberg (1995).

[Dür97] M. Düren: *A Method to Extract Quark Spin Distributions*, Hermes Internal Note 97-067 (1997).

[E143:95] E143 Collaboration (K. Abe et al.): *Precision Measurement of the Proton Spin Structure Function g_1^p*, Phys. Rev. Lett. 74 (1995) 346.

[E143:96] E143 Collaboration (K. Abe et al.): *Measurements of the Proton and Deuteron Spin Structure Function g_2 and Asymmetry A_2*, Phys. Rev. Lett. 76 (1996) 587.

[E154:97] E154 Collaboration (K. Abe et al.): *Precision Determination of the Neutron Spin Structure Function g_1^n*, Phys. Rev. Lett. 79 (1997) 26.

[EDJ77] W.T. Eadie, D. Dijard, F.E. James, M. Roos and B. Sadoulet: *Statistical Methods in Experimental Physics*, North-Holland Publishing Company, Second Printing 1977, ISBN 0-7204-0239-5.

[EJ74] J. Ellis and R.L. Jaffe: *Sum Rule for Deep-Inelastic Electroproduction from Polarized Protons*, Phys. Rev. D45 (1992) 2269.

[EK95] J. Ellis and M. Karliner: *Determination of α_s and the Nucleon Spin Decomposition using recent Polarized Structure Function Data*, Phys. Lett. B341 (1995) 397.

[EMC84] European Muon Collaboration (M. Arneodo et al.): *Quark and Diquark Fragmentation into Neutral Strange Particles as Observed in Muon-Proton Interactions at 280 GeV*, Phys. Lett. B145 (1984) 458.

[EMC89a] European Muon Collaboration (M. Arneodo et al.): *Measurements of the u-Valence-Quark Distribution Functions in the Proton and u-Quark Fragmentation Functions*, Nucl. Phys. B321 (1989) 541.

[EMC89b] European Muon Collaboration (J. Ashman et al.): *An Investigation of the Spin Structure of the Proton in Deep Inelastic Scattaring of Polarized Muons on Polarized Protons*, Nucl. Phys. B328 (1989) 73.

[ESW96] R.K. Ellis, W.J. Stirling and B.R. Webber: *QCD and Collider Physics*, Cambridge University Press 1996, ISBN 0-521-58189-3.

[Fer97] M. Ferstl: *Polarisierte tiefinelastische Streuung an einem ^{3}He-Target im* Hermes*-Experiment*, PHD Thesis, University Erlangen-Nürnberg (1997).

[FF78] R.D. Field and R.P. Feynmann: *A Parametrization of the Properties of Quark Jets*, Nucl. Phys. B136 (1978) 1.

[FGP90] J.L. Friar, B.F. Gibson, G.L. Payne, A.M. Bernstein, T.E. Chupp: *Neutron Polarization in Polarized ^{3}He*, Phys. Rev. C42 (1990) 2310.

[FP93] S.M. Fisher and P. Palazzi: *The* Adamo *Data System. Programmers Manual – Version 3.2*, CERN-ECP and Rutherford Appleton Laboratory (UK) (1993).

[Fun95] M.-A. Funk: *The* PinK *Documentation Page*, `http://www-hermes/pink/` (1995).

[Fun96] M.-A. Funk: *Hanna: A C-based* Hermes *Analysis Tool.*, `http://www-hermes.desy.de/hanna/`

[Gei97] Ph. Geiger: *Private communication* (1997).

[Gei98] PH. GEIGER: *Measurement of Fragmentation Fuctions at* HERMES, PHD Thesis, Ruprecht-Karls-University Heidelberg, Germany (1998).

[Gel64] M. GELL-MANN: *A Schematic Model of Baryons and Mesons*, Phys. Lett. 8 (1964) 214.

[GHM97] M. GÖCKELER, R. HORSLEY, L. MANKIEWICZ, H. PERLT, P. RAKOW, G. SCHIERHOLZ and A. SCHILLER: *A lattice determination of the second moment of the polarised valence quark distribution*, Phys. Lett. B414 (1997) 340.

[GL72] V.N. GRIBOV and L.N. LIPATOV: *Deep Inelastic ep-Scattering in Pertubation Theory*, Sov. J. Nucl. Phys. 15 (1972) 438.

[GMV97] PH. GEIGER, N. MAKINS, E. VOLK et al.: *The* HERMES *Monte Carlo*, `http://www-hermes.desy.de/hmc/`.

[Got67] K. GOTTFRIED: *Sum rule for high-energy electron-proton scattering*, Phys. Rev. Lett. 18 (1967) 1174.

[GRSV95] M. GLÜCK, E. REYA, M. STRATMANN, W. VOGELSANG: *Next-to-Leading Order Radiative Parton Model Analysis of Polarized Deep Inelastic Scattering*, Phys. Rev. D53 (1996) 4775.

[GRV95] M. GLÜCK, E. REYA, W. VOGT: *Dynamical Parton Distribution of the Proton and small x Physics*, Z. Phys. C67 (1995) 433,

[GS96a] T. GEHRMANN and W.J. STIRLING: *Polarized Parton Distributions in the Nucleon.*, Phys. Rev. D53 (1996) 6100.

[GS96b] T. GEHRMANN and W.J. STIRLING: *Analytic Approaches to the Evolution of Polarised Parton Distributions at Small x.*, Phys. Lett. B365 (1996) 347.

[Gut98] A. GUTE: *Private Communication*, To be published in his PHD Thesis, University Erlangen-Nürnberg.

[Has97] D. HASH: *Private Communication*, To be published in her PHD Thesis, Humboldt University Berlin.

[HER97a] THE HERMES g_1^n GROUP: *Determination of the 1995 Data Quality and the Extraction of the Spin Structure Function of the Neutron*, HERMES Internal Note 97-007 (1997).

[HER97b] HERMES COLLABORATION (K. ACKERSTAFF et al.): *Measurement of the Neutron Spin Structure Function g_1^n with a Polarized ^{3}He-3 Internal Target*, Phys. Lett. B404 (1997) 383.

[IER96] G. INGELMAN, A. EDIN, J. RATHSMAN: *LEPTO 6.5 - A Monte Carlo Generator for Deep Inelastic Lepton-Nucleon Scattering*, DESY Report 96-057, `http://www3.tsl.uu.se/thep/lepto/`.

[Ihs98] H. IHSSEN: *Private communication*, (1998).

[Jac97] H.E. JACKSON (for the HERMES COLLABORATION): *Proposal for a Dual Radiator RICH for* HERMES, HERMES Internal Note 97-003 (1997).

[Kai97] R.B. KAISER: *Measurement of the Spin Structure of the Neutron using Polarised Deep Inelastic Scattering*, PHD Thesis, Simon Fraser University, Canada (1997).

[Kol98] M. KOLSTEIN: *Exclusive ρ_0 Electroproduction at* HERMES, PHD Thesis, Free University, Amsterdam, to be published.

[Lee93] K. LEE et al.: *A laser optical pumped polarized ^{3}He target for storage rings*, Nucl. Instr. & Meth. A333 (1993) 294.

[Lip75] L.N. LIPATOV: *The Parton Model and Pertubation Theory*, Sov. J. Nucl. Phys. 20 (1975) 94.

[Lor95] W. LORENZON (for the HERMES COLLABORATION): *Proposal to* DESY *for a Longitudinal Electron Polarimeter at* HERA-*East Section*, May 1995.

[Men97] F.M. MENDEN: *Measurement of the Valence Quark Spin Distributions of the Nucleon Using Deep Inelastic Scattering at* HERMES, Diploma Thesis, University Hamburg (1997).

[MKP96] F. MEISSNER, G. KYLE, S. PATE, A. SCHWIND, A. BRUELL: *Photoproduction Trigger for HERMES*, HERMES Internal Note 96-026 (1996).

[MRS94a] A.D. MARTIN, R.G. ROBERTS, W.J. STIRLING: *Parton Distributions of the Proton*, Phys. Rev. D50 (1994) 6734.

[MRS94b] A.D. MARTIN, R.G. ROBERTS, W.J. STIRLING: *Parton Distributions for low Q^2*, Phys. Rev. D51 (1994) 4756.

[MW92] G. MARCHESI, B.R. WEBBER et al.: HERWIG *5.1 - A Monte carlo Event Generator for Simulating Hadron Emission Reactions with Interfering Gluons*, Comp. Phys. Comm. 67 (1992) 465.

[Nac86] O. NACHTMANN: *Elementarteilchenphysik, Phänomene und Konzepte*, Vieweg Verlagsgesellschaft Braunschweig, Esrte Auflage 1986, ISBN 3-528-08926-1.

[Neu97] F. NEUENREITHER: *Beiträge zur Messung der Spinstrukturfunktion g_1^n des Neutrons im* HERMES *Experiment*, PHD Thesis, University Erlangen-Nürnberg (1997).

[NMC92] NEW MUON COLLABORATION (P. AMAUDRUZ et al.): *Proton and Deuteron F_2 Structure Functions in Deep Inelastic Muon Scattering*, Phys. Lett. B295 (1992) 159.

[NMC94] NEW MUON COLLABORATION (M. ARNEODO et al.): *Reevaluation of the Gottfried sum*, Phys. Rev. D50 (1994) 1.

[NMC95] NEW MUON COLLABORATION (M. ARNEODO et al.): *Measurement of the Proton and the Deuteron Structure Functions, F2(p) and f2(n)*, Phys. Lett. B364 (1995) 107.

[Oel95] PH. OELWEIN: *Messung der longitudinalen Elektronenpolarisation beim Speicherring* HERA *und Monte-Carlo-Studien zur Kalibration des* HERA-*Elektronen-Polarimeters*, Diploma Thesis, MPI-K Heidelberg (1995).

[Ous94] J.K. OUSTERHOUT: *Tcl and Tk Toolkit*, Addison-Wesley Massachusetts (1994).

[PDG94] PARTICLE DATA GROUP (M. AGUILAR-BENITEZ et al.): *Review of Particle Properties*, Phys. Rev. D, Vol. 50 No. 3, 1.6.1994.

[PEPSI] M. VELTRI: *Polarized Quark Distributions from Semi-inclusive Leptoproduction: Studies for the* HERMES *Experiment*, MPIH-V18-1992;
M. MAUL: *The PEPSI Page – Polarized Electron-Proton Scattering Interactions*, `http://www.th.physik.uni-frankfurt.de/~maul/pepsi.html`

[Pre97] J. PRETZ: *Messung der polarisierten Quarkverteilungen in semi-inklusiver Myon-Nukleon-Streuung* , PHD Thesis, Johannes-Gutenberg University Mainz (1997).

[PRS94] B. POVH, K. RITH, CH. SCHOLZ, F. ZETSCHE: *Teilchen und Kerne: Eine Einführung in die physikalischen Konzepte*, Springer Verlag Berlin, Zweite Auflage 1994, ISBN 3-540-58172-3.

[PTV95] W.H. PRESS, S.A. TEUKOLSKY, W.T. VETTERLING, B.P. FLANNERY: *Numerical Recipes in C: The Art of Scientific Computing*, Cambridge University Press, Second Edition 1995, ISBN 0-521-43108-5, `http://nr.harvard.edu/nr/bookc.html`.

[Sch97] D. DE SCHEPER et al.: *The* HERMES *Polarized* ^{3}*He Internal Gas Target*, Submitted to Nuclear Instruments and Methods in Physics Research (1997).

[Sjö94] T. SJÖSTRAND: *High Energy Physics Event Generation with* PYTHIA *5.7 and* JETSET *7.4*, Comp. Phys. Comm. 82 (1994) 74, `http://www.thep.lu.se/tf2/staff/torbjorn/Pythia.html`.

[SLAC92] L.W. WHITLOW, E.M. RIORDAN, S. DASU, S. ROCK, A. BODEK: *Precise Measurement of the Proton and Deuteron Structure Functions from a Global Analysis of the SLAC Deeo Inelastic Electron Scattering Cross-Sections*, Phys. Lett. B282 (1992) 475.

[SMC94a] SPIN MUON COLLABORATION (D. ADAMS et al.): *Measurement of the Spin Dependent Structure Function* $g_1(x)$ *of the Proton*, Phys. Lett. B329 (1994) 399.

[SMC94b] SPIN MUON COLLABORATION (D. ADAMS et al.): *Spin Asymmetry in Muon-Proton Deep Inelastic Scattering on a Transversely Polarized Target*, Phys. Lett. B336 (1994) 125.

[SMC95] SPIN MUON COLLABORATION (D. ADAMS et al.): *A New Measurement of the Spin Dependent Structure Function* $g_1(x)$ *of the Deuteron*, Phys. Lett B357 (1995) 248.

[SMC97a] SPIN MUON COLLABORATION (D. ADAMS et al.): *Spin Structure of the Proton from Polarized Inclusive Deep-Inelastic Muon-Proton Scattering*, Phys. Rev. D56 (1997) 5330.

[SMC97b] SPIN MUON COLLABORATION (D. ADAMS et al.): *The Spin-Dependent Structure Function* $g_1(x)$ *of the Deuteron from Polarized Deep-Inelastic Muon Scattering*, Phys. Lett. B396 (1997) 338.

[SMC97c] SPIN MUON COLLABORATION (D. ADEVA et al.): *The Spin-Dependent Structure Function $g_1(x)$ of the Proton from Polarized Deep-Inelastic Muon Scattering*, Phys. Lett. B412 (1997) 414.

[SMC98] SPIN MUON COLLABORATION (D. ADEVA et al.): *Polarized Quark Distributions in the Nucleon from Semi-Inclusive Spin Asymmetries*, Phys. Lett. B420 (1998) 180.

[ST64] A.A. SOKOLOV and I.M. TERNOV: *On Polarization and Spin Effects in the Theory of Synchrotron Radiation*, Sov. Phys. Dokladi 8 (1964) 1203.

[Ste97] J. STEWART (for the HERMES COLLABORATION): *The* HERMES *Polarized Hydrogen Internal Gas Target*, Proceedings of the 7^{th} Internationl Workshop on Polarized Gas Targets and Polarized Beams, 18.-22.8.1997 at the University of Illinois at Urbana-Champaign, to be published.

[Stö97] U. STÖSSLEIN: *Private communication* (1997); the fit includes data from: [E143:95], [SMC97a] and [SMC97c].

[Stö98] U. STÖSSLEIN: *Private Communication* (1998).

[Tal98] H.A. TALLINI: *A measurement of the quark spin distributions of the nucleon at* HERMES, PHD Thesis, University of Liverpool (1998).

[Tho27] L.H. THOMAS: *The Kinematics of an Electron with an Axis*, Philos. Mag. 3 (1927) 1.

[Tip97] B. TIPTON for the HERMES POLARIMETER GROUP: *Analysis of Positron Beam Polarization Measurements in 1996*, HERMES Internal Note 97-019 (1997).

[Wan95] W. WANDER, K. ACKERSTAFF, M. DÜREN, M. FERSTL, M.-A. FUNK, P. GREEN, PH. OELWEIN, D. POTTERVELD and P. WELCH: DAD – *Distributed* ADAMO *Database system at* HERMES, Proceedings of CHEP '95, Rio de Janeiro, 18.-22. 9. 1995.

[Wan96] W. WANDER: *Rekonstruktion hochenergetischer Streuereignisse im* HERMES *Experiment*, PHD Thesis, University Erlangen-Nürnberg (1996).

[WF97] W. WANDER and M.-A. FUNK for the HERMES Software Group: *The* HERMES *Data Production PC Farm*, Proceedings of CHEP '97, Berlin, 7.-11. 4. 1997.

[Wil74] K.G. WILSON: *Confinements of Quarks*, Phys. Rev. D10 (1974) 2445.

[Zw64] G. ZWEIG: *A SU_3 Model for Strong Interaction Symmetry and its Breaking*, CERN Preprint TH-401 adn 412 (1964).

Acknowledgements

Finally I want to take this opportunity to express my thanks to all those people without whom a successful completion of this thesis would not have been possible. Since this list is necessarily incomplete, I apologise to all those HERMES members (probably mostly hardware-related) who don't find their name in one of the following paragraphs.

First of all, I would like to thank my advisor Albrecht Wagner who encouraged me to begin this work at HERMES and gave me much freedom to define my position in the collaboration and the analysis issues myself. Beside his administrative duties at DESY he always found the time and patience to listen to my (most of the time much too technical) presentations and often pointed out solutions that I did not see. From DESY I also want to thank Yorck Holler and Peter Schüler who have been always helpful to make computer hardware investments and journeys to conferences possible.

It was a pleasure to join HERMES at a very early state, where the software development for slowcontrol and analysis was still a real challenge. I thank Michael Düren as the software coordinator for leaving all the software crew enough room for designing and implementing their own concepts. I want to thank Wolfgang Wander for constantly convincing people about the innovative HERMES software concept and for his help and discussion in any critical situation. But also the other members of the former HERMES software office, Klaus Ackerstaff, Holger Ihssen and Philipp Oelwein, have been very helpful in managing the technical tasks not only by constantly offering a friendly and humorous office environment. I want to thank Manfred Ferstl, Philipp Geiger, Alexander Kisselev, Machiel Kolstein, Naomi Makins, Falk Meißner and Erik Volk, who always helped in word and deed. I would not have found the time to focus on the physical part of this thesis without Knut Woller, who took over most of my software duties and source responsibilities at that time. I thank Walter Brückner for his help with the HERMES DAQ and online system and his flexibility to accept at least parts of all the new technologies. As representatives for the DESY computer centre I want to thank Susanne Brand, Michael

Ernst, Patrick Fuhrmann, Karsten Künne and Dirk Wetter, who always have been helpful in questions concerning the SGI cluster, networking and taping robots.

The physical analysis I have done at HERMES benefited a lot from the freedom that Antje Brüll as the analysis coordinator gave me in defining my own tasks and milestones. It would not have been possible without various ideas inspired by discussions with her, Holger Ihssen, Michael Düren, Klaus Rith, Hugh Tallini, Michael Ruh and many others. I am thankful for the detailed data quality information from the inclusive analysis group: Manfred Ferstl, Andreas Gute, Delia Hasch, Uta Stößlein and many others. I want to express my special thanks to Bryan Tipton who did the same kind of analysis independently at MIT. This work gained a lot from the various, very fruitful discussions and his endurance and patience in producing the first official results at DESY. I'm grateful to Ed Kinney, who spent the time to point out those text passages where I abused the English language too crudely and offered me a lot of style improvements. I'm also grateful to Pamela Chumney for proof-reading an early version of this document and to a huge number of collaboration members for still pointing out typos in the very latest version.

Working as a physicist is a very time consuming job. I thank Philipp Oelwein for maintaining the Offsite-Meeting not only as a reason not to spent the evening in front of the terminal at least once a week. He and Ann-Christine Mecke are the persons who are responsible for the fact that I did not miss all cultural events in Hamburg. Representative for the other offsiters I greet Andreas, Machiel, Greg, Brynnen, Jeff, Antje, Naomi, Manfred, Thomas and Wolfgang L.. I'm very grateful to Klaus, Wolfgang W. and Falk, who helped to relax from the sometimes strenuous workdays at DESY with personal (and much too often also physics-related) discussions in the various pubs of Ottensen. I want to thank also Ainhoa, Asta, Axel, Carola, Focky, Oliver, Rasmus, Susi, Sven, both Verenas and all the unnamed other bartenders of these locations for providing a leisurely atmosphere even in the very late hours of the night.

Schließlich danke ich meinen Eltern, meinen Brüdern und meinen Freunden aus Heidelberg für die schönen, wenn auch meist viel zu kurzen, Aufenthalte dort. Leider hat die Zeit nicht immer ausgereicht, mich genügend um all die zu kümmern, die ich viel zu selten sehe.